Optimization of flavin oxidase enzymes for human health monitoring

By
Dwight O'Dell Deay III

Submitted to the graduate degree program in Biochemistry and Biophysics and the Graduate Faculty of the University of Kansas in partial fulfillment of the requirements for the degree of Doctor of Philosophy.

_____

Chair: Joanna Slusky

_____

Peter A. Petillo

_____

Cindy Berrie

_____

Roberto De Guzman

_____

Erik Holmstrom

_____

Krzysztof Kuczera

Date Defended: 28 April 2021

The dissertation committee for Dwight O'Dell Deay III certifies that this is the approved version of the following dissertation:

Optimization of flavin oxidase enzymes for human health monitoring

_____

Chair: Joanna Slusky

Date Approved: _____

Abstract

Biosensors are an analytic modality able to quantify, in real time, the abundance of specific analytes in complex biological mixtures such as blood, the brain, and in a variety of organs. However, the use of biosensors has been limited to analytes for which suitable oxidase enzyme exists. Flavin dependent peroxide producing oxidase enzymes serve as the highly specific bio-recognition elements in the fabrication of amperometric biosensors. While many enzymes have been evaluated for the purposes of *in vivo* sensing, most of these studies have failed because these enzymes are inherently unsuitable for *in vivo* biosensing applications because of low stability, low substrate affinity, and/or slow rates of turnover. The common thread that ties together these diverse studies performed as part of my dissertation work is the focus on improving enzymes for *in vivo* biosensing and human health monitoring applications. My goal has been to improve the toolbox available to the electrochemists and developers of biosensors by engineering oxidase enzymes with improved performance *in vivo* and *in vitro* biosensing applications. Specifically, my dissertation work focuses primarily on two critical aspects of biosensor design: (1) the structure-informed rational improvement of three FDPGOs as potential nicotine oxidases and (2) the successful use of a gold binding peptide fusion sequence for the orientation-controlled immobilization of a putrescine oxidase on gold surfaces.

This dissertation is dedicated to my late graduate mentor, Dr. Mark L. Richter, who passed away from complications of COVID-19 at the end of my doctoral studies.

He will be dearly missed.

Acknowledgements

During my PhD work I have been fortunate to be supported by numerous individuals and organizations.

I would like to first thank my late graduate mentor, Dr. Mark Richter. My life changed forever the day I walked into Mark's office and asked him if I could volunteer in his lab. This opportunity was shortly followed by financial support as well as support for my application to the molecular biosciences graduate program, without which I would not have had the opportunity to grow into the scientist I am today. Beyond being a phenomenal mentor and PhD advisor, Mark was an incredible friend who supported me through good times and bad. I will never forget his humor, empathy, kindness, and wisdom. His passing from complications of COVID-19 is a true tragedy.

I would also like to thank our lab's long time collaborator, Dr. Peter Petillo, for his mentorship and support throughout my doctoral studies. Because of Pete I had the benefit of a second actively engaged mentor who along with Mark helped shape my development as a scientist. Pete also gave me the opportunity to participate in the establishment of his biotechnology company, Design-Zyme, as part of an industrial internship which was required by my training grant. This internship experience which was one of the most professionally enriching experiences I have had. When Mark passed away from COVID, Pete stepped up to help myself and Mark's other graduate students complete and publish our doctoral work. His friendship and generous assistance in the last months of my doctoral studies was invaluable and a kindness I will always be grateful to him for.

I would also like to thank Dr. Johanna Slusky for serving as my faculty mentor after Mark's passing and giving me excellent advice and guidance while I navigated the final months of my studies.

I would also like to thank all my current and former lab members in both the Richter lab and at Design-zyme who provided advice and fellowship throughout my doctoral work. In particular, I would like to Dr. Kim Colvert for her invaluable tutelage at the bench and for the lively scientific and political discussions that made coming into Mark's lab every day even more enjoyable.

I would like to acknowledge the support I received from the NGIS Biotechnology training grant program which supported me and my research for two years. In addition to funding, the courseware and opportunity to be exposed to the commercial biotechnology field was an enriching and valuable experience.

I would also like to acknowledge the support I received from the molecular biosciences department which provided me with GTA appointments when external funding was unavailable and for their invaluable help navigating the loss of my mentor. The department also provided financial support for my travel to present my work and provided me the opportunity to participate in departmental seminars and award presentations that furthered my development as a scientist.

I would also like to thank my late grandfather, Ronald Barnes, who kindled my interest in science from a young age and sparked my curiosity for the natural world.

Finally, I would like to thank my parents, Charles and Kimberly Deay, who encouraged my interest in science growing up and who supported me during my baccalaureate and doctoral studies. They never gave up on my dream of one day becoming a scientist, even when the path forward seemed insurmountable.

Table of Contents

Table of Figures

List of Tables

1 Introduction

1.1 Introduction to *In vivo* amperometric Biosensors and the importance of FDPGOs as biological recognition elements

Biosensors are analytical devices that leverage the specificity of biological interactions and catalysts to rapidly quantify analytes in complex mixtures such as blood and tissue with exceptional sensitivity and specificity coupled with high temporal and spatial resolution.[1-7] In these sensors, the specific interaction between an analyte of interest with a biological recognition element, either a binder or enzyme, is registered as a signal via a variety of detection methods. The development of biosensors capable of directly and reliably analyzing the presence of nearly any analyte in any aqueous sample no matter how complex, remains an active area of research. Enormous efforts are directed at both the improvement of existing sensor platforms and the development of new platforms with the goal of expanding the diversity of detectable analytes and practical applications are major focuses. For these reasons, in the last year alone, over 2,800 papers have been published with the term 'biosensor' in their titles and abstracts.

Of particular interest is the development of implantable or wearable biosensors for the continuous and real time *in vivo* monitoring of analytes important for human health. Such important analytes include metabolic intermediates, drugs, and the associated metabolites in humans. Measurements of this kind have only been reliably achieved in a therapeutic context by biosensors employing a flavin-cofactor dependent peroxide generating oxidase (FDPGO) enzyme as the biological recognition element.[1-7] In these biosensors, a layer of immobilized oxidase enzyme reacts with the analyte of interest and molecular oxygen and generates an electroactive hydrogen peroxide byproduct. This peroxide subsequently diffuses to a transduction element, typically a platinum electrode surface held at a potential of approximately

0.6 V where electrochemical oxidation occurs with oxygen as the byproduct.[8] This electrochemical reaction results in a current which is measured at a potentiostats' working electrode[6, 8] (Figure 1-1); subsequent fitting of this current signal to a standard curve allows interpolation of the concentration of the analyte in the sample or tissue of interest. It is important to note that the oxidase reaction and the production of the peroxide is a one-to-one molar relationship, resulting in a direct relationship between the rate of enzyme turnover and the measured electrochemical current. Therefore, the amperometric signal measured potentiostatically at the platinum surface does not require any hyperbolic fitting and all relationships within the measurement are linear (Figure 1-2).[4] An example sensor gram showing the current vs time for two prototype sensors exposed to analyte is show in Figure 1-3

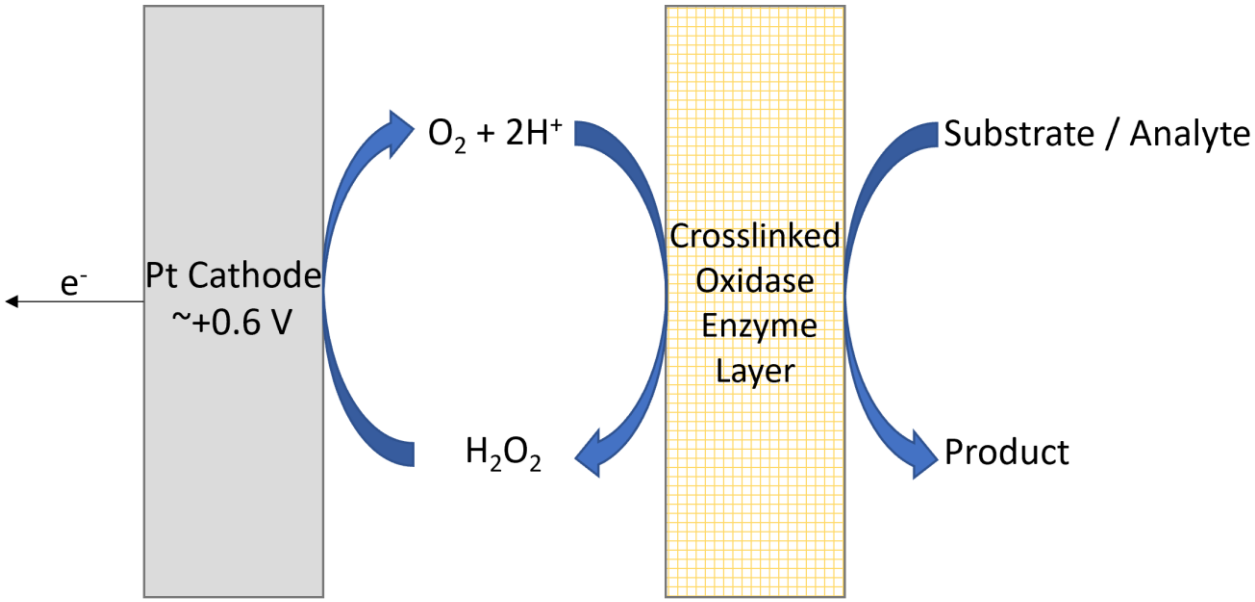

Figure 1-1 Representative diagram of an amperometric enzyme based biosensor system Enzymatically produced H_2O_2 diffuses to the Pt electrode surface where it is electrochemically oxidized, generating a current.

Figure adapted from 'Enzyme Technology', by Martin Chaplin and Christopher Bucke (Cambridge University Press, 1990)

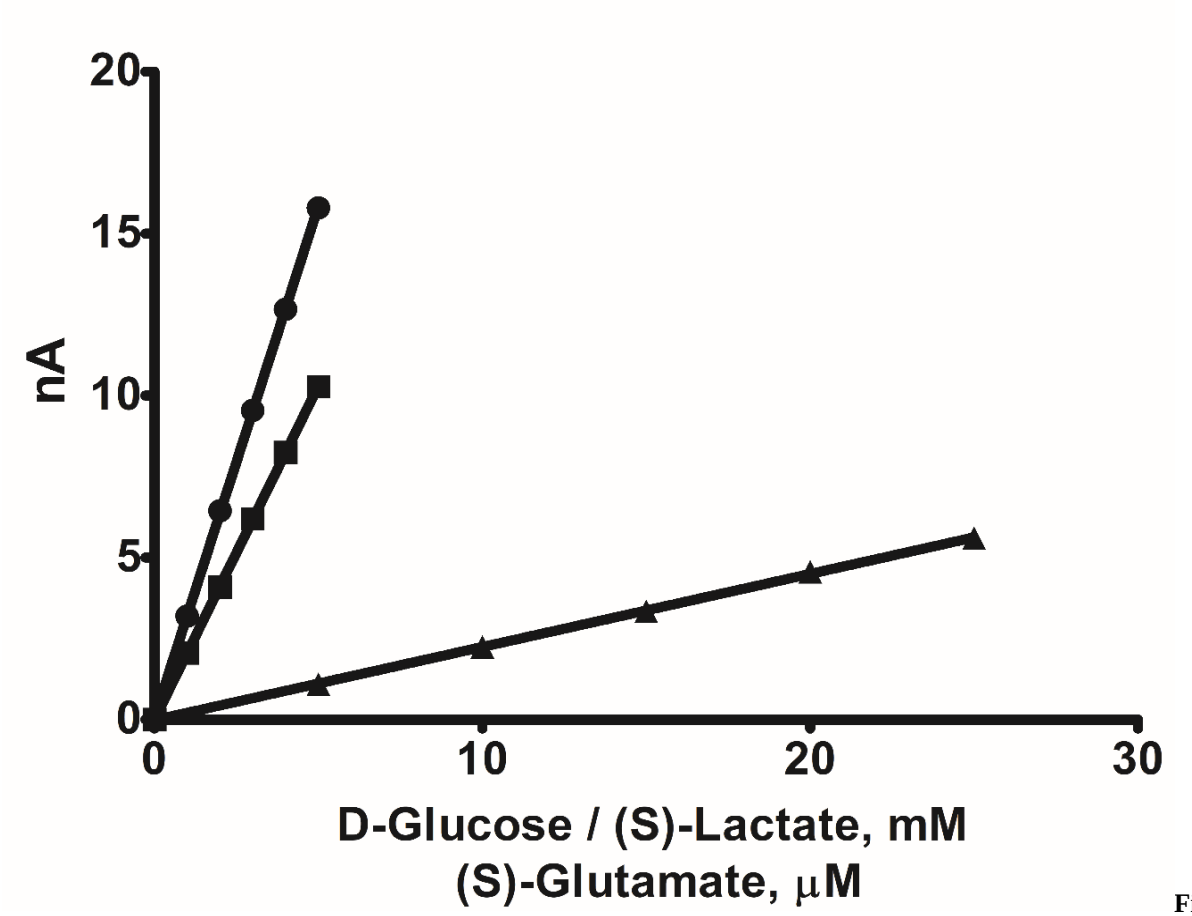

Figure 1-2 Relationship between analyte concentration and current measured by a potentiostat for three representative amperometric biosensors[6] Data points for the D-glucose sensor are shown as circles(●), Data points for the (S)-lactate sensor are shown as squares(■), Data points for the (S)-glutamate sensor are shown as triangles(▲). The current vs analyte concentration demonstrate the linear relationship between analyte added to the test solution and the response of the biosensor.

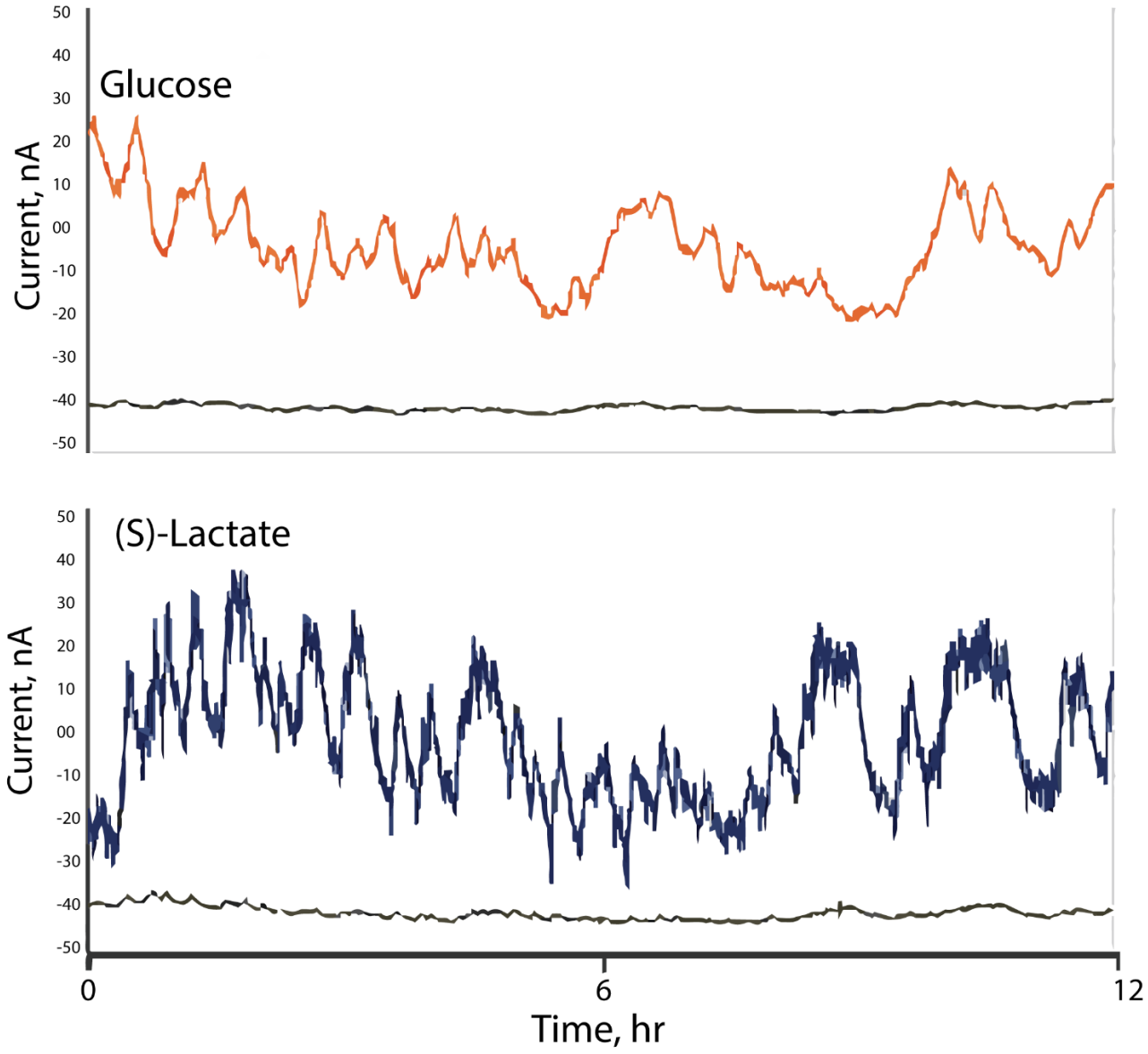

Figure 1-3 ***In vivo*** **sensorgram traces collected from glucose and lactate biosensors implanted in C57/Bl6 mice.** Glucose and (S)-Lactate levels measured simultaneously in a single animal are shown in orange and blue respectively with corresponding negative control sensorgrams shown in black. [9]

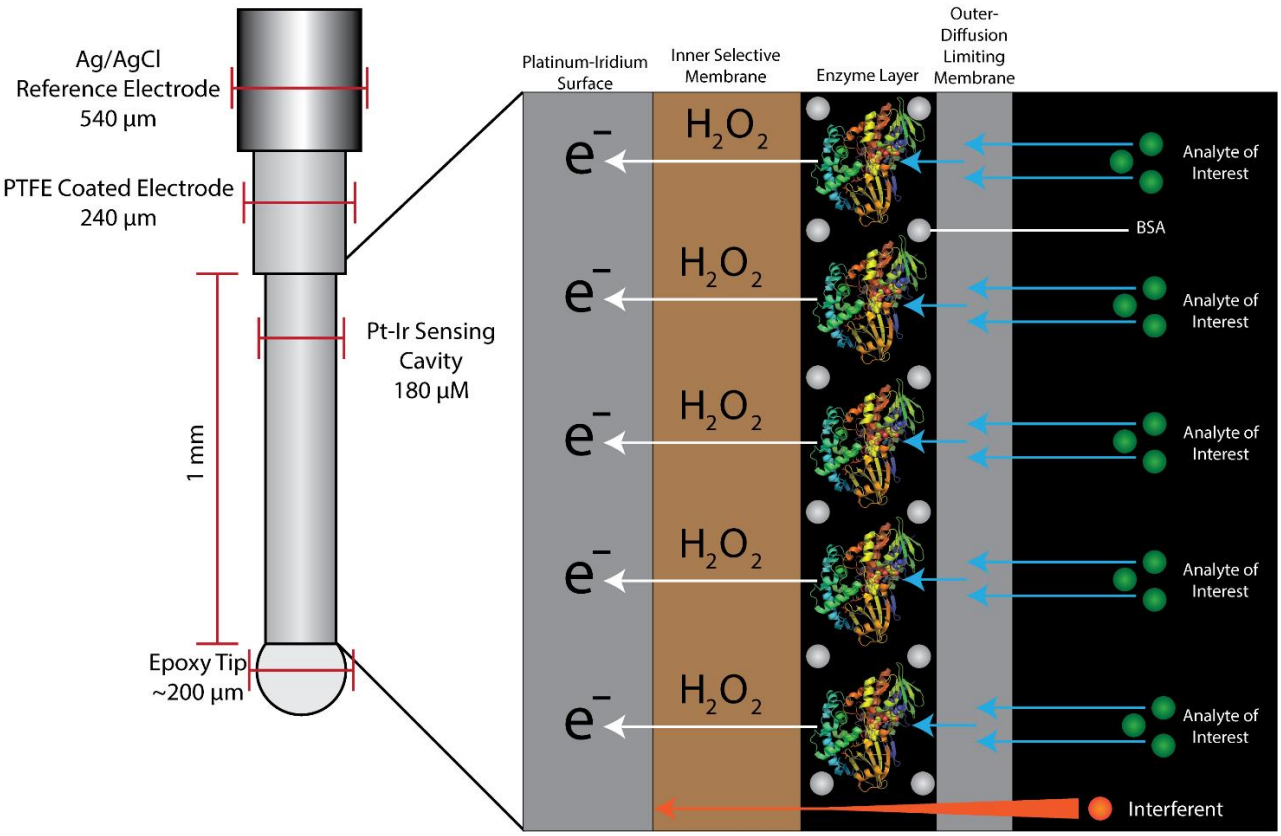

Figure 1-4 Schematic diagram of a contemporary pole electrode based amperometric biosensor for *in vivo* use. This figure is adapted from '*Compendium of In Vivo Monitoring in Real-Time Molecular Neuroscience' by Peter A. Petillo and Erik Naylor,* 2015 [7]

A schematic depiction of a contemporary pole biosensor is shown in Figure 1-4 and an example of simultaneous real time lactate and glucose biosensorgrams collected from a live mouse are shown in Figure 1-3. While many other *in vivo* sensor configurations have shown potential, such as those which employ antibody like binders as the biorecognition element and optical,[10] FET,[11] or capacitive detection,[12] only peroxide based amperometric sensors incorporating FDPGO enzymes as the biorecognition element have thus far demonstrated the requisite properties for continuous real time monitoring of metabolites in humans. Several important properties of an implantable biosensor are responsiveness, reproducibility, reliability, sensitivity, endurance, specificity, reversibility, and biocompatibility.[2, 4, 5] Among these, reproducibility is considered the most important.[13, 14] The significant technical demands of human health monitoring applications account for the failure of the vast majority of biosensor research and development efforts.

While there are many important design considerations when fabricating an amperometric biosensor, the constraints on all other design parameters and the overall sensor performance ultimately depend on the performance of the biological recognition element since the biological recognition element is responsible for signal initiation. The activity and stability of the FDPGO enzymes used should therefore be optimized for *in vivo* performance.

Improvement in enzyme performance provides extra headroom for other design considerations. For example, if enzyme turnover at the anticipated analyte concertation can be increased then the necessary electrode surface area can in theory be proportionally reduced, allowing the sensor to be further miniaturized. Similarly, a sensor constructed with identical dimensions using an improved enzyme will produce a greater initial current; the signal from which will stay above the signal to noise threshold of detection for longer, thereby extending sensor endurance.

The presence of FDPGO enzymes in myriad metabolic pathways has provided researchers with several highly active and reasonably stable oxidases with specificity for metabolites of importance to human health. The existence of these enzymes has allowed for sensor development to proceeded without modification of the enzyme component. Among existing natural enzymes employed in currently available commercial sensors are the glucose oxidase from *Aspergillus niger*[15-17] and the lactate oxidase from *Aerrococcus viridian*s[18].

The glucose oxidase from *Aspergillus niger* is the only example of a FDPGO enzyme that meets the requisite properties for the direct fabrication of a biosensor for *in vivo* use in humans. However, glucose oxidase still has a few functional parameters that are suboptimal for some biosensing applications, and therefore significant effort has gone into improving this, and other,

FDPGO enzymes using directed evolution[19-22] and rational design[23-26] strategies. Directed evolution approaches are attractive for their 'bottom up' ability to find beneficial mutations that current modeling and rational design approaches might overlook. By contrast, rational design approaches permit control over more aspects of protein structure and function without the difficulty of designing and implementing complex biological or *in vitro* selection systems.[27] Ultimately, a combination of both approaches seem to offer the best chance of success at improving functional enzymatic parameters.[27, 28] Importantly, previous protein engineering efforts have improved several FDPGO enzymes, suggesting that other members of this class may also be improved for biosensing applications. By optimizing the stability, turnover, substrate affinity, substrate specificity, co-factor retention, biocompatibility, immunogenicity and manufacturability of FDPGOs, it will be possible to continuously sense an ever-expanding list of analytes with high temporal and spatial resolution *in vivo*.

The FDPGO enzyme family has several attractive advantages for *in vivo* biosensing applications, including the durability of their redox co-factors for extended *in vivo* use. In contrast to other oxidase enzyme families, which employ lysylquinone or heme groups as redox co-factors, FDPGO enzymes employ either FAD or FMN to mediate the redox reactions they catalyze.[29] These co-factors are generally tightly bound or, in some cases, covalently bound to the oxidase. For that reason, FDPGOs are often purified with high co-factor occupancy. This is an important characteristic since co-factor loss by dissociation from the enzyme followed by diffusion into tissue will clearly result in irreversible inactivation of the biological recognition element and a proportional reduction of the biosensor output signal, thereby limiting the useful life of the device. Additionally, unlike other oxidase co-factors, the flavin nucleotides can turn over many times before being broken down by side reactions with molecular oxygen.

Furthermore, the absorbance and florescence signatures of the flavin co-factors also enable spectroscopic collection of detailed kinetic data which improve our understanding of the mechanisms underlying FDPGO activity and so assist efforts to improve these enzymes.

However, because the requirements for an enzyme used in biosensing do not overlap with the requirements for the evolutionary fitness of the host organism, extant FDPGO enzymes frequently suffer from one or more of a variety of shortcomings that can compromise their viability as detection elements. For example, many FDPGOs suffer from an unacceptably high rate of co-factor dissociation, excessive cost of manufacture, or insufficient thermal stability. It is also worth noting that too low of a K_m can, perhaps counterintuitively, result in a sensor that saturates at low analyte concentrations and thus fails to give a linear current response over the analyte concentration range being monitored

1.2 Nicotine biosensing

Nicotine is the third most frequently consumed psychoactive drug on the planet and is responsible for the highest level of global mortality of any drug of abuse, causing over 1 death for every 1000 people globally.[30] Each year, more than 7 million people die globally from health complications related to nicotine use, mostly caused by smoking tobacco products.[31] Primary research into the underlying mechanisms of nicotine dependence in the central nervous system (CNS) is therefore critical if the potential deaths of millions of people over the coming decades are to be prevented. Better understanding of the complex neurochemistry of nicotine adaptation in the CNS will help scientists develop better small molecule and biological therapies that mitigate the pathological changes nicotine causes in the brain that are make cessation of nicotine self-administration (e.g., smoking) exceptionally difficult.

These efforts are complicated by a poor understanding of the spatial and temporal distribution of nicotine in the CNS. Contemporary techniques, such as micro-dialysis, have had limited success and therefore implantable biosensors represent an attractive alternative to address this gap in knowledge. High temporal resolution methods are critical for this task because nicotine concentrations in the brain change rise and fall rapidly during administration, with brain nicotine levels reaching their peak within two minutes after a single inhalation of cigarette smoke.[32] Development of methods for measuring nicotine in real time in the CNS with high temporal resolution could allow for better correlation between nicotine concentration changes in the CNS with critical neurochemical events, including the activation of nicotinic acetyl-choline receptor, which is ultimately responsible for the euphoria and sense of well-being brought on by nicotine consumption.[33]

Clearly, enzymes that efficiently breakdown nicotine would be of great value for the *in vivo* detection of nicotine levels via an amperometric biosensor.[34-36] Additionally, significant demand exists for enzymes capable of degrading nicotine *in vivo,*[37-42] in particular for the enzymatic breakdown of nicotine prior to entry into the CNS.[38, 39, 43] The remediation of toxic industrial waste streams generated during the manufacture of tobacco products is also a potential *ex vivo* application of such an enzyme[44] .

The use of a FDPGO enzyme for the blockade of an addictive drug from the CNS is novel and results from these animal studies are promising. Early successes has prompted the field to turn their focus from establishing proof of concept in animal models to optimization of the enzyme for use in humans. While some of these efforts have focused on increasing circulatory half life[45] and decreasing immunogenicity[46], increasing the oxidative turnover remains a top priority of the field. A high rate of turnover within the pharmacologically relevant concertation range of

(S)-nicotine *in vivo* is a mutual requirement of both biosensing and therapeutic applications. Consequently, the significance of work towards a more efficient nicotine oxidase is amplified by its impact on both fields.

In Chapters 2 and 4 of this dissertation, work is presented which describes the improvement of the kinetic parameters of three nicotine oxidase via rational design approaches. The dissertation work presented in Chapter 2 has been previously published in the peer reviewed Journal of Biochemistry[34] while the work presented in Chapter 3 has been submitted to a peer reviewed journal, *ACS Biochemistry*, for review.

1.3 Biosensor enzyme immobilization strategies

Since amperometric biosensors rely on the electrochemical oxidation of the hydrogen peroxide product generated by the FDPGO to generate a detectable current, the enzyme and electrode surface must be proximal to one another for sensitivity and responsiveness. Additionally, for a biosensor to function for any length of time *in vivo*, the desorption and diffusion of the enzyme away from the electrode surface must be prevented. Accomplishing this task in a manner that does not inactivate the enzyme or sequester it from the chemical environment has proven to be challenging.[47] Contemporary biosensor construction employs crosslinking reactive aldehyde compounds like glutaraldehyde to immobilize the enzyme into a covalent matrix. Despite the success of this method, the activity of the enzyme is inevitably compromised. Many enzyme molecules do not survive the process with their catalytic activity intact due to crosslinking induced denaturation, covalent inactivation, or through steric occlusion of active sites by crosslinked enzyme molecules.[16, 47-49] Some studies have suggested that greater than 90% of the enzyme molecules crosslinked with glutaraldehyde are inactive.[9]

Chapter 3 of this dissertation presents work previously published by the author in the peer reviewed journal, *ACS Langmuir,* that describes the engineering of a gold binding putrescine oxidase by genetic fusion to a gold binding peptide and analysis of its interaction with gold surfaces and nanoparticles.[50] This engineered enzyme was subsequently shown to have been successfully immobilized on a gold surface in an orientation controlled manner. This work advances the feasibility of self assembly of FDPGO enzymes on the surface of biosensor electrodes in a durable fashion without the use of any crosslinking agents. The advantages of this approach over aldehyde crosslinking methods include the lack of enzyme inactivation due to modification of the enzyme's covalent structure, the construction of oriented enzyme layers in which the distance between the active site and the electroactive surface are minimized, and the possibility of self assembly of multi analyte sensors through electrode material specific peptide tags.

1.5 Bibliography

1. Wilson, G. S.; Gifford, R., Biosensors for real-time in vivo measurements. *Biosens Bioelectron* **2005,** *20* (12), 2388-403.

2. Wilson, G. S.; Johnson, M. A., In-Vivo Electrochemistry: What Can We Learn about Living Systems? *Chemical Reviews* **2008,** *108* (7), 2462-2481.

3. Willner, I., Biomaterials for sensors, fuel cells, and circuitry. *Science* **2002,** *298*, 2407-2409.

4. Wilson, G. S.; Gifford, R., Biosensors for real-time in vivo measurements. *Biosens. Bioelectron.* **2005,** *20* (12), 2388-2403.

5. Wilson, G. S.; Hu, Y., Enzyme-based biosensors for in vivo measurements. *Chem. Rev* **2000,** *100* (7), 2693-2704.

6. Naylor, E.; Aillon, D.; Barett, B.; Gabbert, S.; Harmon, H.; Turek, F.; Wilson, G.; Johnson, D.; Petillo, P., *LACTATE ACTS AS A PRIMARY ENERGY SOURCE FOR NEURONAL ACTIVITY DURING WAKING AND REM SLEEP*. 2011; p A41-A41.

7. Naylor, E.; Petillo, P. A., USING BIOSENSORS TO PROBE FUNDAMENTAL QUESTIONS OF SLEEP. In *Compendium of In Vivo Monitoring in Real-Time Molecular Neuroscience*, pp 1-26.

8. Naylor, E.; Aillon, D. V.; Gabbert, S.; Harmon, H.; Johnson, D. A.; Wilson, G. S.; Petillo, P. A., Simultaneous real-time measurement of EEG/EMG and L-glutamate in mice: A biosensor study of neuronal activity during sleep. *J Electroanal Chem (Lausanne)* **2011,** *656* (1-2), 106-113.

9. Petillo, P. A., 2021.

10. Damborský, P.; Švitel, J.; Katrlík, J., Optical biosensors. *Essays in Biochemistry* **2016,** *60* (1), 91-100.

11. Vu; Chen, Field-Effect Transistor Biosensors for Biomedical Applications: Recent Advances and Future Prospects. *Sensors* **2019,** *19* (19), 4214.

12. Ertürk, G.; Mattiasson, B., Capacitive Biosensors and Molecularly Imprinted Electrodes. *Sensors* **2017,** *17* (2), 390.

13. Reiterer, F.; Polterauer, P.; Schoemaker, M.; Schmelzeisen-Redecker, G.; Freckmann, G.; Heinemann, L.; Del Re, L., Significance and Reliability of MARD for the Accuracy of CGM Systems. *Journal of Diabetes Science and Technology* **2017,** *11* (1), 59-67.

14. Danne, T.; Nimri, R.; Battelino, T.; Bergenstal, R. M.; Close, K. L.; Devries, J. H.; Garg, S.; Heinemann, L.; Hirsch, I.; Amiel, S. A.; Beck, R.; Bosi, E.; Buckingham, B.; Cobelli, C.; Dassau, E.; Doyle, F. J.; Heller, S.; Hovorka, R.; Jia, W.; Jones, T.; Kordonouri, O.; Kovatchev, B.; Kowalski, A.; Laffel, L.; Maahs, D.; Murphy, H. R.; Nørgaard, K.; Parkin, C. G.; Renard, E.; Saboo, B.; Scharf, M.; Tamborlane, W. V.; Weinzimer, S. A.; Phillip, M., International Consensus on Use of Continuous Glucose Monitoring. *Diabetes Care* **2017,** *40* (12), 1631-1640.

15. Bankar, S. B.; Bule, M. V.; Singhal, R. S.; Ananthanarayan, L., Glucose oxidase - An overview. *Biotechnol. Adv* **2009,** *27* (4), 489-501.

16. Chen, C.; Xie, Q.; Yang, D.; Xiao, H.; Fu, Y.; Tan, Y.; Yao, S., Recent advances in electrochemical glucose biosensors: a review. *RSC Advances* **2013,** *3* (14), 4473.

17. Wilson, R.; Turner, A. P. F., Glucose oxidase: an ideal enzyme. *Biosens. Bioelectron.* **1992,** *7* (3), 165-85.

18. Rathee, K.; Dhull, V.; Dhull, R.; Singh, S., Biosensors based on electrochemical lactate detection: A comprehensive review. *Biochemistry and Biophysics Reports* **2016,** *5*, 35-54.

19. Mano, N., Engineering glucose oxidase for bioelectrochemical applications. *Bioelectrochemistry* **2019,** *128*, 218-240.

20. Yu, E. H.; Prodanovic, R.; Güven, G.; Ostafe, R.; Schwaneberg, U., Electrochemical Oxidation of Glucose Using Mutant Glucose Oxidase from Directed Protein Evolution for Biosensor and Biofuel Cell Applications. *Applied Biochemistry and Biotechnology* **2011,** *165* (7-8), 1448-1457.

21. Minagawa, H.; Yoshida, Y.; Kenmochi, N.; Furuichi, M.; Shimada, J.; Kaneko, H., Improving the thermal stability of lactate oxidase by directed evolution. *Cellular and Molecular Life Sciences* **2007,** *64* (1), 77-81.

22. Ostafe, R.; Prodanovic, R.; Nazor, J.; Fischer, R., Ultra-high-throughput screening method for the directed evolution of glucose oxidase. *Chem Biol* **2014,** *21* (3), 414-21.

23. Holland, J. T.; Harper, J. C.; Dolan, P. L.; Manginell, M. M.; Arango, D. C.; Rawlings, J. A.; Apblett, C. A.; Brozik, S. M., Rational redesign of glucose oxidase for improved catalytic function and stability. *PLoS One* **2012,** *7* (6), e37924.

24. Kaneko, H.; Minagawa, H.; Shimada, J., Rational Design of Thermostable Lactate Oxidase by Analyzing Quaternary Structure and Prevention of Deamidation. *Biotechnology Letters* **2005,** *27* (22), 1777-1784.

25. Hiraka, K.; Kojima, K.; Tsugawa, W.; Asano, R.; Ikebukuro, K.; Sode, K., Rational engineering of Aerococcus viridansl-lactate oxidase for the mediator modification to achieve quasi-direct electron transfer type lactate sensor. *Biosens Bioelectron* **2020,** *151*, 111974.

26. Stoisser, T.; Rainer, D.; Leitgeb, S.; Wilson, D. K.; Nidetzky, B., The Ala95-to-Gly substitution inAerococcus viridansl-lactate oxidase revisited - structural consequences at the catalytic site and effect on reactivity with O2and other electron acceptors. *FEBS Journal* **2015,** *282* (3), 562-578.

27. Chen, R., Enzyme engineering: rational redesign versus directed evolution. *Trends Biotechnol* **2001,** *19* (1), 13-4.

28. Yip, S. H.; Foo, J. L.; Schenk, G.; Gahan, L. R.; Carr, P. D.; Ollis, D. L., Directed evolution combined with rational design increases activity of GpdQ toward a non-physiological substrate and alters the oligomeric structure of the enzyme. *Protein Eng Des Sel* **2011,** *24* (12), 861-72.

29. Müller, F., *Chemistry and biochemistry of flavoenzymes*. CRC Press: Boca Raton, 1991; p v. <1-3 >.

30. Peacock, A.; Leung, J.; Larney, S.; Colledge, S.; Hickman, M.; Rehm, J.; Giovino, G. A.; West, R.; Hall, W.; Griffiths, P.; Ali, R.; Gowing, L.; Marsden, J.; Ferrari, A. J.; Grebely, J.; Farrell, M.; Degenhardt, L., Global statistics on alcohol, tobacco and illicit drug use: 2017 status report. *Addiction* **2018,** *113* (10), 1905-1926.

31. Region, W. H. O.; Americas, W. H. O.; Region, W. H. O.; Region, W. H. O.; Region, W. H. O.; Region, W. H. O.; Geneva, W. H. O.; Agarwal, N., *WHO REPORT ON THE GLOBAL TOBACCO EPIDEMIC, 2017, Monitoring tobacco use and prevention policies*. 2017.

32. Rose, J. E.; Mukhin, A. G.; Lokitz, S. J.; Turkington, T. G.; Herskovic, J.; Behm, F. M.; Garg, S.; Garg, P. K., Kinetics of brain nicotine accumulation in dependent and nondependent smokers assessed with PET and cigarettes containing 11C-nicotine. *Proceedings of the National Academy of Sciences* **2010,** *107* (11), 5190-5195.

33. Mansvelder, H. D.; McGehee, D. S., Cellular and synaptic mechanisms of nicotine addiction. *Journal of Neurobiology* **2002,** *53* (4), 606-617.

34. Deay, D. O.; Colvert, K. K.; Gao, F.; Seibold, S.; Goyal, P.; Aillon, D.; Petillo, P. A.; Richter, M. L., An active site mutation in 6-hydroxy-l-Nicotine oxidase from Arthrobacter nicotinovorans changes the substrate specificity in favor of (S)-nicotine. *Archives of Biochemistry and Biophysics* **2020,** *692*, 108520.

35. Smith, T. T.; Rupprecht, L. E.; Denlinger-Apte, R. L.; Weeks, J. J.; Panas, R. S.; Donny, E. C.; Sved, A. F., Animal Research on Nicotine Reduction: Current Evidence and Research Gaps. *Nicotine & Tobacco Research* **2017,** *19* (9), 1005-1015.

36. Carroll, D. M.; Murphy, S. E.; Benowitz, N. L.; Strasser, A. A.; Kotlyar, M.; Hecht, S. S.; Carmella, S. G.; McClernon, F. J.; Pacek, L. R.; Dermody, S. S.; Vandrey, R. G.; Donny, E. C.; Hatsukami, D. K., Relationships between the Nicotine Metabolite Ratio and a Panel of Exposure and Effect Biomarkers: Findings from Two Studies of U.S. Commercial Cigarette Smokers. *Cancer Epidemiology Biomarkers & Prevention* **2020,** *29* (4), 871-879.

37. Tararina, M. A.; Dam, K. K.; Dhingra, M.; Janda, K. D.; Palfey, B. A.; Allen, K. N., Fast Kinetics Reveals Rate-Limiting Oxidation and the Role of the Aromatic Cage in the Mechanism of the Nicotine-Degrading Enzyme NicA2. *Biochemistry* **2021,** *60* (4), 259-273.

38. Kallupi, M.; Xue, S.; Zhou, B.; Janda, K. D.; George, O., An enzymatic approach reverses nicotine dependence, decreases compulsive-like intake, and prevents relapse. *Science Advances* **2018,** *4* (10), eaat4751.

39. Pentel, P. R.; Raleigh, M. D.; Lesage, M. G.; Thisted, T.; Horrigan, S.; Biesova, Z.; Kalnik, M. W., The nicotine-degrading enzyme NicA2 reduces nicotine levels in blood, nicotine

distribution to brain, and nicotine discrimination and reinforcement in rats. *BMC Biotechnology* **2018,** *18* (1).

40. Tang, H.; Zhang, K.; Hu, H.; Wu, G.; Wang, W.; Zhu, X.; Liu, G.; Xu, P., Molecular Deceleration Regulates Toxicant Release to Prevent Cell Damage in Pseudomonas putida S16 (DSM 28022). *mBio* **2020,** *11* (5).

41. Tararina, M. A.; Janda, K. D.; Allen, K. N., Structural Analysis Provides Mechanistic Insight into Nicotine Oxidoreductase fromPseudomonas putida. *Biochemistry* **2016,** *55* (48), 6595-6598.

42. Tararina, M. A.; Xue, S.; Smith, L. C.; Muellers, S. N.; Miranda, P. O.; Janda, K. D.; Allen, K. N., Crystallography Coupled with Kinetic Analysis Provides Mechanistic Underpinnings of a Nicotine-Degrading Enzyme. *Biochemistry* **2018,** *57* (26), 3741-3751.

43. Xue, S.; Schlosburg, J. E.; Janda, K. D., A New Strategy for Smoking Cessation: Characterization of a Bacterial Enzyme for the Degradation of Nicotine. *Journal of the American Chemical Society* **2015,** *137* (32), 10136-10139.

44. Briški, F.; Kopčić, N.; Ćosić, I.; Kučić, D.; Vuković, M., Biodegradation of tobacco waste by composting: Genetic identification of nicotine-degrading bacteria and kinetic analysis of transformations in leachate. *Chemical Papers* **2012,** *66* (12).

45. Xue, S.; Kallupi, M.; Zhou, B.; Smith, L. C.; Miranda, P. O.; George, O.; Janda, K. D., An enzymatic advance in nicotine cessation therapy. *Chem Commun (Camb)* **2018,** *54* (14), 1686-1689.

46. Thisted, T.; Biesova, Z.; Walmacq, C.; Stone, E.; Rodnick-Smith, M.; Ahmed, S. S.; Horrigan, S. K.; Van Engelen, B.; Reed, C.; Kalnik, M. W., Optimization of a nicotine

degrading enzyme for potential use in treatment of nicotine addiction. *BMC Biotechnology* **2019,** *19* (1).

47. Sassolas, A.; Blum, L. J.; Leca-Bouvier, B. D., Immobilization strategies to develop enzymatic biosensors. *Biotechnology Advances* **2012,** *30* (3), 489-511.

48. Guzik, U.; Hupert-Kocurek, K.; Wojcieszyńska, D., Immobilization as a Strategy for Improving Enzyme Properties-Application to Oxidoreductases. *Molecules* **2014,** *19* (7), 8995-9018.

49. Nguyen, H. H.; Lee, S. H.; Lee, U. J.; Fermin, C. D.; Kim, M., Immobilized Enzymes in Biosensor Applications. *Materials* **2019,** *12* (1), 121.

50. Kamathewatta, N. J. B.; Deay, D. O.; Karaca, B. T.; Seibold, S.; Nguyen, T. M.; Tomás, B.; Richter, M. L.; Berrie, C. L.; Tamerler, C., Self-Immobilized Putrescine Oxidase Biocatalyst System Engineered with a Metal Binding Peptide. *Langmuir* **2020,** *36* (40), 11908-11917.

2 An active site mutation in 6-hydroxy-l-Nicotine oxidase from *Arthrobacter nicotinovorans* changes the substrate specificity in favor of (S)-nicotine

2.1 Authorship and Publication Information:

This work by the author was published on 15th October 2020 in *Archives of Biochemistry and Biophysics* Volume 629 under the following title and authorship series and is reproduced here with minor formatting revisions. It is a work contributed to by all listed authors.

Reproduced with permission from Archives of Biochemistry and Biophysics 2020 October 15;692:108520

DOI: 10.1016/j.abb.2020.108520. PMID: 32750321

An active site mutation in 6-hydroxy-L-Nicotine oxidase from *Arthrobacter nicotinovorans* changes the substrate specificity in favor of (S)-nicotine

Dwight O. Deay III[a],1, Kim K. Colvert[b],1, Fei Gao[a], Steve Seibold[a], Priyanka Goyal[a], Daniel Aillon[c], Peter A. Petillo[c], Mark L. Richter*[a],*

[a]Department of Molecular Biosciences, The University of Kansas, Lawrence, KS, 66045, USA
[b]Department of Physical Sciences, Ferris State University, MI, 49307, USA
[c]Pinnacle Technology Inc, Lawrence, KS, USA
[d]Design-Zyme LLC, Lawrence, KS, USA

2.2 Abstract

The enzyme 6-Hydroxy-l-Nicotine oxidase (HLNO) is a flavin-dependent enzyme that catalyzes the first step in the pyridine pathway of oxidation of nicotine as a source of energy and nitrogen in several bacteria. Recombinant *Arthrobacter nicotinovorans* HLNO also catalyzes oxidation of (s)-nicotine at a low but measurable rate (Fitzpatrick et al., 2016, Biochemistry 55, 697–703). Rational design and bioinformatics approaches, based on the known high-resolution structure of this enzyme (RCSB: 3NG7), were employed to further enhance the catalytic turnover and stability of the enzyme using (S)-nicotine as substrate. The active site residue Tyr311 forms a hydrogen bond with the hydroxyl group of (S)-6-OH-nicotine within the catalytic pocket. Its replacement by a tryptophan residue reduced the k_{cat} for (S)-6-OH-nicotine by more than 6-fold and increased ~1.5-fold. Combining this mutation with two surface mutations that were predicted to enhance enzyme stability, further increased the k_{cat} for nicotine resulting in a comparatively robust oxidation of (s)-nicotine (k_{cat} >1 s^{-1}) at 37 °C, at the same time reducing the specificity for (S)–OH-nicotine (k_{cat}/K_M) by more than 100-fold and increasing that for (S)-nicotine by more than 2-fold. Interestingly, adding a maltose-binding protein (MBP) tag onto the N-terminus of HLNO markedly increased the thermal stability of the enzyme, extending the half-life at 37 °C from ~2 h to ~22 h. This effect was due almost entirely to increased FAD retention, an observation that may prove useful to improve flavin retention in other flavin-dependent monoamine oxidases.

2.3 Introduction

Several microbial species are known to catabolize nicotine as a source of both energy and nitrogen and their catabolic pathways have been studied extensively.[1-9] Two major pathways have emerged from these studies defined by the initial steps involved in oxidation of nicotine as shown in Fig. 1. In the "pyridine pathway", the first enzyme in the series, nicotine dehydrogenase (NDH), places a hydroxyl group on the C6 position of the pyridine ring of (S)-nicotine to form (S)-6-OH-nicotine.[5, 6] The second enzyme, 6-Hydroxy-l-Nicotine oxidase (HLNO)[1], oxidizes the pyrrolidine C–N bond to produce 6-hydroxy-methylmyosmine which rapidly hydrolyses to 6-hydroxy-pseudooxynicotine which is further degraded ultimately to nicotine blue, methylamine and succinic acid.[9, 10] In the second major pathway, the "pyrrolidine pathway", nicotine is oxidized directly by the action of (S)-nicotine oxidase to produce N-methylmyosmine which spontaneously converts to pseudooxynicotine which, via a series of additional enzyme-catalyzed steps, is converted into citric acid cycle intermediates.[7-10] Several variants of these two pathways exist among nicotine degrading microorganisms as reviewed by Gurusamy & Natarajan[9] and Fitzpatrick et al[10]. In this study we have compared the ability of enzymes from both the pyridine and pyrrolidine pathways to oxidize nicotine with a view towards identifying enzymes that oxidize nicotine with sufficient kinetic and stability characteristics for use in bioremediation and biosensing applications.

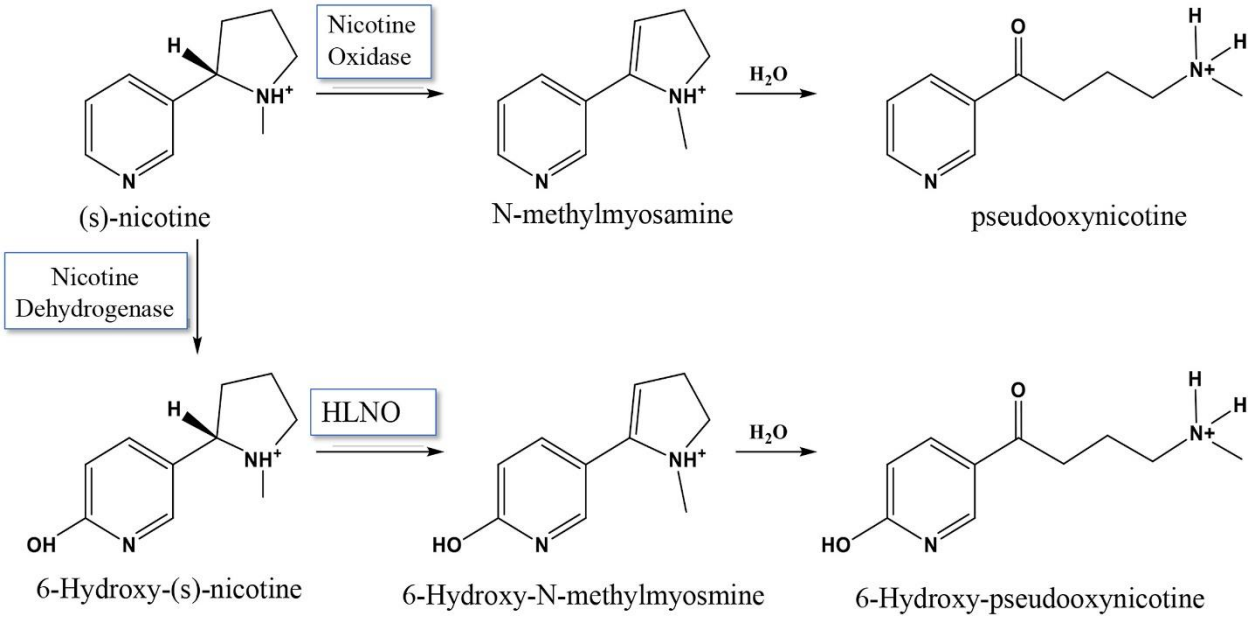

Figure 2-1 Initial steps in nicotine metabolism. In the pyrrolidine pathway, (S)-nicotine is oxidized to N-methylmyosmine by Nicotine Oxidase. In the pyridine pathway, Nicotine Dehydrogenase converts nicotine to (S)-6-hydroxynicotine prior to oxidation by (S)-6-hydroxynicotine oxidase (HLNO)

A recombinant nicotine oxidase (NicA2) from *Pseudomonas putida*, a representative of the pyrrolidine pathway, has been expressed and purified from *E. coli* and its structure determined to 2.2 Å.[11] The enzyme exists as a monomer in solution containing a single FAD co-factor. The steady state catalytic rate constant (k_{cat}) of this enzyme was found to be very low (~6×10^{-3} s^{-1})[11] at ambient temperature although the Michaelis constant (K_M) for the enzyme is in the nanomolar range so that the specificity constant (k_{cat}/K_M) is of the order of 105 s^{-1} M^{-1} [11, 12]. A similar FAD-containing enzyme (NOX) from the *Pseudomonas* Sp. HZN6 strain, which has >80% sequence similarity to NicA2, has also been expressed in recombinant form in *E.* coli[13]. The kinetic properties of this enzyme have not, to our knowledge, been reported. We show here that, apart from the observation that it requires a solubility tag for soluble bacterial expression, the enzyme, as expected, has very similar kinetic properties to those of the NicA2 enzyme.

The first enzyme in the pyridine pathway, OH-nicotine oxidase (HLNO, EC:1.5.3.6) in *Arthrobacter nicotinovorans*, has been isolated and shown to actively oxidize (S)-6-hydroxy-nicotine.[2, 3, 5, 6]The dimeric enzyme uses one non-covalently bound FAD co-factor per subunit in the oxidation reaction.[6, 14] It has been over-expressed in *E. coli*, crystallized, and a high resolution structure obtained[14]. Here we confirm a recent study indicating that HLNO can also catalyze nicotine oxidation.[15] Somewhat surprisingly, the k_{cat} of HLNO with nicotine as substrate is ~30-fold higher than that of the NOX enzyme albeit with a significantly higher K_M . Targeted mutagenesis of active site and surface-exposed residues resulted a substantial activity enhancement along with a significant shift in the specificity of the enzyme toward oxidation of nicotine relative to OH-nicotine. The modified enzyme exhibited a comparatively robust oxidation of nicotine.

Of additional note is that placement of a maltose binding protein (MBP) tag on the N-terminus of HLNO led to a marked increase in the thermal stability of the enzyme following prolonged incubation at 37 °C. The increased stability was found to result almost entirely from an increased retention of the FAD co-factor. This latter observation may prove to be of general significance in stabilizing flavin monoamine oxidases, especially those with a high tendency to lose their flavin co-factors during isolation and purification.

2.4 Materials and Methods

2.4.1 Materials. DEAE cellulose, antibiotics (ampicillin, tetracycline, and chloramphenicol), Sephadex G-50 resin, (S)-nicotine, horseradish peroxidase were purchased from Sigma Aldrich. Ni-NTA resin was purchased from Qiagen. FAD was obtained from TCI, Ltd. and 10-acetyl-3,7-dihydroxyphenoxazine from Cayman Chemical. DNA primers were obtained from Integrated DNA Technologies (Iowa). Benzonase was purchased from EMD Millipore.

2.4.2 Gene constructs and protein expression DNA encoding the NOX enzyme from *Pseudomonas* sp. strain HZN6 was obtained from Integrated DNA Technologies as a DNA fragment encoding the full-length protein. DNA encoding the HLNO enzyme of *Arthrobacter nicotinovorans* was prepared from genomic DNA using standard procedures[16] and was used as the target sequence for the synthesis of a PCR fragment comprising the HLNO gene[17, 18]. Both genes were cloned into the pTBSG1 vector which incorporated a His6 tag on the N-terminus of the protein using a ligation independent cloning method.[17] The resulting plasmids, pTBSG1 hzn6nox and pTBSG1 hlno, were transformed into competent *E. coli* XL10 Gold cells (Agilent Technologies). The plasmids were also cloned into the LIC expression vector pTMal incorporating an N-terminal maltose binding protein (MBP) tag upstream of the cloning site as indicated in Fig. 1.[17]

The sequence of each new gene construct was confirmed commercially (ACGT Inc.). Sequenced plasmids were transformed into the expression host *E. coli* BL21 (DE3) pRARE which were grown to mid-exponential phase in Luria broth, and over-expression of mutant enzymes induced by addition of isopropylthiogalactoside to 0.1 mM followed by incubation overnight at 20 °C in a shaking incubator. Cells were harvested by centrifugation at 5,000×g for 10 min, frozen at −80 °C overnight, thawed and resuspended in lysis buffer (50 mM sodium

phosphate, pH 7.4, containing 0.3 M NaCl) containing benzonase (5 U/mL of lysate) and imidazole-HCl to 10 mM. Cell suspensions were sonicated for 4 min on ice using an alternating 10 s on/10 s off duty cycle. Insoluble material was removed by centrifugation at 10,000×g for 30 min at 4 °C. The soluble cell fraction was applied to a 1.6 × 2.5 cm column of NiNTA resin equilibrated in lysis buffer plus 10 mM imidazole. The column was washed with 10 column volumes of lysis buffer containing 20 mM imidazole. The enzyme was eluted with lysis buffer containing 0.25 M imidazole and peak protein fractions pooled, glycerol added to 20% (v/v), and flash frozen in liquid nitrogen for storage at −80 °C.

Gel electrophoresis was performed under reducing conditions on pre-cast NuPage@ (Invitrogen, San Diego) 12% acrylamide gels with each lane containing approximately 5 μg of protein. Protein concentrations were determined in triplicate by the Bradford method[19].

2.4.3 Oxidase assays Oxidase assays measured the amount of hydrogen peroxide formed during the enzymatic oxidation of OH-nicotine or nicotine using the Amplex Red coupled enzyme assay.[20] The assay mixture contained, in 50 mM potassium phosphate, pH 7.4, 50 μM 10-acetyl-3,7-dihydroxyphenoxazine (Amplex red), 0.1 U/mL of horse radish peroxidase and varying concentrations of nicotine or OH-nicotine. The concentrations of enzymes used are given in the figure legends. Unless stated otherwise, incubations were performed in triplicate at 22 °C. Note that the final concentration of nicotine in these studies was limited to 30 mM due to apparent inhibition at higher concentrations. Kinetic parameters were obtained by fitting the data to the Michaelis Menten equation using the GraphPad Prizm™ software. The flavin content of enzymes was measured using the published molar extinction coefficient for FAD at 450 nm (ε_M = 11,300) following release from the enzyme by heat treatment [21]. Values of k_{obs} (μmol substrate oxidized per μmol enzyme per sec) obtained experimentally were corrected for FAD content by dividing them by the calculated fraction (mol/mol) of FAD occupancy.

2.4.4 Substrate docking and surface mutant prediction Nicotine and OH-nicotine docking studies were performed using the genetic algorithm implemented by Autodock 4[22, 23] Models were generated using the high resolution crystal structure of the *A. nicotinovorans* HLNO (PDB entry: 3NG7) and manually introducing nicotine or OH-nicotine into the general area of the active site and identifying the "best fit" (lowest energy) orientations. This method allows examination of the possible range of conformations that are energetically favorable for the substrate binding in the active site.

The program I-Mutant2.0 predicts, with high accuracy, single point mutations likely to increase stability of already folded proteins[24]. In this study, the solved structure of HLNO was introduced, via the PDB identifier, through the I-Mutant2 website which identified five point

mutations that were predicted to enhance stability. These five proteins formed the basis of site-directed mutations as described in the Results.

2.5 Results

2.5.1 Bacterial over-expression of nicotine-degrading enzymes Four gene constructs were prepared as described in the Materials and Methods and are depicted in Fig. 2. All four contained an N-terminal 6-histidine tag for affinity purification and two contained an additional N-terminal maltose binding protein (MBP) tag to enhance soluble protein expression. Short linker sequences were included to encode a tobacco etch virus (TEV) protease cleavage site (Fig. 2). The two HLNO constructs and the MBP-NOX construct over-expressed in significant amounts (10–100 mg protein/liter of growth medium). The NOX protein without the MBP tag failed to express in significant amounts in soluble form. Following nickel affinity purification, the over-expressed MBP-NOX, HLNO and MBP-HLNO proteins were greater than 95% homogeneous as judged by SDS-gel electrophoresis analysis.

2.5.2 The N-terminal MBP tag increases FAD retention Interestingly, adding an N-terminal MBP tag to the HLNO enzyme, intended to increase recovery of soluble enzyme, increased the observed V_{max} of HLNO for OH-nicotine by about 4.5-fold. The increase in activity was almost entirely accounted for by an increase in the occupancy of the flavin co-factor following expression and purification. The FAD content of freshly prepared wild type HLNO lacking the tag varied significantly from batch to batch, averaging 0.17 mol FAD per mol enzyme. In contrast, the FAD content of MBP-HLNO averaged 0.8 mol FAD per mol of enzyme. Following this observation, all subsequent reported activities were corrected for the FAD content of the enzyme according to Mayhew and Tollin[21].

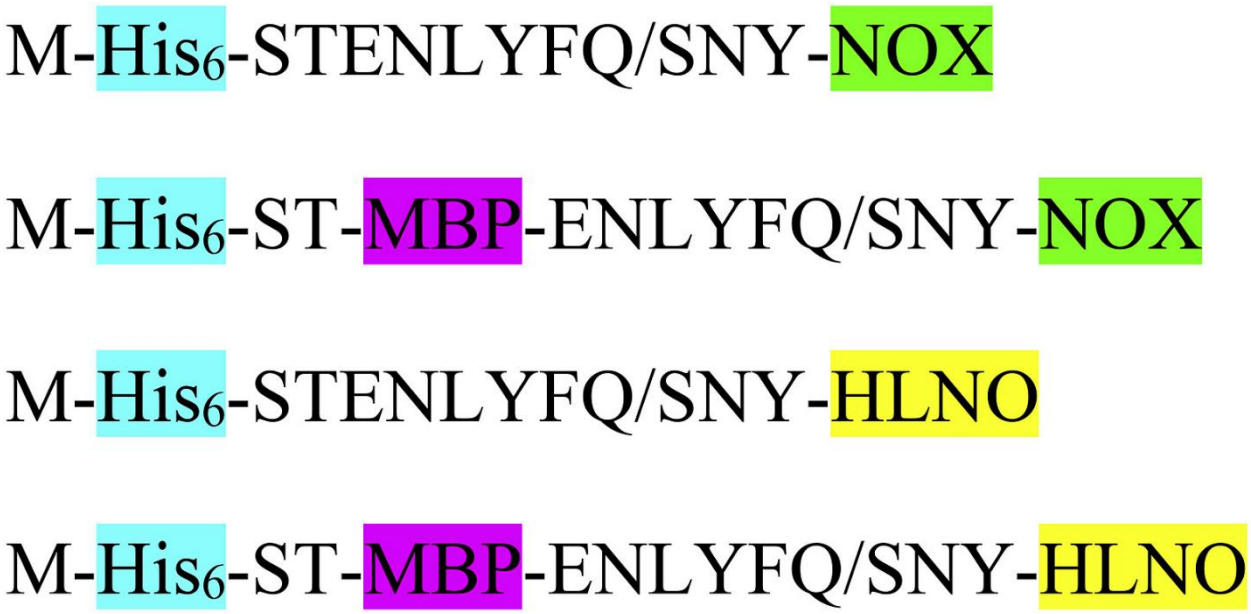

Figure 2-2 Gene Constructs All constructs incorporated a 6 histidine N-terminal tag and a short linker encoding a tobacco etch virus (TEV) protease cleavage site (slash). NOX, l-nicotine oxidase from *Pseudomonas Sp.* HZN6; HLNO, 6-OH-l-nicotine oxidase from *Arthrobacter nicotinovorans*; MBP, maltose binding protein.

2.5.3 Nicotine Oxidation The catalytic properties of the three constructs expressed in soluble form were measured using the sensitive Amplex Red™ coupled enzyme assay[20] that measures the peroxide generated during the reaction. The majority of measurements were performed in 50 mM sodium phosphate buffer at pH 7.4 at 22 °C. The wild type HLNO oxidized its natural substrate 6-OH-nicotine at a relatively high rate (k_{cat} ~56 s^{-1}) with a Michaelis constant of ~60 μM (Fig. 3A, Table S1), consistent with previous measurements[6]. The enzyme also oxidized (S)-nicotine at a low but measurable rate (k_{cat} ~0.1 s^{-1}) with an apparent K_M of ~13 mM (Fig. 3B, Table S1). The observation that (S)-nicotine is also a substrate for HLNO was reported previously measuring oxygen depletion.[15] In that case the k_{cat} was similar to that obtained here whereas the apparent K_M for (S)-nicotine was ~an order of magnitude lower.[15] In contrast, the measured k_{cat} for the NOX enzyme was more than 30-fold lower than that obtained for oxidation of (s)-nicotine by HLNO (Table S1). The K_M for (S)-nicotine for NOX was found to be less than 1 μM. These properties are very similar to those reported previously for the analogous NicA2 enzyme from *Pseudomonas putida* S16[7, 11] which is not surprising since these enzymes share more than 80% sequence similarity[13].

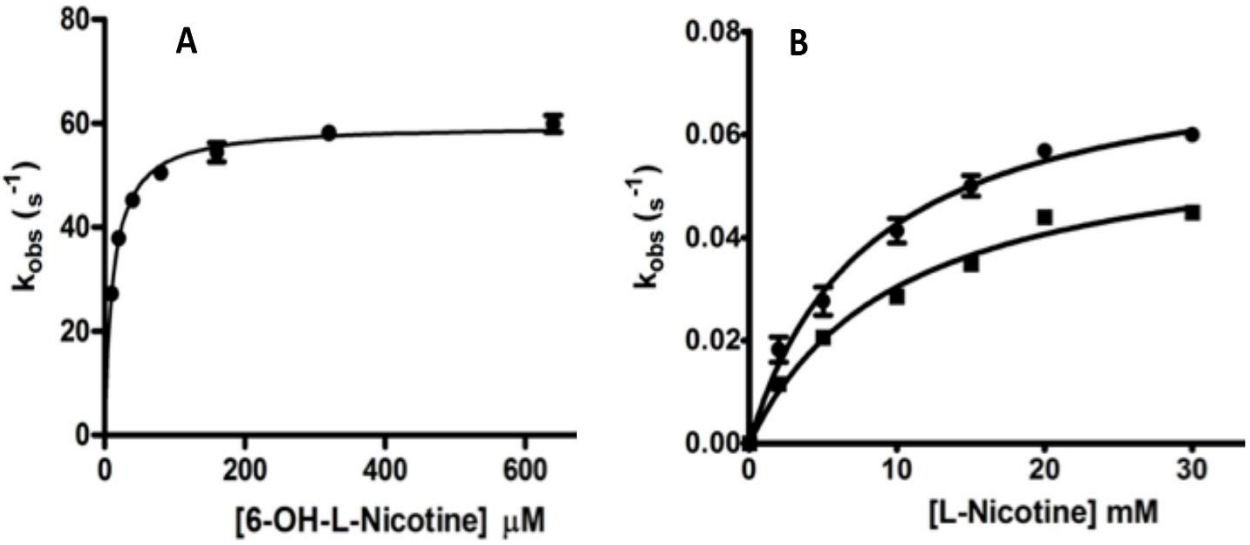

Figure 2-3 (S)-OH-nicotine and (S)-nicotine oxidation by HLNO. A) rate of OH-nicotine oxidation by HLNO; **B**) comparison of rates of nicotine oxidation by HLNO (circles) and MBP-HLNO (squares). Rates were corrected for FAD content as described in the Materials and Methods. Assays were performed at 22 °C in 1mL of assay mixture containing 0.2 mg of HLNO or MBP-HLNO equivalent, for nicotine oxidation assays and 10 μg of HLNO for OH-nicotine oxidation assays. Error bars represent standard deviations for three independent measurements. K_{obs} s^{-1} =mol of substrate oxidized per second per mol of enzyme.

2.5.4 An active site HLNO mutant Tyr311Trp increases turnover Nicotine and (S)-6-hydorxy-nicotine docking studies were performed using the genetic algorithm implemented by Autodock 4[22, 23]. Models were generated using the high resolution crystal structure of the *A. nicotinovorans* HLNO and manually introducing nicotine or OH-nicotine into the general area of the active site and identifying the "best fit" (lowest energy) orientations. This method allows examination of the possible range of conformations that are energetically favorable for the substrate binding in the active site. As in the reported crystal structure, OH-nicotine low energy (high affinity) structures assumed a single unique conformation in which C2' carbon atom of the OH-nicotine substrate is juxtaposed with the N5 of the isoalloxazine ring of the FAD, present in the oxidized form, which would be optimal for hydride transfer. The hydroxyl group and the pyridyl ring nitrogen of OH-nicotine undergo hydrogen bonding interactions with the hydroxyl of Tyr311 and the carbonyl oxygen and amide nitrogen of Asn166 within the active site as indicated in Fig. 4A. All of these features are identical to those seen in the high-resolution crystal structure of HLNO[14].

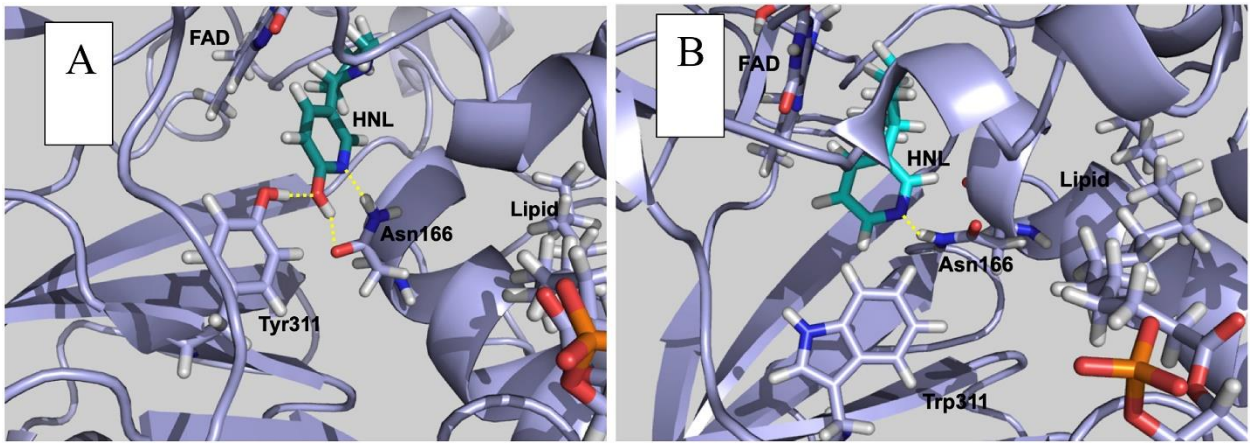

Figure 2-4 (S)-6-OH-nicotine and (S)-nicotine Bound in the Active Site of HLNO. (S)-6-OH-nicotine (HNL in panel **A)** and (S)-nicotine (HNL) in Panel **B)** were docked into the active site of HLNO using Autodock 4[22]. The most energetically favorable conformations are shown together with the hydrogen bonding interactions between the pyridine ring of the substrate and nearby Tyr311 and Asn166. The single molecule of glycolipid that co-crystallizes with the enzyme close to the active site is also indicated.

In contrast to OH-nicotine, nicotine was predicted to adopt a broad ensemble of conformations in which a catalytically favorable conformation was rarely achieved. In the most favorable conformation, nicotine forms only a single hydrogen bond between the carbonyl oxygen of Asn166 and the amide nitrogen of the pyridine ring (Fig. 4B) with a calculated binding energy of −6.9 kcal mol^{-1} which is more than 1 kcal mol^{-1} less favorable than OH-nicotine (−8.1 kcal mol^{-1}).

Site-specific mutation of Tyr311 to tryptophan was predicted to reduce the binding affinity of HLNO for OH-nicotine by eliminating the stabilizing hydrogen bonding interaction between the Tyr hydroxyl and that of OH-nicotine and replacing it with the hydrophobic edge of the tryptophan. The increased bulk of tryptophan at this site was also predicted to fill the void left by the loss of the hydroxyl group on nicotine. By comparison, the simulations predicted a greater than five-fold increase in the number of favorable binding conformations over less favorable ones for nicotine in the Tyr311Trp mutant with an average decrease of −0.15 kcal mol^{-1} in binding energy. The decreased conformational heterogeneity for nicotine in the docking study of this mutant apparently resulted from stabilizing steric interactions between the five-membered ring of nicotine and Met 167, Leu 198 and Trp 407 within the catalytic pocket of the enzyme. The predicted change in favorable binding of nicotine was borne out experimentally. The mutation resulted in an ~40% increase in the k_{cat} using nicotine as substrate (Fig. 5A, Table 1). In contrast, the calculated binding energy for OH-nicotine fell by 0.5 kcal mol^{-1} with a concomitant introduction of a significant number (~25%) of unfavorable binding conformations to the ensemble. Experimentally, this substitution resulted in an ~6-fold decrease in the k_{cat} and an ~6-fold increase in the K_M for OH-nicotine (Table 1), that is, a greater than 60% reduction in the specificity constant for OH-nicotine.

In a second mutation the asparagine at position 166 was substituted with glutamine. This mutation was also rationalized to change the relative binding affinity of the enzyme for OH-nicotine and nicotine by sterically hindering OH-nicotine binding and enhancing nicotine binding by filling the void created by the missing OH group of OH-nicotine with the larger sidechain of glutamine. This mutation slightly reduced the K_M for nicotine as expected, however, it also reduced enzyme turnover by ~5-fold with nicotine as substrate (Fig. 5A, Table 1).

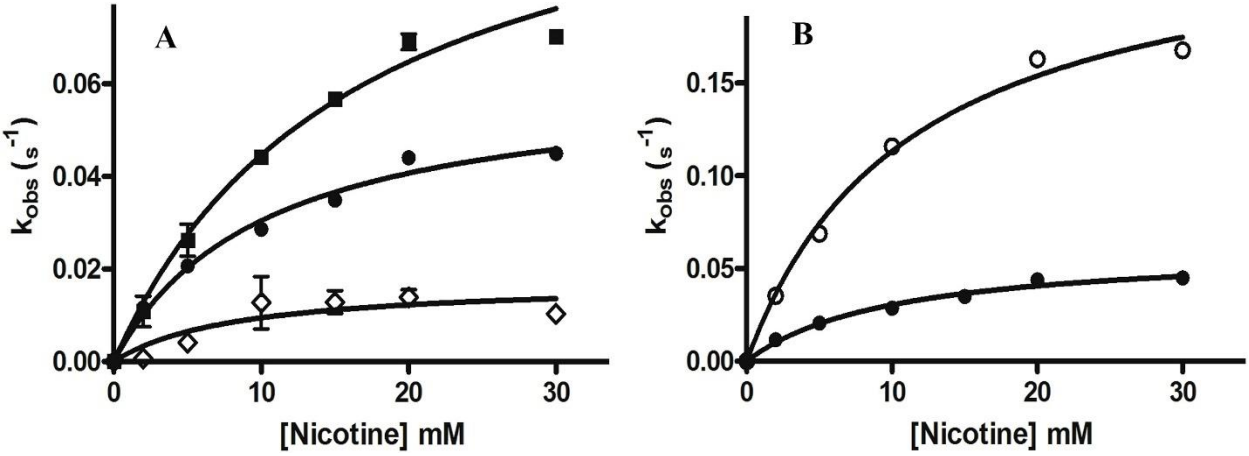

Figure 2-5 Active Site and Surface Mutants of MBP-HLNO. Panel **A**) effects of active site mutations: Tyr311Trp (closed squares); Asn166Gln (open diamonds); compared to wild type (closed circles). Panel **B**) MBP-HLNO triple mutant, R274A/Y311W/C417W (open circles); wild type (closed circles). Assays were performed at room temperature with (S)-nicotine as substrate in 1 mL of assay mix containing 0.2 mg of enzyme. Values were corrected for FAD content as described in the Materials and Methods. $K_{obs}s^{-1}$=mol of substrate oxidized per second per mol of enzyme. Error bars represent standard deviations for three independent measurements.

Table 2-1 Kinetic properties of HLNO mutants.

Enzyme	(S)-nicotine			(S)–OH-nicotine		
	k_{cat} $(sec^{-1})^1$	K_M $(mM)^1$	k_{cat}/K_M $(M^{-1}s^{-1})$	k_{cat} $(sec^{-1})^1$	K_M $(mM)^1$	k_{cat}/K_M $(M^{-1}s^{-1})$
MBP-HLNO	1.00 (±0.03) x 10^{-1}	13 ± 1	7.7	58 ± 2	5.7 (±0.6) x 10^{-2}	1.02×10^6
MBP-HLNO-Y311W	1.44 (±0.03) x 10^{-1}	19 ± 7	7.6	9 ± 1	3.4 (±0.4) x 10^{-1}	2.65×10^4
MBP-HLNO-N166Q	2.10 (±0.07) x 10^{-2}	10 ± 1	2.1	–[2]	–	–
MBP-HLNO-R274A	1.63 (±0.19) $\times 10^{-1}$	27 ± 5	6.0	–	–	–
MBP-HLNO-C417W	1.73 (±0.35) $\times 10^{-1}$	38 ± 5	4.6	–	–	–
MBP-HLNO.triple mutant	2.65 (±0.09) x 10^{-1}	16 ± 1	20.4	2.5 ± 0.3	2.7 (±0.2) x 10^{-1}	9.26×10^3
MBP-HLNO.triple mutant	[3]1.14 ± 0.07	13 ± 2	87.7	–	–	–

[1]Data collected at 22ºC and corrected for FAD content with errors reported as standard deviation, n=3; [2]not determined; ,[3]assayed at 37°C.

2.5.5 Enhanced solubility and turnover introduced by surface mutations The program I-Mutant2.0 was used to predict mutations in HLNO that are likely to result in enhanced stability (24). The program was used to identify a series of surface mutations that were calculated to reduce the overall free energy of folding for wild type HLNO from an estimated 39.43 to 30.26 kcal mol^{-1} when introduced collectively. The mutants: Tyr189Gly; Ile277Gly; Arg274Ala; Ser214Trp and Cys417Trp were introduced into the MBP-HLNO expression construct individually as well as together in a single mutant. Three of the mutants, Tyr189Gly, Ser214Trp and Ile277Gly, as well as the mutant with all five substitutions, were found to be prone to extensive proteolysis and could not be recovered in sufficient quantities for meaningful analysis. The remaining two mutants, Arg274Ala and Cys417Trp, expressed well with yields that were 3 to 5-fold greater than the wild type MBP-HLNO (Table 1).

2.5.6 Integration of mutations for maximal catalytic turnover and increased thermal stability. The three most efficacious mutations, Tyr311Trp, Arg274Ala and Cys417Trp, were combined into a triple mutant and its catalytic properties compared to those of the wild type enzyme with the MBP tag as shown in Fig. 5B and Table 1. The MBP-HLNO triple mutant has a k_{cat} of 0.265 s−1 which is an ~2.7-fold increase over that of the wild type enzyme with only a modest increase in the K_M . The activities of the MBP-NOX, MBP-HLNO and the triple mutant of MBP-HLNO when incubated at 37 °C are also compared in Table 1. The k_{cat} of the MBP-HLNO triple mutant was >1 s^{-1} at 37 °C. By comparison, the k_{cat} of the NOX enzyme under the same conditions was 0.017 s^{-1} (>60-fold lower).

2.5.7 The MBP tag promotes thermal stability and increases FAD retention. Data shown in Fig. 6A, B and C compare the stability of the wild type HLNO, MBP-HLNO and the MBP-HLNO. Y311W mutant during prolonged incubation at 37 °C, 22 °C and 4 °C respectively over a period of 4 h. All three were stable at 4 °C during the course of the experiment and, in fact, for at least a week at this temperature (data not shown). Incubation at the higher temperatures led to significant loss of activity of the wild type HLNO. The enzyme lost 50% of its activity following 2.3 h of incubation at 37 °C whereas the other two enzymes remained relatively stable over the same time period.

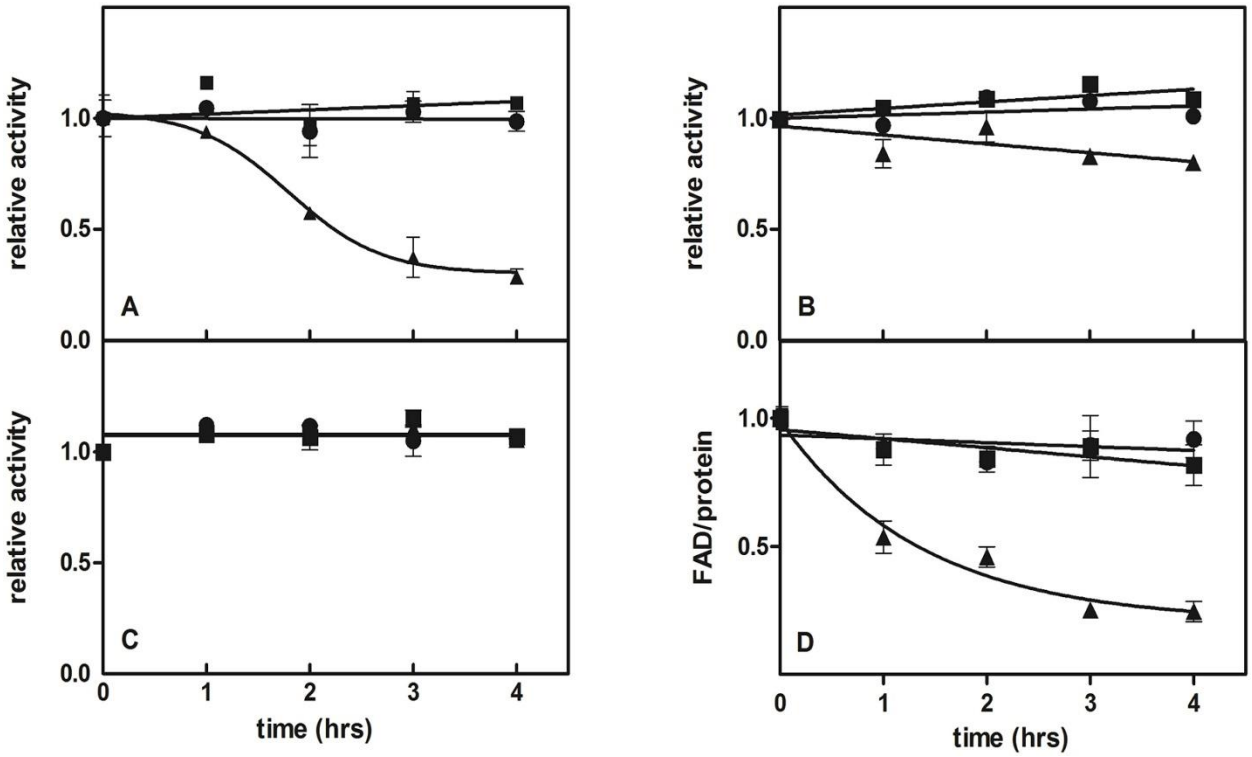

Figure 2-6 Thermal stability of HLNO and MBP-HLNO vs time Freshly isolated HLNO (filled triangles), MBP-HLNO (filled squares) and MBP-HLNO-Y311W (filled circles) were desalted into 50 mM sodium phosphate buffer, pH 7.4 and the FAD content measured. The enzymes were diluted to a final concentration of 0.1 mg/mL and aliquots incubated for 4 h at 37 °C (Panel A), 22 °C (Panel B), or 4 °C (Panel C). In Panel D, the three enzymes were incubated at 37 °C and at the time points indicated, aliquots were removed, desalted on Sephadex G-50 spin columns, and the FAD content determined as described in the Materials and Methods. Data in Panel D were normalized to the initial FAD concentrations. Error bars represent standard deviations for three independent measurements.

In the experiment shown in Fig. 6D the three enzymes were incubated at 37 °C for the indicated times, desalted and the FAD content measured. The results show a good correlation between the temperature-dependent loss of activity and loss of the FAD co-factor during the incubation (compare 5 A and 5D) adding to the earlier observation that the N-terminal MBP tag increases the FAD content of the isolated enzyme. In a separate experiment the stability at 37 °C of the MBP-HLNO and MBP-HLNO triple mutant were compared over an extended period of time. Compared to a half-life of ~2.5 h for HLNO at 37 °C, MBP-HLNO and the MBP-HLNO triple mutant retained 50.7 and 47.6% of their activities respectively at 22.5 h of incubation at 37 °C. Measurement of the melting temperature (Tm) of the HLNO triple mutant and MBP-HLNO by circular dichroism (Fig. S1) indicated an ~5° and ~11° increase respectively in their Tm values relative to wild type HLNO, supporting the contention that increased flavin retention results from increased overall stabilization of HLNO to thermal inactivation.

2.6 Discussion

The NOX enzyme from the pyrrolidine pathway of nicotine metabolism was expressed in recombinant form in *E. coli* along with the OH-nicotine oxidase representing the second step in the pyridine pathway of microbial nicotine metabolism. The NOX enzyme was only expressed in soluble form when attached to an N-terminal MBP tag. The enzyme turned over nicotine very slowly with a sub-micromolar K_M , similar properties to those of the NicA2 enzyme from *P. putida* S16[7-11, 25]. On the basis of the very low k_{cat} value of S16 NicA2 *in vitro*, it has been suggested that the rate at which molecular oxygen accepts electrons from the reduced flavin is very low and that an alternate acceptor may function *in vivo*[8, 11]. The same may be true for the NOX enzyme.

Because of its very low K_M and high specificity for nicotine, the S16 NicA2 enzyme has potential for use in nicotine addiction therapy.[26-30] To this end it was shown that the enzyme significantly reduced the amount of nicotine present in nicotine-dosed serum where concentrations of nicotine were in the nM range[31]. More recent studies have shown that NicA2, fused to an albumin binding domain[28] or to polyethyleneglycol[30], exhibited an extended half-life when injected into mice, effectively reducing circulating nicotine levels in both blood and brain. Further studies aimed at increasing the catalytic turnover of NicA2 through saturation mutagenesis achieved a 3-fold increase in potency in reducing nicotine levels *in vivo*, a significant step toward engineering an enzyme suitable for therapeutic use.[30]

We have shown here that the HLNO enzyme can oxidize nicotine at a rate that is between one and two orders of magnitude greater than those of the S16 NicA2 and NOX enzymes, confirming an earlier observation[15]. Substitution of the active site residue tyrosine at position 311 for tryptophan resulted in a significant increase in the k_{cat} for nicotine as substrate while reducing the specificity constant for OH-nicotine by more than 60-fold. The importance of Y311 in binding OH-nicotine in the active site of HLNO was also examined by Fitzpatrick et al., where they showed that the mutant Y311F resulted in a ~4-fold reduction in the k_{cat}/K_M for OH-nicotine.[32] The even larger reduction in the k_{cat}/K_M for OH-nicotine with the Y311W mutation is consistent with the bulkier tryptophan residue sterically excluding the hydroxyl group on OH-nicotine from occupying its normal position within the active site. On the other hand, the enhanced k_{cat} with nicotine as substrate resulting from substitution of tryptophan for tyrosine at position 311 is likely to have resulted from formation of a stabilizing hydrophobic contact with the nicotine ring which was indeed observed in the docking study to limit conformational flexibility of nicotine within the active site. The additive effect of the two surface mutations on

the k_{cat} of HLNO led to a further reduction in the specificity constant for OH-nicotine (>100-fold) with a concomitant increase in that for nicotine, likely due to a further increased stability as predicted by the IMutant-2 algorithm.

At 37 °C, the k_{cat} of the triple mutant of HLNO is above 1 per second, a level of activity that is expected to generate sufficient H_2O_2 to obtain a measurable amperometric response on an implanted microelectrode at this temperature in the presence of high μM to mM concentrations of nicotine [33-37]. However, the K_M of the combined mutant would limit the sensitivity toward nicotine in biological tissues and fluids of nicotine users which is typically present at sub-micromolar concentrations.[25, 26, 28, 30, 38]

Interestingly, an HLNO-like enzyme was described recently from the *Shinella sp.* HZN7 strain that is also capable of oxidizing nicotine with a k_{cat} similar to that described here for the HLNO.[39] This enzyme was shown to have a K_M for nicotine approximately ~10-fold lower than the *A. nicotinovorans* HLNO and is, therefore, a promising additional target for similar rational design. To pursue this we have solved the structure of the *Shinella* enzyme and are in the process of comparing its structural and kinetic properties to those of the *Actinobacter* enzyme and other family members. The coordinates of the *Shinella* 6-OH-L-nicotine oxidase solved by our group are available in the protein database (RCSB: 6cr0).

Of significance is the observation that adding an MBP tag to the N-terminus of HLNO resulted in an ~4-fold increase in occupancy by the FAD co-factor upon over-expression and isolation of the enzyme. Moreover, the MBP-enhanced FAD retention led to an ~11-degree shift in the melting temperature of the enzyme and an ~10-fold increase in the half-life of the enzyme upon prolonged incubation at 37 °C. One possible explanation for this effect is that, through intramolecular interactions between the fusion tag and the enzyme domain, placement of the

MBP tag on the N-terminus restricts conformational changes that are necessary for FAD release, consistent with the known chaperone-like property of MBP[40, 41]. This hypothesis is consistent with the observation that N-terminal residues 7 through 11 engage in stabilizing non covalent interactions with the bound FAD, where residues 8–13 in particular form a known phosphate binding motif that contributes to flavin binding as indicated in Fig. 7[42, 43]. As this is a common structural feature of monoamine oxidases, adding an N-terminal MBP tag may well work to enhance retention of the bound flavin and thermal stability of other flavin coenzyme containing amine oxidase enzymes. This would be of special significance for applications where loss of the flavin co-factor reduces the utility of the enzyme.

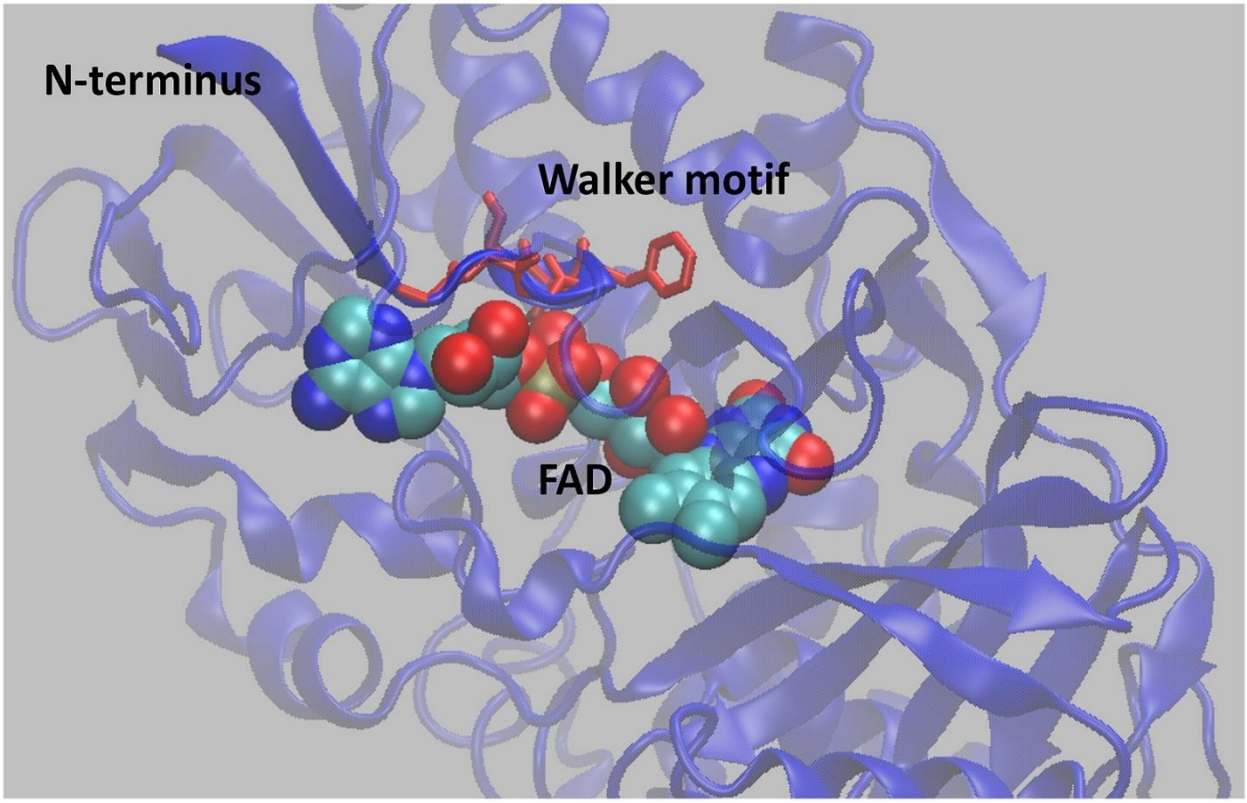

Figure 2-7 Cross section through HLNO highlighting N-terminal residues (dark blue) containing the Walker phosphate binding motif (red) stabilizing bound FAD.

In summary, we have shown that mutations in the *Arthrobacter nicotinovorans* HLNO enzyme resulting from rational design and bioinformatics considerations altered the substrate specificity leading to a significant increase in the rate of nicotine oxidation such that the k_{cat} is ~70-fold greater than those of native nicotine oxidizing enzymes, albeit with a substantially higher K_M . The improved enzyme may be of use in bioremediation applications where high concentrations of nicotine are present. However, for biosensing and substance abuse deterrence, further reduction of the K_M is required. On that basis, the enzyme is an excellent candidate for combining further rational design experiments with directed evolution studies to improve its efficiency at low nicotine concentrations. The significantly enhanced stability toward flavin loss that is afforded by placing an MBP tag on the N-terminus of HLNO, further enhances the suitability of the enzyme for a range of applications that require sustained enzymatic activity over prolonged time periods.

2.7 Funding information

This work was supported by NIH 2R44DA033701-02A1 grant. D. Deay was supported on NIH graduate training grant #5T32GM008359-27.

2.8 Acknowledgement

We would particularly like to thank Dr. Sunil David for generously supplying 6-OH-l-nicotine.

2.9 Supplementary data

Table 2-2 Comparison of **Kinetic** Constants of NOX and HLNO Enzymes

Enzyme	**OH-nicotine**			**nicotine**		
	k_{cat} (s^{-1})[1]	**K_M (mM)**	**k_{cat} /K_M**	**k_{cat} (s^{-1})[1]**	**K_M (mM)**	**k_{cat} /K_M**
MBP-NOX	*nd*[2]	*nd*	-	3.5 (± 0.5) x10^{-3}	< 1 x 10^{-3}	-
WT HLNO	56 ± 2	5.4 (± 0.6) x 10^{-2}	1.04x10^{6} M^{-1} s^{-1}	1.03 (± 0.07) x 10^{-1}	12.6 ± 0.1	8.2 M^{-1} s^{-1}
MBP-HLNO	58 ± 2	5.7 (± 0.6) x 10^{-2}	1.02x10^{6} M^{-1} s^{-1}	1.00 (± 0.03) x 10^{-1}	13 ± 1	7.7 M^{-1} s^{-1}

[1]Data collected at 22°C, values corrected for FAD content with errors reported as standard deviation, n=3;

[2]*nd*, not determined.

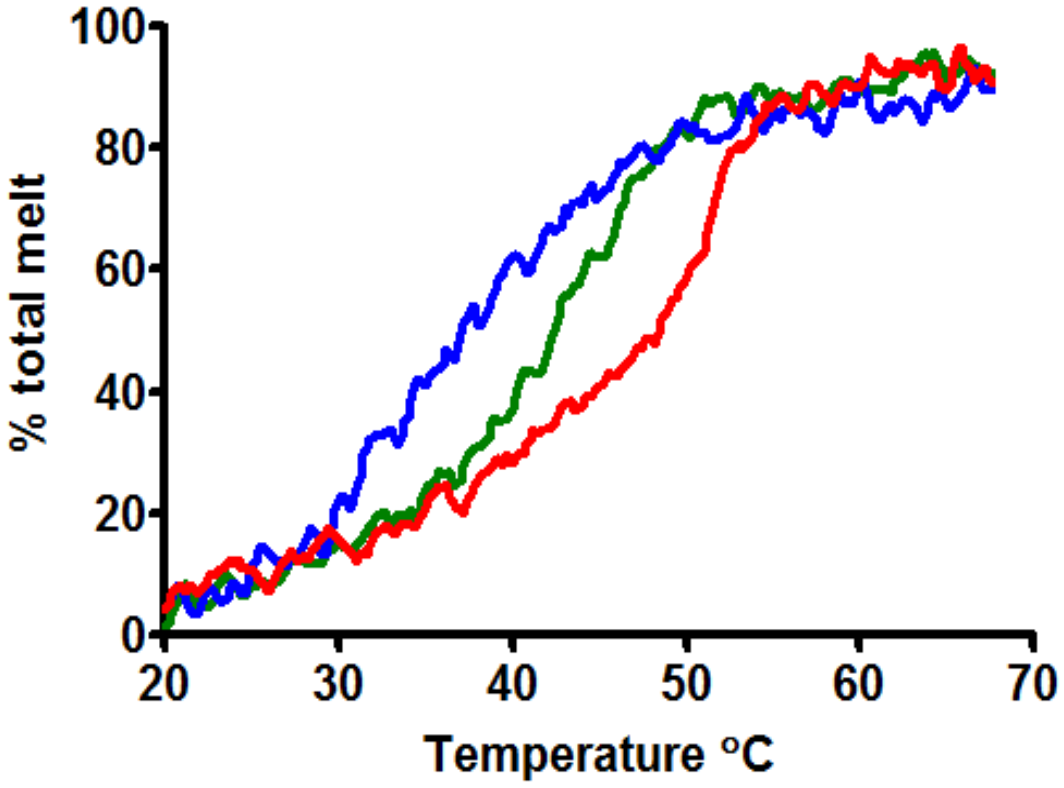

Figure 2-8 Representative melting curves for HLNO, the HLNO triple mutant, and MBP-HLNO as measured by circular dichroism. The melting temperature (T_m) of the HLNO triple mutant was 42.5°C, 5°C greater than that of wild type OH-NicOX (37.5°C). More significantly, the T_m for MBP-HLNO (48.5°C) was 11 degrees higher than for the wild type OH-NicOX.

2.9.1 Figure 2-8 methods.

Circular dichroism temperature melt experiments were performed in 10 mM sodium phosphate buffer, pH 7.4 containing 0.1 mg/mL of protein. Data were recorded with a resolution of 0.2 ^{o}C and ΔT of 1.5 ^{o}C per minute. Molar ellipticity values were recorded at 222 nm using a Jasco 810 spectrometer and measuring the change as a function of temperature. Representative curves are shown for the three constructs: wild type HLNO (Blue), HLNO-triple mutant (Green) and MBP-HLNO (Red).

2.10 Bibliography / References

1. Hochstein, L. I.; Rittenberg, S. C., The bacterial oxidation of nicotine. I. Nicotine oxidation by cell-free preparations. *J Biol Chem* **1959,** *234* (1), 151-5.

2. Hochstein, L. I.; Rittenberg, S. C., The Bacterial Oxidation of Nicotine. *Journal of Biological Chemistry* **1959,** *234* (1), 156-160.

3. Hochstein, L. I.; Rittenberg, S. C., The Bacterial Oxidation of Nicotine. *Journal of Biological Chemistry* **1960,** *235* (3), 795-799.

4. Decker, K.; Bleeg, H., Induction and purification of stereospecific nicotine oxidizing enzymes from Arthrobacter oxidans. *Biochim Biophys Acta* **1965,** *105* (2), 313-24.

5. Decker, K.; Dai, V. D., Mechanism and Specificity of l- and d-6-Hydroxynicotine Oxidase. *European Journal of Biochemistry* **1967,** *3* (2), 132-138.

6. Dai, V. D.; Decker, K.; Sund, H., Purification and properties of L-6-hydroxynicotine oxidase. *Eur J Biochem* **1968,** *4* (1), 95-102.

7. Tang, H.; Wang, L.; Meng, X.; Ma, L.; Wang, S.; He, X.; Wu, G.; Xu, P., Novel nicotine oxidoreductase-encoding gene involved in nicotine degradation by Pseudomonas putida strain S16. *Appl Environ Microbiol* **2009,** *75* (3), 772-8.

8. Tang, H.; Wang, L.; Wang, W.; Yu, H.; Zhang, K.; Yao, Y.; Xu, P., Systematic unraveling of the unsolved pathway of nicotine degradation in Pseudomonas. *PLoS Genet* **2013,** *9* (10), e1003923.

9. Gurusamy, R.; Natarajan, S., Current status on biochemistry and molecular biology of microbial degradation of nicotine. *ScientificWorldJournal* **2013,** *2013*, 125385.

10. Fitzpatrick, P. F., The enzymes of microbial nicotine metabolism. *Beilstein J Org Chem* **2018,** *14*, 2295-2307.

11. Tararina, M. A.; Xue, S.; Smith, L. C.; Muellers, S. N.; Miranda, P. O.; Janda, K. D.; Allen, K. N., Crystallography Coupled with Kinetic Analysis Provides Mechanistic Underpinnings of a Nicotine-Degrading Enzyme. *Biochemistry* **2018,** *57* (26), 3741-3751.

12. Tararina, M. A.; Janda, K. D.; Allen, K. N., Structural Analysis Provides Mechanistic Insight into Nicotine Oxidoreductase fromPseudomonas putida. *Biochemistry* **2016,** *55* (48), 6595-6598.

13. Qiu, J.; Ma, Y.; Zhang, J.; Wen, Y.; Liu, W., Cloning of a novel nicotine oxidase gene from Pseudomonas sp. strain HZN6 whose product nonenantioselectively degrades nicotine to pseudooxynicotine. *Appl Environ Microbiol* **2013,** *79* (7), 2164-71.

14. Kachalova, G. S.; Bourenkov, G. P.; Mengesdorf, T.; Schenk, S.; Maun, H. R.; Burghammer, M.; Riekel, C.; Decker, K.; Bartunik, H. D., Crystal structure analysis of free and substrate-bound 6-hydroxy-L-nicotine oxidase from Arthrobacter nicotinovorans. *J Mol Biol* **2010,** *396* (3), 785-99.

15. Fitzpatrick, P. F.; Chadegani, F.; Zhang, S.; Roberts, K. M.; Hinck, C. S., Mechanism of the Flavoprotein L-Hydroxynicotine Oxidase: Kinetic Mechanism, Substrate Specificity, Reaction Product, and Roles of Active-Site Residues. *Biochemistry* **2016,** *55* (4), 697-703.

16. Hill, E. B.; Wayne, L. G.; Gross, W. M., Purification of mycobacterial deoxyribonucleic acid. *J Bacteriol* **1972,** *112* (3), 1033-9.

17. Qin, H.; Hu, J.; Hua, Y.; Challa, S. V.; Cross, T. A.; Gao, F. P., Construction of a series of vectors for high throughput cloning and expression screening of membrane proteins from Mycobacterium tuberculosis. *BMC Biotechnol* **2008,** *8*, 51.

18. Tucker, W. C.; Du, Z.; Hein, R.; Gromet-Elhanan, Z.; Richter, M. L., Role of the ATP synthase alpha-subunit in conferring sensitivity to tentoxin. *Biochemistry* **2001,** *40* (25), 7542-8.

19. Bradford, M. M., A rapid and sensitive method for the quantitation of microgram quantities of protein utilizing the principle of protein-dye binding. *Anal Biochem* **1976,** *72*, 248-54.

20. Mishin, V.; Gray, J. P.; Heck, D. E.; Laskin, D. L.; Laskin, J. D., Application of the Amplex red/horseradish peroxidase assay to measure hydrogen peroxide generation by recombinant microsomal enzymes. *Free Radic. Biol. Med.* **2010,** *48* (11), 1485-1491.

21. Müller, F., *Chemistry and biochemistry of flavoenzymes*. CRC Press: Boca Raton, 1991; p v. <1-3 >.

22. Morris, G. M.; Goodsell, D. S.; Huey, R.; Olson, A. J., Distributed automated docking of flexible ligands to proteins: parallel applications of AutoDock 2.4. *J Comput Aided Mol Des* **1996,** *10* (4), 293-304.

23. Morris, G. M.; Huey, R.; Olson, A. J., Using AutoDock for ligand-receptor docking. *Curr Protoc Bioinformatics* **2008,** *Chapter 8*, Unit 8 14.

24. Capriotti, E.; Fariselli, P.; Casadio, R., I-Mutant2.0: predicting stability changes upon mutation from the protein sequence or structure. *Nucleic Acids Res* **2005,** *33* (Web Server issue), W306-10.

25. Xue, S.; Schlosburg, J. E.; Janda, K. D., A New Strategy for Smoking Cessation: Characterization of a Bacterial Enzyme for the Degradation of Nicotine. *J Am Chem Soc* **2015,** *137* (32), 10136-9.

26. Benowitz, N. L., Clinical pharmacology of inhaled drugs of abuse: implications in understanding nicotine dependence. *NIDA Res Monogr* **1990,** *99*, 12-29.

27. Benowitz, N. L.; Swan, G. E.; Jacob, P., 3rd; Lessov-Schlaggar, C. N.; Tyndale, R. F., CYP2A6 genotype and the metabolism and disposition kinetics of nicotine. *Clin Pharmacol Ther* **2006,** *80* (5), 457-67.

28. Xue, S.; Kallupi, M.; Zhou, B.; Smith, L. C.; Miranda, P. O.; George, O.; Janda, K. D., An enzymatic advance in nicotine cessation therapy. *Chem Commun (Camb)* **2018,** *54* (14), 1686-1689.

29. Ray, R.; Tyndale, R. F.; Lerman, C., Nicotine dependence pharmacogenetics: role of genetic variation in nicotine-metabolizing enzymes. *J Neurogenet* **2009,** *23* (3), 252-61.

30. Thisted, T.; Biesova, Z.; Walmacq, C.; Stone, E.; Rodnick-Smith, M.; Ahmed, S. S.; Horrigan, S. K.; Van Engelen, B.; Reed, C.; Kalnik, M. W., Optimization of a nicotine degrading enzyme for potential use in treatment of nicotine addiction. *BMC Biotechnology* **2019,** *19* (1).

31. Xue, S.; Schlosburg, J. E.; Janda, K. D., A New Strategy for Smoking Cessation: Characterization of a Bacterial Enzyme for the Degradation of Nicotine. *Journal of the American Chemical Society* **2015,** *137* (32), 10136-10139.

32. Fitzpatrick, P. F.; Chadegani, F.; Zhang, S.; Dougherty, V., Mechanism of Flavoprotein l-6-Hydroxynicotine Oxidase: pH and Solvent Isotope Effects and Identification of Key Active Site Residues. *Biochemistry* **2017,** *56* (6), 869-875.

33. Wilson, G. S.; Gifford, R., Biosensors for real-time in vivo measurements. *Biosens Bioelectron* **2005,** *20* (12), 2388-403.

34. Wilson, G. S.; Johnson, M. A., In-Vivo Electrochemistry: What Can We Learn about Living Systems? *Chemical Reviews* **2008,** *108* (7), 2462-2481.

35. Naylor, E.; Aillon, D.; Barett, B.; Gabbert, S.; Harmon, H.; Turek, F.; Wilson, G.; Johnson, D.; Petillo, P., *LACTATE ACTS AS A PRIMARY ENERGY SOURCE FOR NEURONAL ACTIVITY DURING WAKING AND REM SLEEP*. 2011; p A41-A41.

36. Lambrianou, A.; Demin, S.; Hall, E. A. H., Protein Engineering and Electrochemical Biosensors. Springer Berlin Heidelberg: pp 65-96.

37. Naylor, E.; Aillon, D. V.; Gabbert, S.; Harmon, H.; Johnson, D. A.; Wilson, G. S.; Petillo, P. A., Simultaneous real-time measurement of EEG/EMG and L-glutamate in mice: A biosensor study of neuronal activity during sleep. *J Electroanal Chem (Lausanne)* **2011,** *656* (1-2), 106-113.

38. Benowitz, N. L.; Hukkanen, J.; Jacob, P., 3rd, Nicotine chemistry, metabolism, kinetics and biomarkers. *Handb Exp Pharmacol* **2009,** (192), 29-60.

39. Qiu, J.; Wei, Y.; Ma, Y.; Wen, R.; Wen, Y.; Liu, W., A novel (S)-6-hydroxynicotine oxidase gene from Shinella sp. strain HZN7. *Appl Environ Microbiol* **2014,** *80* (18), 5552-60.

40. Bach, H.; Mazor, Y.; Shaky, S.; Shoham-Lev, A.; Berdichevsky, Y.; Gutnick, D. L.; Benhar, I., Escherichia coli maltose-binding protein as a molecular chaperone for recombinant intracellular cytoplasmic single-chain antibodies 1 1Edited by R. Huber. *Journal of Molecular Biology* **2001,** *312* (1), 79-93.

41. Raran-Kurussi, S.; Waugh, D. S., Unrelated solubility-enhancing fusion partners MBP and NusA utilize a similar mode of action. *Biotechnol Bioeng* **2014,** *111* (12), 2407-11.

42. Vallon, O., New sequence motifs in flavoproteins: evidence for common ancestry and tools to predict structure. *Proteins* **2000,** *38* (1), 95-114.

43. Kopacz, M. M.; Rovida, S.; van Duijn, E.; Fraaije, M. W.; Mattevi, A., Structure-based redesign of cofactor binding in putrescine oxidase. *Biochemistry* **2011,** *50* (19), 4209-17.

3 Self-Immobilized Putrescine Oxidase Biocatalyst System Engineered with a Metal Binding Peptide

3.1 Authorship and Publication Information

This work was published on 12th September 2020 in the journal ACS *Langmuir* under the following title and authorship series and is reproduced here with minor formatting revisions. It is a work contributed to by all listed authors. In this work, I prepared recombinant DNA expression vectors for the production of *wt-PutOx* and *PutOx-AuBP* proteins, expressed and purified *wt-PutOx* and *PutOx-AuBP* proteins out of *E. coli*, carried out the nanoparticle binding experiments described in the methods and results sections, carried out the QCMD binding experiments described in the methods and results sections, assisted in the final interpretation of data, and contributed to the editorial preparation of the final document.

Reproduced with permission from ACS Langmuir 2020 36 (40), 11908-11917

DOI:10.1021/acs.langmuir.0c01986,

Self-Immobilized Putrescine Oxidase Biocatalyst System Engineered with a Metal Binding Peptide

*Nilan J. B. Kamathewatta[‡a], Dwight O. Deay III[‡b], Banu Taktak Karaca[cd], Steve Seibold[b], Tyler M. Nguyen[a], Brandon Tomás[cf], Mark L. Richter[a], Cindy L. Berrie[*a,c], and Candan Tamerler**

[a]Department of Chemistry; University of Kansas, Lawrence, KS 66045, USA
[b]Department of Molecular Biosciences; University of Kansas, Lawrence, KS 66045, USA
[c]Institute for Bioengineering Research, University of Kansas, Lawrence, KS 66045, USA
[d]Department of Molecular Biology and Genetics, Biruni University, Istanbul, Turkey, 34010
[e]Bioengineering Program, University of Kansas, Lawrence, KS 66045, USA
[f]Department of Mechanical Engineering, University of Kansas, Lawrence, KS 66045, USA

‡N.J.B.K. and D.O.D. equally contributed, co-first authors.

3.2 Abstract

Flavin oxidases are valuable biocatalysts for the oxidative synthesis of a wide range of compounds, while at the same time reduce oxygen to hydrogen peroxide. Compared to other redox enzymes, their ability to use molecular oxygen as an electron acceptor offers a relatively simple system that does not require a dissociable coenzyme. As such, they are attractive targets for adaptation as cost-effective biosensor elements. Their functional immobilization on surfaces offers unique opportunities to expand their utilization for a wide range of applications. Genetically engineered peptides have been demonstrated as enablers of the functional assembly of biomolecules at solid material interfaces. Once identified as having a high affinity for the material of interest, these peptides can provide a single step bioassembly process with orientation control, acritical parameter for functional immobilization of the enzymes. In this study, for the first time, we explored the bioassembly of a putrescine oxidase enzyme using a gold binding peptide tag. The enzyme was genetically engineered to incorporate a gold binding peptide with an expectation of an effective display of the peptide tag to interact with the gold surface. In this work, the functional activity and expression were investigated, along with the selectivity of the binding of the peptide-tagged enzyme. The fusion enzyme was characterized using multiple techniques, including protein electrophoresis, enzyme activity, and microscopy and spectroscopic methods, to verify the functional expression of the tagged protein with near-native activity. Binding studies using quartz crystal microbalance (QCM), nanoparticle binding studies, and atomic force microscopy studies were used to address the selectivity of the binding through the peptide tag. Surface binding AFM studies show that the binding was selective for gold.

Quartz crystal microbalance studies show a strong increase in the affinity of the peptide-tagged protein over the native enzyme, while activity assays of protein bound to nanoparticles provide evidence that the enzyme retained catalytic activity when immobilized. In addition to showing selectivity, AFM images show significant differences in the height of the molecules when immobilized through the peptide tag compared to immobilization of the native enzyme, indicating differences in orientation of the bound enzyme when attached via the affinity tag. Controlling the orientation of surface-immobilized enzymes would further improve their enzymatic activity and impact diverse applications, including oxidative biocatalysis, biosensors, biochips, and biofuel production.

3.3 Introduction

Nature has provided a versatile array of enzymes responsible for a wide variety of selective redox reactions. Oxidative enzymes have emerged as desirable for a range of applications due to their high degree of selectivity relative to other chemocatalysts.[1-3] This feature is highly valued by industry as the use of redox enzymes in organic synthesis can minimize by-product formation and circumvent the need for protection and deprotection steps.

Flavin-dependent oxidase enzymes in particular have been used extensively to generate compounds of interest to the pharmaceutical, chemical and agrochemical industries as well as for biosensing applications.[4-9] These enzymes contain a flavin adenine mononucleotide (FMN) or dinucleotide (FAD) which is tightly associated with the enzyme and, in some cases covalently bound.1 Flavoprotein oxidases can catalyze two-electron oxidations of a wide range of compounds such as amines and alcohols, use molecular oxygen as an electron acceptor to generate hydrogen peroxide. Their ability to rely on the reductive activation of molecular oxygen as an electron acceptor to regenerate the oxidized enzyme-bound flavin provides a simpler and

less expensive system compared to other redox enzymes that require a constant supply of a dissociable coenzyme (nicotine amide dinucleotide (phosphate)/reduced nicotine amide dinucleotide (NAD(P)H/NADH)). Flavin oxidases that produce hydrogen peroxide are especially useful as the recognition element for biosensors since the hydrogen peroxide product is electroactive.[2-6]

The best studied flavin oxidase is glucose oxidase which has been applied for many years in the textile industry and for diagnostic applications.[7-9] Glucose oxidase catalyzes sugar oxidation coupled to the reduction of FAD to $FADH_2$ and to hydrogen peroxide production. Another flavin-containing enzyme is putrescine oxidase (PutOx, E.C 1.4.3.10) which is capable of degrading polyamines. PutOx is a homodimeric protein and unique among flavin-containing enzymes since the isolated enzyme appears to include only one non-covalently bound FAD per dimeric protein.[10-12] Recently, PutOx has been utilized as a diagnostic tool for the detection of biogenic amines such as putrescine and cadaverine[13-17] in body fluids as increased levels of these biogenic amines reflect tumor growth rates and thus can be used as tumor biomarkers.[18, 19] PutOx is also used to monitor food freshness by detecting polyamines in spoiling food.[14, 20] The physiological and toxicological effects of several biogenic amines have been reported in a wide range of food products and are a potential public health concern. These include, but are not limited to, putrescine, histamine, cadaverine, spermine and agmatine. The consumption of foods containing high levels of biogenic amines has been associated with poisoning cases and health hazards; biogenic amines formed in food can cause serious allergic reactions that may lead to difficulty in breathing, itching, rash, vomiting, fever, and hypertension.[21, 22] Consequently, there has been an increasing effort in developing sensors that allow monitoring of these compounds and relate the outcomes to the freshness of food products.[23] For instance, Inaba *et al* have

developed an electrochemical biosensor based on two oxygen electrodes utilizing a combination of putrescine oxidase and agmatinase to determine squid freshness.[14] Boka *et al* also developed a biosensor based on an enzyme modified carbon electrode for rapid determination of putrescine in food products with a detection limit of 0.01-0.25 mM.[13] Different immobilization techniques have been employed for putrescine biosensors. Enzyme electrodes were constructed by covalently binding the enzyme onto modified carbon or platinum surfaces by crosslinking with glutaraldehyde.[13, 17, 18] Recently many efforts have been made to fabricate biosensors based on direct electron transfer between the catalytic site of enzyme and the electrode. This phenomenon is highly difficult in the case of PutOx, since the FAD co-factor is deeply embedded within the protein.[10, 11] It is, however, feasible to create electron bridges between a conductive surface and a redox component within the enzyme, and this strategy is being actively pursued but again requires control over the surface orientation of the protein.

Immobilization of enzymes often results in reduction in stability and activity of the surface bound enzymes. Control over the orientation and the molecular level interactions at the solid support interfaces are the major contributors to such activity reductions. Biological systems typically integrate multicomponent self-assembly for complex tasks requiring precise function of many components working in tandem. There has been a growing interest in harnessing self-assembly in controlling molecular level interactions between enzymes and the surfaces. Yet, functional assembly of multicomponent systems at the nanoscale remains a significant challenge.[24-30] Incorporation of biomolecules into solid supports requires two critical considerations: 1) maintenance of functional integrity of the biomolecule when surface-immobilized, and 2) precise placement and orientation of the biomolecule in a manner that allows control over its interaction, not only with the interface directly but also with other

components in the assembly.[31, 32] These factors are essential for designing functional, complex, nanostructured materials and devices that involve proteins such as microarrays, biosensors, and biochips.[29, 30, 32]

Self-assembled monolayers (SAM) that can be patterned using lithographic methods have been used extensively to create surface arrays of proteins for proteomic or biosensing applications.[33-38] Linkers that are most often used to immobilize proteins are silanes and thiols that bind at one end to the inorganic materials surface via silanol or thiol moieties and have a functional group at the other end (*e.g.* amine, carboxyl) for protein binding.[39-41] Although widely used, these linkers have a number of disadvantages including instability, lack of material selectivity or multilayer coverage. More importantly, attachment to surface groups on the protein is dependent on the availability and location of those groups. It is, therefore, difficult to control the orientation of the protein on the surface, which is often heterogeneous due to the attachment of the linker to one or more different groups on the surface of the protein. The variation due to such heterogeneous binding can result in a mixture of active, inactive, or partially active proteins on the surface.[25]

The use of surface-recognition peptides as an alternative to chemical coupling methods as surface specific bio-linkers is gaining considerable traction.[42, 43] The peptides are selected from combinatorial peptide phage or cell surface display libraries. The peptide-mediated surface functionalization provides much greater control over the assembly process in a self-directed manner, removing the uncertainty of orientation that accompanies a random attachment approach where binding can occur through multiple sites on the protein. The dissociation constant values for surface-recognition peptides vary within the nM to mM range[44-46] and can be tuned for selective material binding over a wide range of surfaces.[47] The properties of these peptides have been critically examined in studies of surface functionalization, self-assembly, and formation of

various nanostructures.[34, 35] They were also demonstrated to be efficient surface linkers as fusion partners to other biomolecules.[48-50]

In the present work, we designed a self-immobilized biocatalyst system by focusing on a recently discovered putrescine oxidase from actinomycete *Rhodococcus erthropolis.* The enzyme ($PutOx_{Rh}$) displays a low level of sequence identity to other family members, but the structure of the flavin-binding region is highly conserved. $PutOx_{Rh}$ exhibits a high catalytic activity and high specificity toward putrescine as substrate ($k_{cat}/K_M = 3.2\times10^6$).[10] The enzyme is a homodimer with a molecular mass of ~100 kDa.[11] Flavin oxidases have been used in a variety of biosensing applications [13-15, 51-53] and the putrescine oxidase has been selected here as a model redox active enzyme for surface immobilization studies.[10, 13, 15] The most promising way to achieve direct electron transfer to a metal surface can be fusion of $PutOx_{Rh}$ enzyme with inorganic binding peptide, which is highly specific for several types of metal surfaces either flat or with structured nanoscale topography.[51, 54-58] In our prior work, we have demonstrated that the gold binding peptide alone binds to gold surfaces with high selectivity and affinity.[42, 43] Building upon this prior work,[42, 43] we have engineered a fusion protein consisting of the $PutOx_{Rh}$ and a C-terminal gold binding peptide (AuBP). We have chosen a novel putrescine oxidase identified from the genome of *Rhodococcus erythropolis*.[12] In this work, we have studied its assembly onto a both gold nanoparticles and flat Au(111) surfaces. The self-assembled PutOx-AuBP binds onto the gold surface with a significantly higher affinity than the native PutOx enzyme lacking the AuBP. We have also demonstrated that the immobilized enzyme remained functionally active when bound to the surface of gold nanoparticles. A detailed investigation of the enzyme binding using atomic force microscopy demonstrated that the protein shape and orientation at the surface are significantly altered on the gold surface upon the incorporation of the AuBP. The use of PutOx

engineered with a peptide tag offers a precise assembly while securing the enzyme function in a single step and can be adapted easily as a promising strategy for designing immobilized enzyme biocatalysts in multicomponent systems.

3.4 Experimental Methods

3.4.1 Materials DNA ligase and Dpn1 were purchased from Thermo Fisher Scientific. *E.coli* XL-10 Gold and BL21 (DE3) competent cells were purchased from Agilent Technologies. TEV was prepared as previously described.[59] NuPAGE gel, 12% Bis-Tris, Life Technologies, stained with InstantBlue from Expedeon. Gold-citrate nanoparticles were obtained Nanopartz™. All other reagents were of the highest grade available. Standard pH 8.0 phosphate buffer was obtained from Fisher scientific (10 mM Potassium phosphate monobasic/sodium hydroxide). Ruby muscovite mica was purchased from Lawrence Mica Company (New York). It was freshly cleaved before use. Milli-Q water (resistivity> 18.2 MΩ-cm) was used to rinse surfaces before and after protein incubation.

Template stripped gold surfaces were prepared by thermal evaporation of gold (Alfa Aesar, 99.999%) on mica at a rate of ~1-3 Å/sec in an Edwards Auto 306 thermal evaporator while heating to a temperature of ~200℃ with a quartz lamp. Template stripping was carried out as described previously.[60-62] Briefly, the samples were glued to a clean glass surface using Epo-Tek 377 epoxy (Epoxy Technology) and cured at 80℃ for 16 to 24 hours (h). The pieces were mechanically cleaved at the gold/mica interface immediately prior to use to expose a flat Au (111) surface with relatively large grains.

3.4.2 Expression Vector Construction Construction of expression vectors for the production of PutOx-AuBP was performed using whole plasmid PCR mutagenesis on the pTBMalE plasmid[63] encoding the putrescine oxidase (PutOx) gene from *Rhodococcus erythropolis* together with His6-Maltose-Binding Protein (His6-MBP). Mutagenic PCR primers targeted to either the N or C terminus of the PutOx gene were produced with 5' overhangs each encoding half of the cyclic AuBP peptide (cpgWALRRSIRRQSYgpc) plus linker (PGGG) sequence.[12, 42, 44, 50] For the production of the N terminal construct, primer annealing sites were chosen to delete the MBP, and TEV cut site coding regions thereby generating an ORF coding for PutOx-AuBP. The annealing site of primers for C terminal insertion was selected to leave these sequences intact with the intention of removing them by TEV protease cleavage after expression. The primers used are shown in Table S1. Primers were phosphorylated on their 5' termini with polynucleotide kinase prior to PCR. PCR products were purified using a Qiagen PCR cleanup kit, ligated with DNA ligase, digested with Dpn1 and transformed into 50 μL of XL-10 Gold cells. Transformants were selected on 100 μg/mL ampicillin LB agar plates. DNA from transformant colonies was purified using a Qiagen miniprep kit, sequenced and transformed into BL21 (DE3) pRARE cells for expression. BL21 (DE3) pRARE cells were also transformed with the unmutated pTBMalE-PutOX expression vector for side by side production of the wild type enzyme.

3.4.3 Protein Expression and Purification Transformant starter cultures of BL21 DE3 pRARE were grown in 25 mL Luria Bertani (LB) broth containing 200 μg/mL carbenicillin at 30ºC overnight. Large scale protein expression was performed the next day at 20ºC in 1 L of enhanced LB medium (200 □g/mL carbenicillin, 50 g low salt LB mix, 10 mM $MgCl_2$, 0.8 % (V/V) glycerol, 89 mM sodium phosphate, pH 7.4). Cells were grown to an OD_{600} of 0.6 at 350 rpm shaking speed before the addition of 100 μM Isopropyl-B-D-1-thiogalactopyranoside (IPTG) and 0.5 % (V/V) glycerol. Expression was allowed to continue for 24 hours before cells were chilled to 4ºC and harvested by centrifugation at 2744 rcf for 10 min. Cell pellets were resuspended in 100 mL lysis buffer (50 mM Tris-HCl, pH 8.0, 300 mM NaCl, 10 mM imidazole) and frozen overnight at -80ºC. Cell suspensions were thawed and sonicated in an ice water bath using a Branson model 400 sonifier (2 sec on, 10 s off at 30% amplitude for 10 min). The lysate was clarified by centrifugation at 20,000 rcf for 1 hour. The soluble fraction was gently mixed with 5 mL of Qiagen Superflow Ni-NTA resin equilibrated with lysis buffer. The resin slurry was loaded onto a 1.6 cm x 30 cm (biorad) column and washed with 20 column volumes of lysis buffer followed by 20 column volumes of lysis buffer containing 20 mM imidazole. The protein was eluted with 1.5 column volumes of lysis buffer containing 250 mM imidazole-HCl.

The eluate from the Ni-NTA column was subjected to gel filtration on Sephadex G50 equilibrated with TEV protease buffer (10 mM Tris-HCl, pH 7.5, 100 mM NaCl, 100 □M EDTA, and 2 mM DTT). The TEV protease was added to a 1:20 (TEV: protein) molar ratio. The cleavage reactions were sterile filtered, and cleavage was allowed to proceed for 48 hours at 25ºC. Following gel filtration on Sephadex G50 equilibrated with TBS (20 mM Tris-HCl, pH 7.5, 140 mM NaCl), the protein was applied to a Ni-NTA column. The tag-less protein that was collected in the flow-through was >99% pure as judged by SDS-PAGE (Figure 1). The protein

was concentrated to ~40 mg/mL by ultrafiltration (Amicon Ultra-15 concentrator) and loaded onto a 1.6 × 60 cm Superdex PG200 column at a flow rate of 1.25 mL/min. Peak fractions containing the PutOx-AuBP or PutOx dimer were pooled, glycerol added to 20% (v/v), and the sample flash frozen in liquid nitrogen and stored at -80^{o}C.

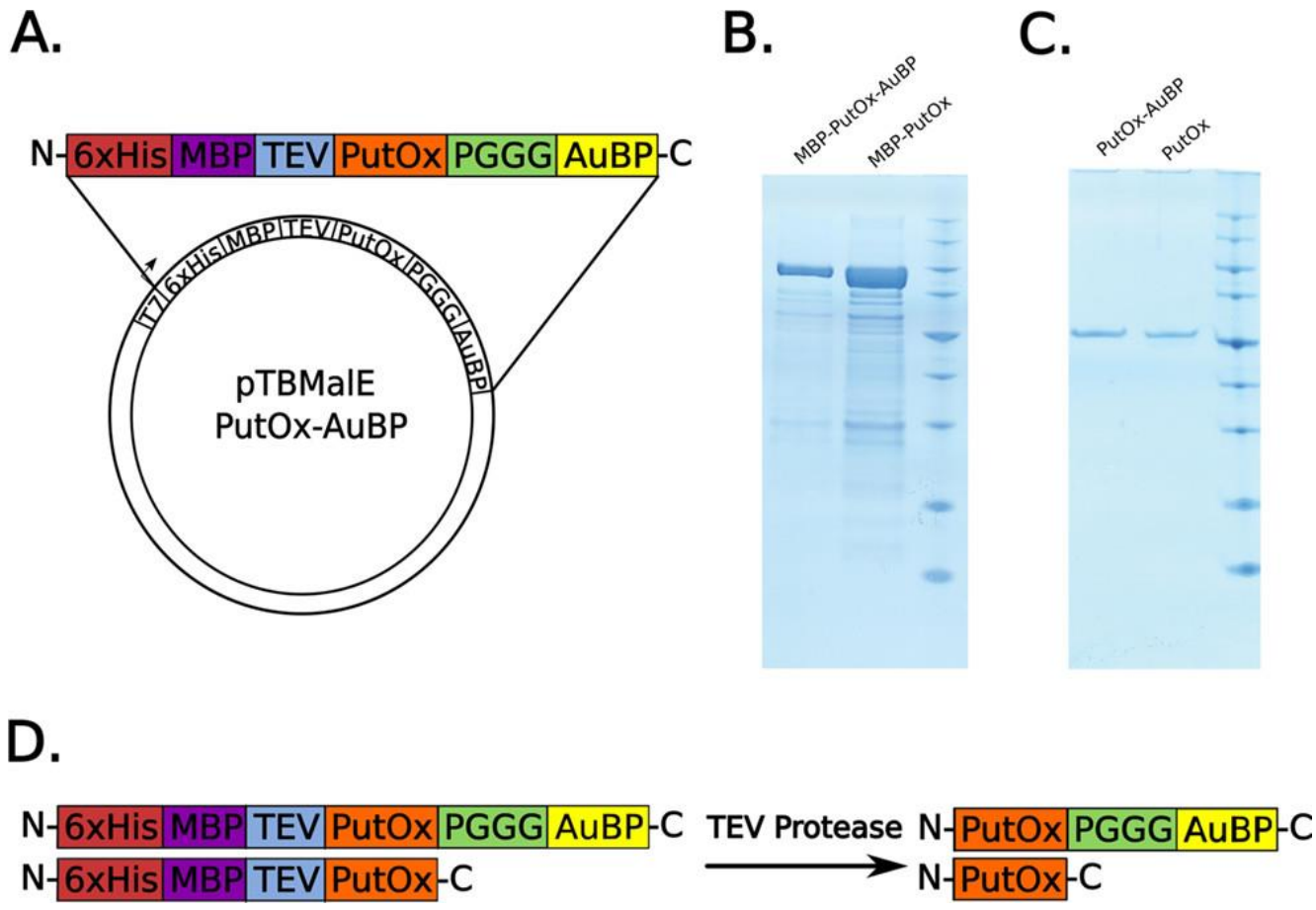

Figure 3-1 Expression vector overview and SDS-PAGE of expressed proteins

3.4.4 Enzyme Activity Measurements The putrescine oxidase activity was measured using a horseradish peroxidase (HRP)-coupled assay containing 2,2'-azino-bis (3-ethylbenzthiazoline-6-sulphonic acid) (ABTS) at 25ºC .[12] The hydrogen peroxide formed by PutOx is the primary substrate of HRP which couples the reduction of peroxide to the oxidation of ABTS, yielding a green chromogen that can be measured at 420 nm (ε_{420}=36000 μM^{-1} cm^{-1}). The standard assay mixture with HRP-ABTS consisted of 40 μM putrescine, 50 mM Tris HCl buffer at pH 8.0, 100 μM ABTS, 5 U HRP and 10 μl of the enzyme dilution sample. To determine the kinetic parameters, PutOx and/or PutOx-AuBP activities were measured at different putrescine concentrations (1 μM-40 μM) at 25ºC using HRP-ABTS enzyme assay through following the hydrogen peroxide formation by Cytation3 multimode spectrophotometer (Biotek, Vermont, USA). Data were then fitted with GraphPadPrism using the Michaelis-Menten equation for enzyme kinetics (Supporting Information, Fig. S1). Data were reproduced three times and all assays were performed in triplicates. The enzyme concentration was determined with the standard Bradford assay using bovine serum albumin (BSA) standards at 595 nm wavelength.

3.4.5 Gold Nanoparticle Binding Assay The activity of the PutOx and PutOx-AuBP bound to gold nanoparticles was analyzed by The activity of the PutOx and PutOx-AuBP bound to gold nanoparticles was analyzed by Amplex Red/Horseradish Peroxidase (HRP) assay after multiple washing steps to assess the robustness of the binding and activity. Efficient washing of nanoparticles was accomplished by repeatedly collecting the particles by centrifugal sedimentation followed by withdrawal of a defined volume of the particle free supernatant and then resuspending the nanoparticle pellet in an equal volume of fresh buffer. Specifically, citrate capped gold nanoparticles were concentrated to 5 mg/mL by centrifugation at 200 x g for 48 h and resuspended in 100 μL H_2O. Aliquots of 25 μL of PutOx and PutOx-AuBP with a concentration of 10 mg/mL (100 μM) in 200 μM sodium phosphate buffer, pH 7.4, were combined with 25 μL of the concentrated nanoparticles and allowed to incubate at room temperature overnight with gentle mixing by inversion to prevent aggregation. Samples were then diluted with 900 μL of the sodium phosphate buffer and pelleted by centrifugation at 200 rcf for 48 h. A volume of 900 μL of the supernatant was carefully removed with a pipette and the pellet was resuspended in 50-100 μL of residual buffer. The protein/nanoparticle suspension was assayed for volume specific putrescine oxidation activity using the Amplex Red/Horseradish Peroxidase (HRP) assay method using 200 μM putrescine-HCl as the substrate. After resuspension and HRP activity assay (~20 min), 900 μL of phosphate washing buffer was added to the suspension and the particles were again collected by centrifugation. This cycle of washing the particles followed by volumetric specific activity determination was repeated 8 times.

3.4.6 Quartz Crystal Microbalance Determination of Binding Constants PutOx and PutOx-AuBP stock solutions were prepared for QCM-D analysis by gel filtration into 140 mM NaCl, 10 mM sodium phosphate, pH 7.4, followed by centrifugation at 21,000 rcf for 10 min and filtration through a 0.1 μm filter (Millipore, UltraFree-MC, type VV). The concentrations of protein samples were adjusted with freshly degassed buffer and filtered through 0.2 μm Millipore filters. Amorphous gold QCM-D sensors (Q-sense) were rigorously cleaned, mounted in flow cells, and equilibrated with the same phosphate buffer for 2 hours. Only sensors achieving baseline stability (< 0.5 Hz/h drift) were used for data collection. Protein solutions were passed over the equilibrated sensors at 200 μL/min. For each concentration, side-by-side replicates were collected for both PutOx and PutOx-AuBP.

3.4.7 AFM Imaging of Protein on Gold and Mica To study the material specificity of the proteins, template stripped gold and mica surfaces were used as substrates for protein adsorption. The surfaces were cleaned with pH adjusted (pH = 8.0) doubly distilled water for 45 seconds and conditioned with pH 8.0 phosphate buffer (10 mM potassium phosphate monobasic/sodium hydroxide) for 45 seconds. The protein concentrations were adjusted to 0.1 μM with the phosphate buffer. A volume of 100 μL of each protein sample was applied to the template stripped gold surfaces and mica surfaces and allowed to incubate for 2 hours. The surfaces were then washed with pH 8.0 phosphate buffer for 45 seconds, washed under a stream of pH adjusted MilliQ water (pH=8.0) for 45 seconds and dried under a stream of nitrogen. The surfaces were imaged after drying under nitrogen via tapping mode AFM *(Digital Instruments, NanoScope IIIa)*. Diamond-like carbon coated tips (TAP300DLC, *f=300 kHz, k = 40 N/m)* were used for imaging in tapping mode. Typical scan rates were 1 Hz with a scan size of 1 μm x 1μm.

To determine the dimensions of single molecules, samples were prepared with low protein coverage. Protein solutions containing 0.01 μM PutOx-AuBP were allowed to adsorb for 15 min on template stripped gold surfaces followed by rinsing with buffer and water as described above. To isolate the unlabelled PutOx molecules on template stripped gold surfaces, a 0.1 μM solution of protein was incubated on the surface for 2 hours. For mica samples, 0.1 μM solutions were used with 2 hours of incubation. (The higher protein concentration and longer incumbation times in these cases are due to the lower affinity, resulting in a smaller number of adsorbed molecules.) To measure the dimensions of individual molecules Bruker-NanoScope analysis 1.5 software was used, and from each sample, 50 molecules were analyzed over three different spots of the sample (n=50 for each protein). The average length and the width were measured as the full width at half maximum (FWHM) and the average height was measured with respect to the flat surface.

3.5 Results and Discussion

3.5.1 Fusion Protein Constructs The previously characterized gold binding peptide AuBP2[50] was chosen for this study due to its demonstrated high specificity and high affinity for binding to gold surfaces. The peptide was cyclized by incorporating flanking cysteinyl residues together with a short linker sequence attaching the peptide to the C-terminus of the protein. The oxidase partner for this construct, putrescine oxidase (PutOx), was chosen because it could be readily produced in a soluble, recombinant form when a maltose binding protein (MBP) solubility tag was incorporated into the N-terminus, plus a high resolution structure of the enzyme is available for computational analysis of constructs.[11] Preliminary experiments also indicated that PutOx retains >95% of its bound FAD upon purification following over-expression. Fusion proteins were engineered into the pTBMalE-4 vector such that they contained the AuBP on either the N- or the C-terminal end of the MBP-PutOx. When placed on the N-terminus of MBP-PutOx, attempts to recover the fusion protein from the soluble fraction, either by DEAE-cellulose or ammonium sulfate precipitation, resulted in irreversible aggregation of the protein. The N-terminally labeled construct was therefore abandoned. In contrast, when the AuBP was placed on the C-terminus of MBP-PutOx (see Fig. 1A) the fusion protein remained soluble during purification (see Fig. 1B) and retained 100% of its catalytic function when compared to the wild type enzyme (Fig. S1). A sequence coding for the TEV (tobacco etch virus) protease was introduced either 3′ (for N-terminal insertion) or 5’ (for C-terminal insertion) to the poly-linker insertion sites. This allowed the 6HisMBP tag to be cleaved from the protein following purification (see Fig. 1C and 1D). Several characterization methods were subsequently employed to examine the contribution of the AuBP to selective interaction with gold surfaces.

3.5.2 Enzymatic Activities of Fusion Protein After the successful expression and purification of the engineered enzyme, PutOx-AuBP, the catalytic activity was tested. First the PutOx-AuBP's activity was first analyzed to elucidate its retention of catalytic activity following the insertion of the new gold binding domain, AuBP. The calculated kinetic parameters are provided in Table 1. The k_{cat}/K_m ratio, where k_{cat} is the catalytic constant for conversion of substrate into product, and K_m (Michaelis-Menten constant), which provides an estimation of the affinity of enzyme to its substrate and is defined as the substrate concentration at which initial rates are half of the maximum velocity has been widely used for enzyme efficiency. The k_{cat} value obtained for the PutOx-AuBP (25.5±0.8 s^{-1}) was determined to be comparable to that of wild type PutOx (26.4±0.5 s^{-1}), which indicates that the enzymatic conversion of putrescine is similar for both enzymes and the AuBP tag insertion did not influence the enzymatic activity. Similarly, the substrate affinities (K_m) of PutOx-AuBP and PutOx for putrescine were calculated to be comparable. The catalytic efficiency of the PutOx-AuBP was determined to be 92.7% of the wild type PutOx. Attained catalytic efficiency demonstrates the engineered PutOx-AuBP enzyme can be adapted as a robust self-assembling biocatalysis system.

Table 3-1 Steady-State Kinetic Parameters for Putrescine of PutOx and PutOx-AuBP at pH 8.0

	K_M (μM)	k_{cat} (s^{-1})	k_{cat}/K_M ($s^{-1}mM^{-1}$)
PutOx[12]	8.2±0.5	26.4±0.5	3200
PutOx-AuBP	8.6±0.7	25.5±0.8	2965

3.5.3 PutOx-AuBP Attachment to Gold Nanoparticles The enzyme (PutOx-AuBP or PutOx) was incubated for 2 hours with 15 nm diameter citrate-coated gold nanoparticles and then subjected to multiple centrifugal washes with phosphate buffer. In this assay, nanoparticles are oversaturated with the proteins samples and the washing step removes free enzyme from solution, weakly bound protein, and reduces multi-layer formation of the enzyme over the nanoparticle surfaces (Fig. 2). The PutOx-AuBP is expected to replace the citrate on the particle surface as it binds. During adsorption, the particles were subjected to mixing overnight to prevent particle aggregation and multiple centrifugal washes were needed to completely remove the bulk excess unbound and weakly bound enzyme. At the end of each wash, the catalytic activity of the particles was measured using the Amplex red assay that measures the H_2O_2 generated upon putrescine oxidation.[64, 65]The results indicated PutOx coated samples drastically continued to lose their activity starting from the 1st wash to complete loss of activity at the end of 8 washing cycles whereas PutOx-AuBP coated samples conserved more of their activity with steady levels of activity from the 3rd washing cycle until the end of the 8th cycle. The results indicate that AuBP peptide provided a tight binding to the engineered PutOx-AuBP biocatalysis system.

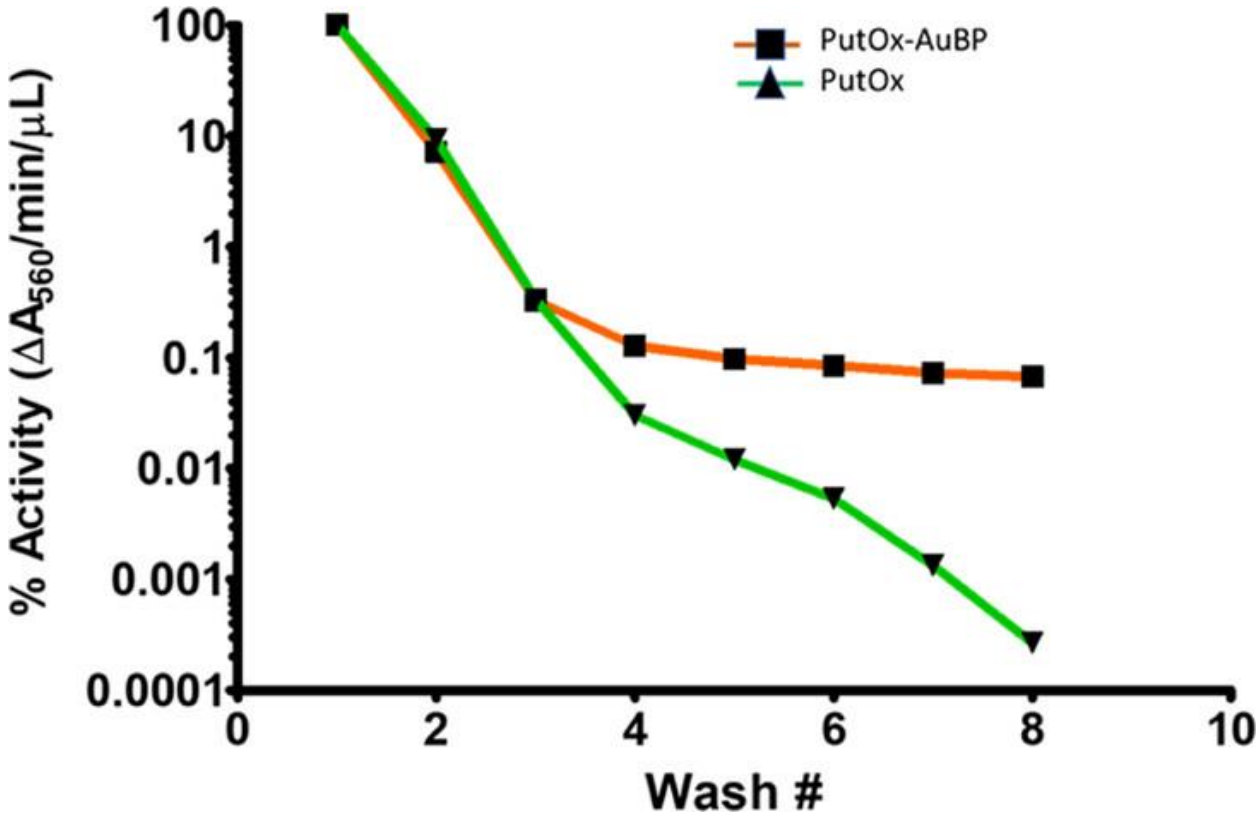

Figure 3-2 Nanoparticle binding experiment result Gold particles of 15 nm diameter were incubated with wild type putrescene oxidase or PutOx-AuBP followed by successive wash cycles. Putrescene oxidase activity decreases in both cases, but more activity is retained in the case of PutOx-AuBP. Activity is normalized to the initial activity of protein-bound particles.

3.5.4 QCM Binding Curves for the PutOx-AuBP Fusion Protein The interaction between both PutOx-AuBP and PutOx and the gold surface were investigated using a quartz crystal microbalance. Protein binding to the gold surface was measured in a small flow cell at a constant flow rate of 200 μL/min and the frequency was recorded as a function of time. Multiple binding curves were collected using solutions with different protein concentrations. Response curves are shown for two different concentrations (20 nM and 100 nM) of PutOx-AuBP compared to 100 nM PutOx lacking the gold binding tag (see Fig. 3A). Adsorption data were fit to a single exponential to obtain maximum equilibrium frequency shift (Δf) values over a range of concentrations (see Fig. 3B). Little if any desorption occurred following several hours of washing in the absence of enzyme, indicating very tight binding. Estimates of the dissociation constant for binding of PutOx-AuBP were obtained from a Langmuir fit of the kinetic data (20.2 ± 9.6 nM)66 as well as from a non-linear regression analysis (20.0 ± 7.1 nM) of the data shown in Figure 3B.

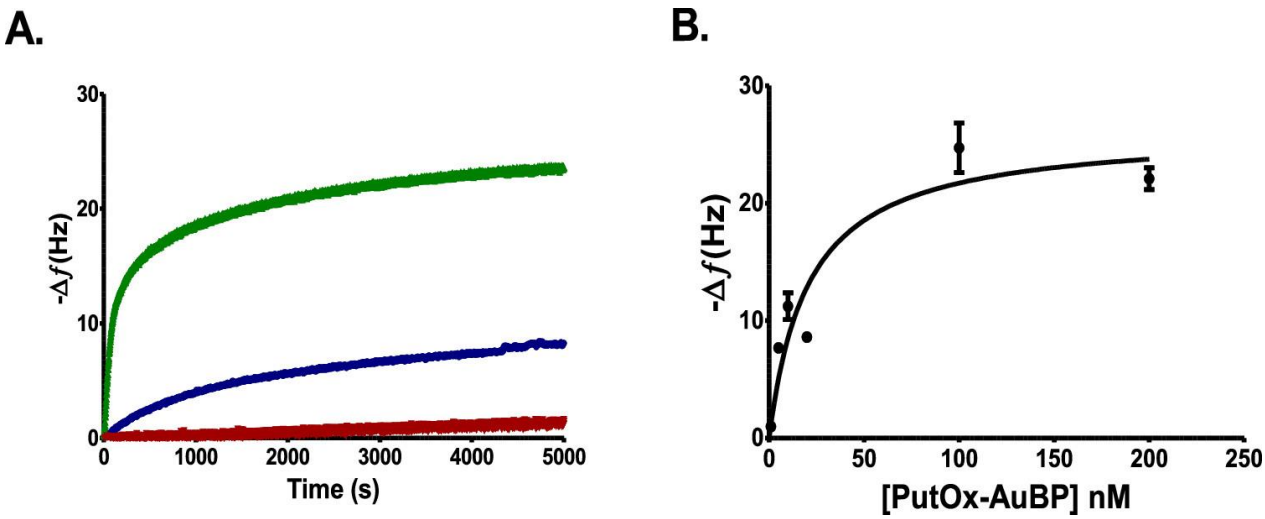

Figure 3-3 QCMD Binding Data A) QCM response curves (change in frequency vs time) for binding of PutOx(red) and PutOx-AuBP (blue at 20 nM and green at 100 nM). **B)** Concentration dependence of PutOx-AuBP binding.

The expression of the folded, functional, active protein with the peptide tag on the C-terminal end of the protein was demonstrated, while expression with the tag on the N-terminal end of the protein did not allow recovery of folded, active protein. Therefore, the tag was included on the C-terminus of the protein. The binding of the protein to gold nanoparticles and their stability under a series of washing steps showed that while both the native PutOx and the PutOx-AuBP bound to the gold nanoparticles and desorbed after washing steps, the PutOx-AuBP retained significantly more activity on the particles over time than did the PutOx. This is likely due to the higher affinity of the PutOx-AuBP for the gold, and possibly an increased stability of the PutOx-AuBP on the surface due to differences in binding. The difference in affinity for the gold was confirmed by QCM studies which showed much stronger binding of the PutOx-AuBP to the gold than the PutOx. In addition, the binding curves for the PutOx-AuBP show very little desorption of the protein from the surface when the protein solution was exchanged for the buffer only solution within the timeframe of the experiment (not shown), suggesting a very small k_d for this binding interaction. Analysis of the PutOx-AuBP/Au interaction indicated that the equilibrium binding constant (K_d) for the interaction is approximately 20 nM.

The binding and orientation of proteins at interfaces are critical for a variety of applications including biosensing and biocatalysis. In this work, the QCM and nanoparticle binding assays suggest that significant differences arise in the binding of the PutOx enzyme on gold surfaces, due to the incorporation of a relatively small peptide tag. Typically, these peptides are developed through biocombinatorial approaches including phage display to identify peptides with high affinity for a particular surface. Genetically engineered peptide sequences have been developed for a variety of materials including gold, silver, platinum, silica, and graphite. They have been shown to control the direction of protein binding at the microscale, however little is known about

the control of the orientation of the assembled proteins. Here, the binding of the PutOx has been specifically studied with and without the AuBP tag to investigate the role of the peptide tag in the binding process.

3.5.5 Protein Coverage and Orientation—AFM The binding studies using QCM and nanoparticle washing experiments indicated that the PutOx-AuBP bound considerably more tightly to gold surfaces than the enzyme lacking the AuBP tag. To probe this binding further, the PutOx and PutOx-AuBP were introduced to template-stripped gold surfaces and mica surfaces. Protein films were imaged using AFM in air after protein adsorption for 2 hours at a concentration of 10 μg/mL. The images were collected in tapping mode under ambient conditions after washing with buffer and MilliQ water followed by drying with nitrogen (see Fig. 4). In Fig. 4A, the image shows the PutOx-AuBP on Au (111). This surface has a high coverage of protein molecules compared to the very low coverage indicated in the image of the PutOx (see Fig. 4C). This is consistent with the PutOx-AuBP molecules adsorbing to the surface via the AuBP tag. In contrast, on mica, the adsorption of the PutOx-AuBP and the PutOx under conditions identical to those for binding to the gold surface are relatively low and indistinguishable from one another. The coverage is identical, and the distribution of the two different protein molecules is similar on the mica surface indicating that the interaction with the mica surface is not affected by the presence of the AuBP.

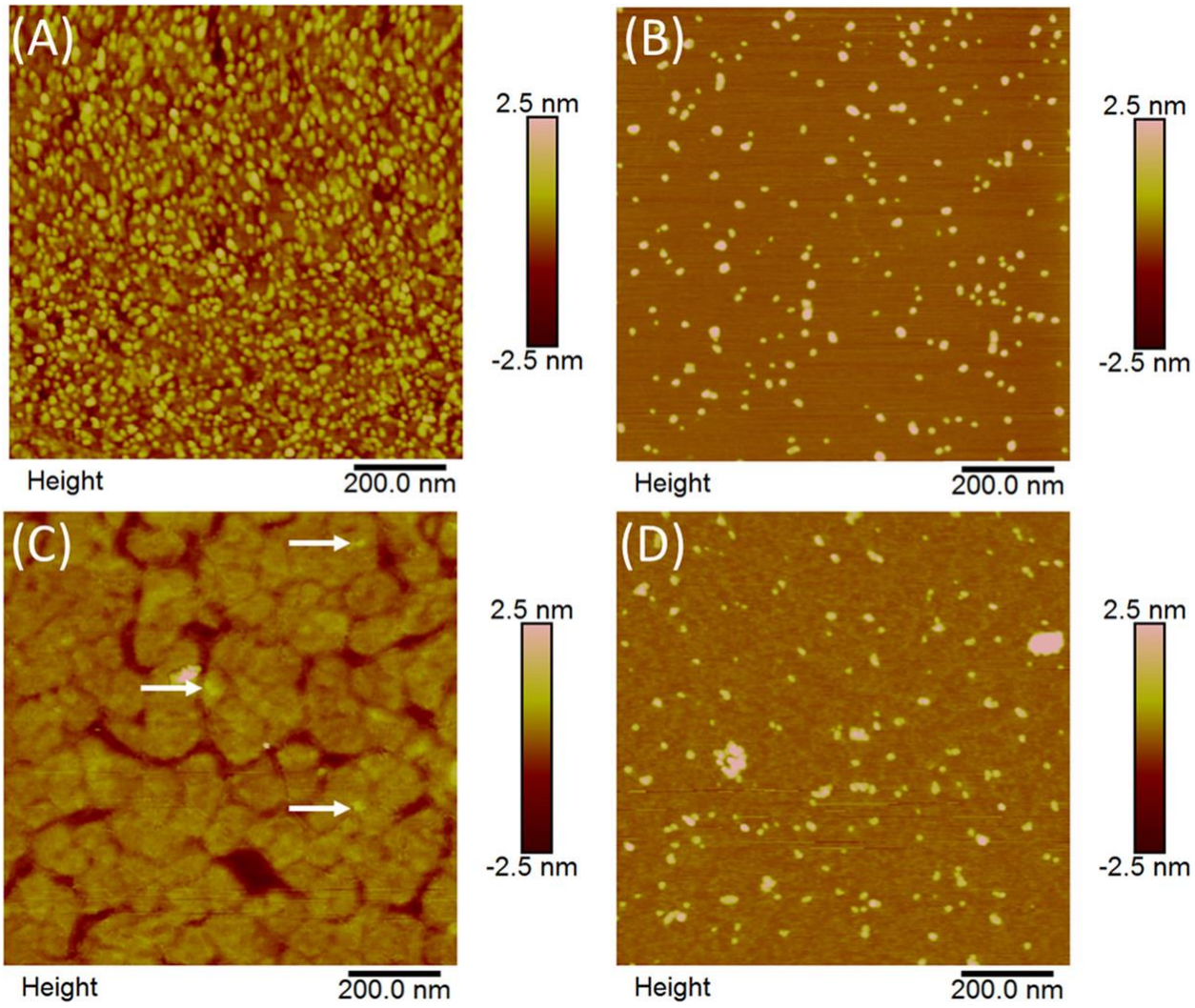

Figure 3-4 AFM images under ambient conditions of PutOxon Au(111) (A, C) and mica (B, D) surfaces. (A) PutOx-AuBP on Au(111). (B) PutOx-AuBP on mica. (C) PutOx on Au(111). (D) PutOx on mica. The white arrows show some of the PutOx molecules in figure (C).

Under low coverage conditions, AFM images of individual molecules can be analyzed to determine the single molecule dimensions of the protein. Representative images are shown in Fig. 5 along with cross-sectional profiles through the PutOx and the PutOx-AuBP molecules bound to gold. For each sample, 50 molecules were analyzed to determine the length, width (FWHM) and height of the molecules. The dimensions are reported in supplementary information (Table S2). As shown in Fig. 6, while there is little change in the length and width of the PutOx and the PutOx-AuBP, there is a significant increase in the height of the PutOx-AuBP molecules on Au compared to the PutOx. The dimensions reported here have not been deconvoluted for the tip shape, but images were recorded with the same tip under similar imaging conditions to allow direct comparison. When a similar analysis is carried out for the individual molecules on the mica surface, there is no significant difference in any of the three dimensions, again suggesting that the adsorption of the PutOx to mica is not affected by the presence of the AuBP tag, but the adsorption to gold is significantly modified. The increase in height of approximately 1 nm observed on the Au surface of bound PutOx-AuBP is significant and likely comes from a difference in how the protein is interacting with the surface. This suggests that the presence of the AuBP holds the protein away from the surface in a more vertical orientation. The significant increase in coverage of the PutOx- AuBP on Au is consistent with this difference in interaction as well as the tighter binding observed between the PutOx-AuBP and the Au in the QCM data.

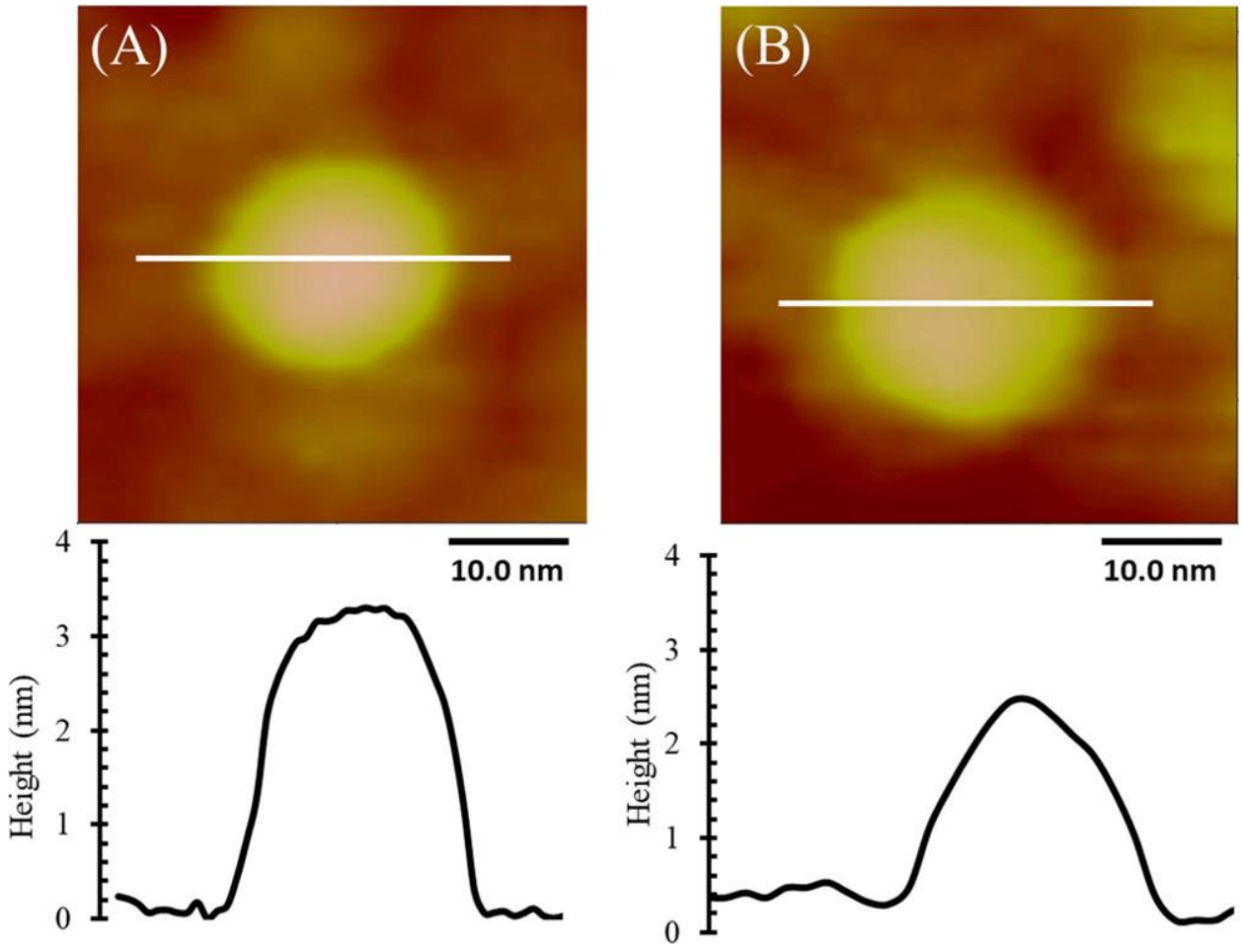

Figure 3-5 AFM images of individual molecules on the Au(111) surface along with cross-sectional profiles through the molecules along the indicated line in the image. (A) PutOx-AuBP. (B) PutOx.

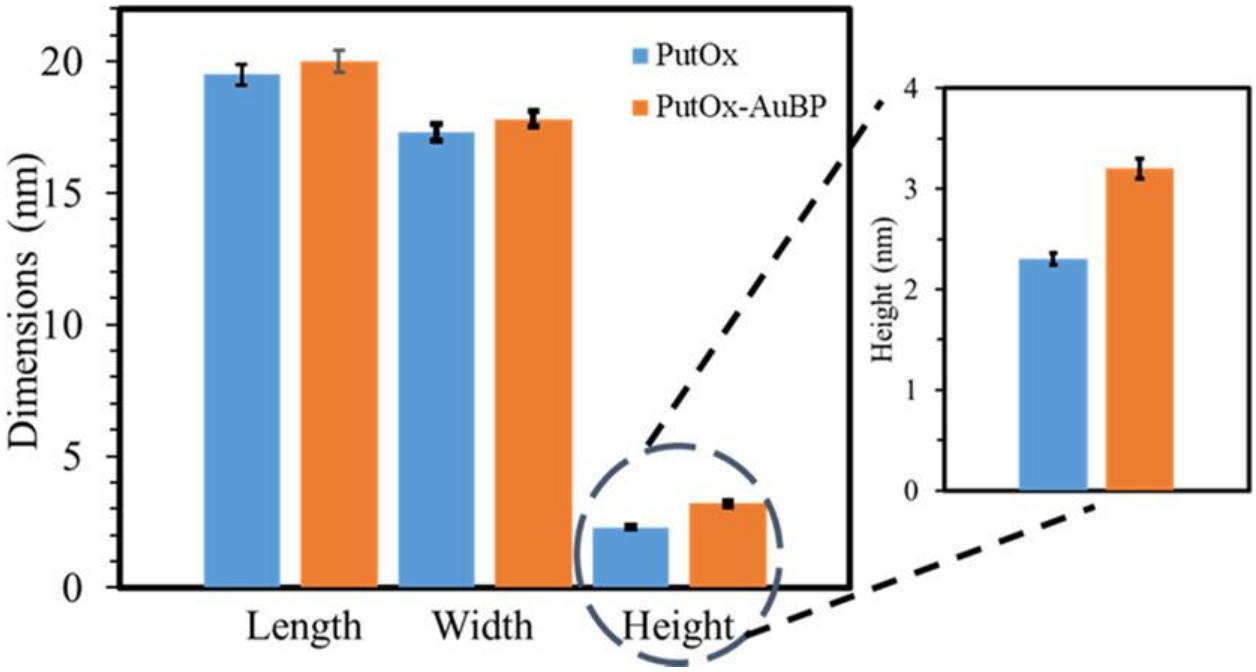

Figure 3-6 AFM-measured dimensions of PutOx-AuBP and PutOx on Au(111) The dimensions are from a single sample at three different locations, and the experiment has been replicated three times with similar results. Error bars represent 95% confidence limits based on the analysis of n = 50 molecules.

These data provide a clear link between single molecule shape and orientation and protein binding using these peptide tags. In contrast, when similar experiments were carried out on mica surfaces, there was no change in coverage or dimensions of the protein when the AFM experiments were carried out. This confirms that the differences seen between the PutOx and PutOx-AuBP binding on the gold surface are in fact due to the specific interaction between the peptide tag and the gold surface. Similar experiments have been conducted on other surfaces as well and will be the subject of a future manuscript. The fact that the binding through the AuBP tag results in significant differences in not only the protein coverage, but also the shape and orientation suggests that binding through these genetically engineered peptide tags may provide strong benefits in protein assembly at interfaces over other methods for peptide attachment, including nonspecific interactions (both covalent and noncovalent coupling) which lack the precise control of orientation and materials specificity desired. Facile, self-assembly of complex multicomponent systems necessitates material specificity as well as orientational control that binding through the engineered peptide tags affords.

3.6 Conclusions

Flavin oxidases are responsible for catalyzing the oxidation of diverse analytes with hydrogen peroxide as a product. Hydrogen peroxide production is often used as a measure of catalytic activity, making flavin oxidases attractive targets for biosensing applications. The ability of flavin oxidases to use molecular oxygen as an electron acceptor makes these enzymes industrially attractive as they are inexpensive and straightforward enzymes compared to other redox enzymes. Here, we engineered a novel flavin containing oxidase from *Rhodococcus erythropolis* NCIMB 11540, putrescine oxidase (PutOx) which is used to monitor the

degradation of biogenic amines for applications such as food spoilage and tumor biomarker detection. The detection of the electron transfer reaction in the putrescine oxidase is challenging due to the location of the flavin adenine dinucleotide (FAD) site in the protein. Controlling the orientation to provide an active conformation of the protein at the interface will impact the wider implementation of such enzymes as useful biocatalysts. To address this critical issue, we have investigated the self-assembly of PutOx on gold surfaces using a gold binding peptide, AuBP, to guide the enzyme orientation by providing a competitive binding site. The expression and purification of the novel PutOx-AuBP engineered enzyme with near native activity was demonstrated. In addition, standard activity assays showed that the functional activity of the tagged enzyme was comparable to that of the wild type enzyme. Engineered enzyme coated nanoparticles remained active on the surface after several washing cycles, whereas the activity of the wild type enzyme decreased much more rapidly with repeated washing. Binding studies using QCM spectroscopy demonstrated that the PutOx-AuBP construct bound to gold surface with higher affinity than the native PutOx. Analysis of AFM images showed that the PutOx-AuBP resulted in a higher coverage on the surface than the native PutOx under identical adsorption conditions. In addition, single molecule AFM measurements at low coverage revealed a significant difference in the height of the PutOx-AuBP and the native PutOx on the gold surface, while no such difference was observed in the case of adsorption on a mica surface. The specific attachment of functionally active PutOx via the AuBP to gold surfaces has been demonstrated using a combination of QCM, activity assays, and AFM investigations of coverage and shape of individual molecules. The increase in coverage as well as the difference in single molecule dimensions show that the binding to the gold surface is mediated by a specific interaction with the AuBP, which results in a more stably bound, functionally active protein at

the interface with a different shape than enzyme bound nonspecifically without the AuBP. This highlights the critical role of controlling specific interfacial interactions when self-assembling proteins at interfaces for an expanding list of applications of hybrid nanodevices based on proteins. Specifically, these studies demonstrate the potential for the control of binding, assembly, and orientation of active PutOx on the surface which should allow the design of much more sensitive and robust biocatalysts as well as biosensor systems based on the flavoprotein oxidases. Moreover, the technique should be readily adaptable to other enzyme systems for which it is difficult to develop a suitable biosensor platform.

3.7 Supplemental information

Table 3-2. Mutagenic inverse PCR primers used to create PutOx-AuBP and 6xHis-MBP-TEV-PutOx-AuBP encoding expression vectors from a 6xHis-MBP-TEV-PutOx encoding pTBMalE plasmid.

Primer name	Sequence
C-terminal, AuBP primer A	5'-act tcg tcg gag agc cca tcc agg aca gcc gcc gcc cgg ggc cttg ctg cgg gcg atg a-3'
C-terminal AuBP Primer B	5'-atc cga cgg cag agc tac ggg ccc tgt tga cat tgg aag tgg ata acg -3'
N-terminal AuBP primer A	5'-act tcg tcg cag agc cca tcc agg aca gcc gcc gcc cgg cat atg tat atc tcc ttc tta aa-3'
N-terminal AuBP Primer B	5'-ata cgc cga caa agt tat gga cct tgt gtg cct aca ctc cag aga ga-3'

Table 3-3 AFM measured dimensions of PutOx-AuBP and PutOx on Au(111) Error bars represent 95% confidence limits based on the analysis of n=50 molecules.

Parameter	PutOx-AuBP	PutOx
Length (nm)	20.0 ± 0.4	19.5 ± 0.4
Width (nm)	17.8 ± 0.3	17.3 ± 0.3
Height (nm)	3.2 ± 0.1	2.3 ± 0.1

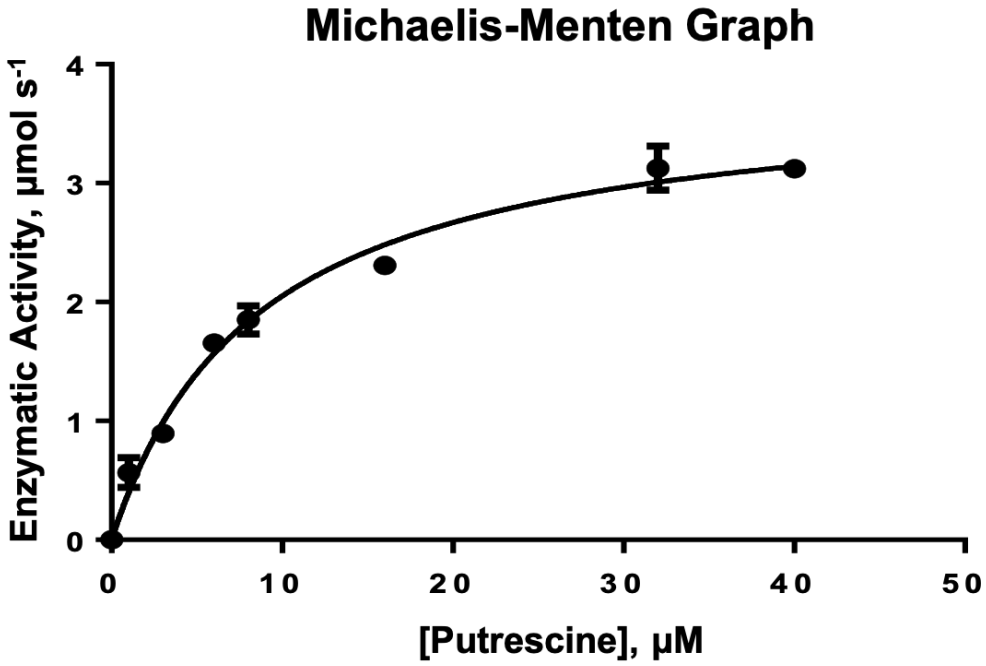

Figure 3-7 Michaelis-Menten plot of engineered enzyme, PutOx-AuBP, for determination of kinetic parameters

3.8 Bibliography

1. Torres Pazmiño, D. E.; Winkler, M.; Glieder, A.; Fraaije, M. W., Monooxygenases as biocatalysts: classification, mechanistic aspects and biotechnological applications. *J Biotechnol* **2010,** *146* (1-2), 9-24.

2. Ceccoli, R. D.; Bianchi, D. A.; Rial, D. V., Flavoprotein monooxygenases for oxidative biocatalysis: recombinant expression in microbial hosts and applications. *Front. Microbiol.* **2014,** *5*, 1-14.

3. Dong, J. J.; Fernández-Fueyo, E.; Hollmann, F.; Paul, C. E.; Pesic, M.; Schmidt, S.; Wang, Y.; Younes, S.; Zhang, W., Biocatalytic oxidation reactions: a chemist's perspective. *Angew. Chem. Int. Ed.* **2018,** *57*, 9238-9261.

4. Montersino, S.; Tischler, D.; Gassner, G. T.; Van Berkel, W. J. H., Catalytic and structural features of flavoprotein hydroxylases and epoxidases. *Adv Synth Catal* **2011,** *353*, 2301-2319.

5. Moonen, M. J. H.; Fraaije, M. W.; Rietjens, I. M. C. M.; Laane, C.; Van Berkel, W. J. H., Flavoenzyme-Catalyzed Oxygenations and Oxidations of Phenolic Compounds. *Adv Synth Catal* **2002,** *344*, 1023-1035.

6. Ullrich, R.; Hofrichter, M., Enzymatic hydroxylation of aromatic compounds. *Cell Mol Life Sci* **2007,** *64* (3), 271-293.

7. Bankar, S. B.; Bule, M. V.; Singhal, R. S.; Ananthanarayan, L., Glucose oxidase - An overview. *Biotechnol. Adv* **2009,** *27* (4), 489-501.

8. Tzanov, T.; Costa, S. A.; Gbitz, G. M.; Cavaco-Paulo, A., Hydrogen peroxide generation with immobilized glucose oxidase for textile bleaching. *J Biotechnol* **2002,** *93* (1), 87-94.

9. Wilson, R.; Turner, A. P. F., Glucose oxidase: an ideal enzyme. *Biosens. Bioelectron.* **1992,** *7* (3), 165-85.

10. Kopacz, M. M.; Heuts, D. P. H. M.; Fraaije, M. W., Kinetic mechanism of putrescine oxidase from Rhodococcus erythropolis. *FEBS Journal* **2014,** *281* (19), 4384-4393.

11. Kopacz, M. M.; Rovida, S.; van Duijn, E.; Fraaije, M. W.; Mattevi, A., Structure-based redesign of cofactor binding in putrescine oxidase. *Biochemistry* **2011,** *50* (19), 4209-17.

12. Van Hellemond, E. W.; Van Dijk, M.; Heuts, D. P. H. M.; Janssen, D. B.; Fraaije, M. W., Discovery and characterization of a putrescine oxidase from Rhodococcus erythropolis NCIMB 11540. *Appl. Microbiol.* **2008,** *78* (3), 455-463.

13. Bka, B.; Adnyi, N.; Szamos, J.; Virg, D.; Kiss, A., Putrescine biosensor based on putrescine oxidase from Kocuria rosea. *Enzyme Microb. Technol.* **2012,** *51* (5), 258-262.

14. Inaba, Y.; Tokishita, S.; Hamada-Sato, N.; Kobayashi, T.; Imada, C.; Yamagata, H.; Watanabe, E., Development of agmatine sensor using the combination of putrescine oxidase and agmatinase for squid freshness. *Biosens. Bioelectron.* **2004,** *20* (4), 833-840.

15. Lee, J. I.; Jang, J. H.; Yu, M. J.; Kim, Y. W., Construction of a bifunctional enzyme fusion for the combined determination of biogenic amines in foods. *Agric. Food Chem.* **2013,** *61* (38), 9118-9124.

16. Nagy, L.; Nagy, G.; Gyurcsnyi, R. E.; Neuman, M. R.; Lindner, E., Development and study of an amperometric biosensor for the in vitro measurement of low concentration of putrescine in blood. *J Biochem Bioph Meth* **2002,** *53* (1-3), 165-175.

17. Rochette, J. F.; Sacher, E.; Meunier, M.; Luong, J. H. T., A mediatorless biosensor for putrescine using multiwalled carbon nanotubes. *Anal. Biochem.* **2005,** *336* (2), 305-311.

18. Casero, R. A.; Marton, L. J., Targeting polyamine metabolism and function in cancer and other hyperproliferative diseases. *Nat. Rev. Drug Discov.* **2007,** *6* (5), 373-390.

19. Liu, R.; Lin, X.; Li, Z.; Li, Q.; Bi, K., Quantitative metabolomics for investigating the value of polyamines in the early diagnosis and therapy of colorectal cancer. *Oncotarget* **2018,** *9* (4), 4583-4592.

20. Kalač, P.; Krausová, P., A review of dietary polyamines: Formation, implications for growth and health and occurrence in foods. *Food Chem.* **2005,** *90* (1-2), 219-230.

21. Bardcz, S., Polyamines in food and their consequences for food quality and human health. *Trends Food Sci. Tech.* **1995,** *6* (10), 341-346.

22. Kalač, P., Health effects and occurrence of dietary polyamines: A review for the period 2005-mid 2013. *Food Chem.* **2014,** *161*, 27-39.

23. Reverte, L.; Prieto-Simon, B.; Campas, M., New advances in electrochemical biosensors for the detection of toxins: Nanomaterials, magnetic beads and microfluidics systems. A review. *Anal Chim Acta* **2016,** *908*, 8-21.

24. Muguruma, H.; Iwasa, H.; Hidaka, H.; Hiratsuka, A.; Uzawa, H., Mediatorless direct electron transfer between flavin adenine dinucleotide-dependent glucose dehydrogenase and single-walled carbon nanotubes. *ACS Catalysis* **2017,** *7* (1), 725-734.

25. Sarikaya, M.; Tamerler, C.; Schwartz, D. T.; Baneyx, F., Materials assembly and formation using engineered polypeptides. *Annu. Rev. Mater. Res.* **2004,** *34*, 373-408.

26. Schulz, C.; Kittl, R.; Ludwig, R.; Gorton, L., Direct electron transfer from the FAD cofactor of cellobiose dehydrogenase to electrodes. *ACS Catalysis* **2016,** *6* (2), 555-563.

27. So, C. R.; Kulp, J. L.; Oren, E. E.; Zareie, H.; Tamerler, C.; Evans, J. S.; Sarikaya, M., Molecular recognition and supramolecular self-assembly of a genetically engineered gold binding peptide on Au(111). *ACS Nano* **2009,** *3* (6), 1525-1531.

28. Tamerler, C.; Sarikaya, M., Molecular biomimetics: genetic synthesis, assembly, and formation of materials using peptides. *MRS Bulletin* **2008,** *33* (5), 504-512.

29. Willner, I., Biomaterials for sensors, fuel cells, and circuitry. *Science* **2002,** *298*, 2407-2409.

30. Willner, I.; Willner, B., Biomolecule-based nanomaterials and nanostructures. *Nano Lett.* **2010,** *10*, 3805-3815.

31. Tamerler, C.; Duman, M.; Oren, E. E.; Gungormus, M.; Xiong, X.; Kacar, T.; Parviz, B. A.; Sarikaya, M., Materials specificity and directed assembly of a gold-binding peptide. *Small* **2006,** *2* (11), 1372-1378.

32. Woodbury, R. G.; Wendin, C.; Clendenning, J.; Melendez, J.; Elkind, J.; Bartholomew, D.; Brown, S.; Furlong, C. E., Construction of biosensors using a gold-binding polypeptide and a miniature integrated surface plasmon resonance sensor. *Biosens. Bioelectron.* **1998,** *13* (10), 1117-1126.

33. Haussmann, A.; Milde, P.; Erler, C.; Eng, L. M., Ferroelectric lithography: Bottom-up assembly and electrical performance of a single metallic nanowire. *Nano Lett.* **2009,** *9* (2), 763-768.

34. Hnilova, M.; Khatayevich, D.; Carlson, A.; Oren, E. E.; Gresswell, C.; Zheng, S.; Ohuchi, F.; Sarikaya, M.; Tamerler, C., Single-step fabrication of patterned gold film array by an engineered multi-functional peptide. *J. Colloid Interface Sci.* **2012,** *365* (1), 97-102.

35. Kacar, T.; Zin, M. T.; So, C.; Wilson, B.; Ma, H.; Gul-Karaguler, N.; Jen, A. K.; Sarikaya, M.; Tamerler, C., Directed self-immobilization of alkaline phosphatase on micro-patterned substrates via genetically fused metal-binding peptide. *Biotechnol. Bioeng.* **2009,** *103* (4), 696-705.

36. David S. Ginger, H. Z., and Chad A. Mirkin, The evolution of dip-Pen nanolithography. *Angew. Chem. Int. Ed.* **2004,** *43*, 30-45.

37. Khalid Salaita, Y. W., Chad A. Mirkin, Applications of dip-pen nanolithography. *Nat. Nanotechnol.* **2007,** *2*, 146-155.

38. Joydeep Lahiri, E. O., and George M. Whitesides, Patterning ligands on reactive SAMs by microcontact printing. *Langmuir* **1999,** *15*, 2055-2060.

39. Fenter, P.; Eisenberger, P.; Li, J.; Camillone, N.; Bernasek, S.; Scoles, G.; Ramanarayanan, T. A.; Liang, K. S., Structure of $CH_3(CH_2)_{17}SH$ Self-assembled on the Ag(111) surface: an incommensurate monolayer. *Langmuir* **1991,** *7* (10), 2013-2016.

40. Leong, K.; Chen, Y.; Masiello, D. J.; Zin, M. T.; Hnilova, M.; Ma, H.; Tamerler, C.; Sarikaya, M.; Ginger, D. S.; Jen, A. K. Y., Cooperative near-field surface plasmon enhanced quantum dot nanoarrays. *Adv. Funct. Mater.* **2010,** *20* (16), 2675-2682.

41. Porter, M. D.; Bright, T. B.; Allara, D. L.; Chidsey, C. E., Spontaneously organized molecular assemblies. 4. structural characterization of n-alkyl thiol monolayers on gold by optical ellipsometry, infrared spectroscopy, and electrochemistry. *J. Am. Chem. Soc.* **1987,** *109* (12), 3559-3568.

42. Sarikaya, M.; Aksay, I. A., Biomimetics : design and processing of materials. In *AIP series in polymers and complex materials*, 1995; pp 147-160.

43. So, C. R.; Hayamizu, Y.; Yazici, H.; Gresswell, C.; Khatayevich, D.; Tamerler, C.; Sarikaya, M., Controlling self-assembly of engineered peptides on graphite by rational mutation. *ACS Nano* **2012,** *6* (2), 1648-56.

44. Akdim, B.; Pachter, R.; Kim, S. S.; Naik, R. R.; Walsh, T. R.; Trohalaki, S.; Hong, G.; Kuang, Z.; Farmer, B. L., Electronic properties of a graphene device with peptide adsorption: Insight from simulation. *ACS Appl. Mater. Interfaces* **2013,** *5* (15), 7470-7477.

45. Sarikaya, M.; Tamerler, C.; Jen, A. K. Y.; Schulten, K.; Baneyx, F., Molecular biomimetics: Nanotechnology through biology. *Nat. Mater.* **2003,** *2*, 577-585.

46. Tamerler, C.; Khatayevich, D.; Gungormus, M.; Kacar, T.; Oren, E. E.; Hnilova, M.; Sarikaya, M., Molecular biomimetics: GEPI-based biological routes to technology. *Biopolymers* **2010,** *94* (1), 78-94.

47. Evans, J. S.; Samudrala, R.; Walsh, T. R.; Oren, E. E.; Tamerler, C., Molecular design of inorganic-binding polypeptides. *MRS Bulletin* **2008,** *33* (5), 514-518.

48. Hnilova, M.; Karaca, B. T.; Park, J.; Jia, C.; Wilson, B. R.; Sarikaya, M.; Tamerler, C., Fabrication of hierarchical hybrid structures using bio-enabled layer-by-layer self-assembly. *Biotechnol. Bioeng.* **2012,** *109* (5), 1120-1130.

49. Hnilova, M.; Liu, X.; Yuca, E.; Jia, C.; Wilson, B.; Karatas, A. Y.; Gresswell, C.; Ohuchi, F.; Kitamura, K.; Tamerler, C., Multifunctional protein-enabled patterning on arrayed ferroelectric materials. *ACS Appl. Mater. Interfaces* **2012,** *4* (4), 1865-1871.

50. Hnilova, M.; So, C. R.; Oren, E. E.; Wilson, B. R.; Kacar, T.; Tamerler, C.; Sarikaya, M., Peptide-directed co-assembly of nanoprobes on multimaterial patterned solid surfaces. *Soft Matter* **2012,** *8* (16), 4327-4334.

51. Hu, Y.; Mitchell, K. M.; Albahadily, F. N.; Michaelis, E. K.; Wilson, G. S., Direct measurement of glutamate release in the brain using a dual enzyme-based electrochemical sensor. *Brain Research* **1994,** *659* (1-2), 117-125.

52. Wilson, G. S.; Gifford, R., Biosensors for real-time in vivo measurements. *Biosens. Bioelectron.* **2005,** *20* (12), 2388-2403.

53. Wilson, G. S.; Hu, Y., Enzyme-based biosensors for in vivo measurements. *Chem. Rev* **2000,** *100* (7), 2693-2704.

54. Karaca, B. T.; Hnilova, M.; Tamerler, C., Addressable biological functionalization of inorganics: Materials-selective fusion proteins in bio-nanotechnology. In *Bio-Inspired Nanotechnology*, Springer: New York, 2014; pp 221-255.

55. VanOosten, S. K.; Yuca, E.; Karaca, B. T.; Boone, K.; Snead, M. L.; Spencer, P.; Tamerler, C., Biosilver nanoparticle interface offers improved cell viability. *Surf Innov* **2016,** *4* (3), 121-132.

56. Yuca, E.; Karatas, A. Y.; Seker, U. O. S.; Gungormus, M.; Dinler-Doganay, G.; Sarikaya, M.; Tamerler, C., In vitro labeling of hydroxyapatite minerals by an engineered protein. *Biotechnol. Bioeng.* **2011,** *108* (5), 1021-1030.

57. Yucesoy, D. T.; Karaca, B. T.; Cetinel, S.; Caliskan, H. B.; Adali, E.; Gul-Karaguler, N.; Tamerler, C., Direct bioelectrocatalysis at the interfaces by genetically engineered dehydrogenase. *Bioinspir. Biomim. Nan.* **2015,** *4* (1), 79-89.

58. Zhang, S.; Karaca, B. T.; Vanoosten, S. K.; Yuca, E.; Mahalingam, S.; Edirisinghe, M.; Tamerler, C., Coupling infusion and gyration for the nanoscale assembly of functional polymer nanofibers integrated with genetically engineered proteins. *Macromol. Rapid Commun.* **2015,** *36* (14), 1322-1328.

59. Tropea, J. E.; Cherry, S.; Waugh, D. S., Expression and purification of soluble His(6)-tagged TEV protease. *Methods Mol Biol* **2009,** *498*, 297-307.

60. Vogel, N.; Zieleniecki, J.; Köper, I., As flat as it gets: ultrasmooth surfaces from template-stripping procedures. *Nanoscale* **2012,** *4*, 3820-3832.

61. Wagner, P.; Hegner, M.; Guntherodt, H.-J.; Semenza, G., Formation and in Situ Modification of Monolayers Chemisorbed on Ultraflat Template-Stripped Gold Surfaces. *Langmuir* **1995,** *11*, 3867-3875.

62. Hegner, M.; Wagner, P.; Semenza, G., Ultralarge atomically flat template-stripped Au surfaces for scanning probe microscopy. *Surface Science* **1993,** *291*, 39-46.

63. Hu, J.; Qin, H.; Gao, F. P.; Cross, T. A., A systematic assessment of mature MBP in membrane protein production: overexpression, membrane targeting and purification. *Protein Expr Purif* **2011,** *80* (1), 34-40.

64. Mishin, V.; Gray, J. P.; Heck, D. E.; Laskin, D. L.; Laskin, J. D., Application of the Amplex red/horseradish peroxidase assay to measure hydrogen peroxide generation by recombinant microsomal enzymes. *Free Radic. Biol. Med.* **2010,** *48* (11), 1485-1491.

65. Zhou, M.; Diwu, Z.; Panchuk-Voloshina, N.; Haugland, R. P., A stable nonfluorescent derivative of resorufin for the fluorometric determination of trace hydrogen peroxide: applications in detecting the activity of phagocyte NADPH oxidase and other oxidases. *Anal. Biochem.* **1997,** *253* (2), 162-168.

66. Tamerler, C.; Oren, E. E.; Duman, M.; Venkatasubramanian, E.; Sarikaya, M., Adsorption kinetics of an engineered gold binding Peptide by surface plasmon resonance spectroscopy and a quartz crystal microbalance. *Langmuir* **2006,** *22* (18), 7712-8.

4 Improving the Kinetic Parameters of Nicotine Oxidizing Enzymes by Homologous Structure Comparison and Rational Design

4.1 Authorship and Publication Information

This work by the author was submitted to ACS *Biochemistry* on 26th April 2021 under the following title and authorship series and is reproduced here with minor formatting revisions. It is a work contributed to by all listed authors.

Improving the Kinetic Parameters of Nicotine Oxidizing Enzymes by Homologous Structure Comparison and Rational Design

Dwight O. Deay III[1], Steve Seibold[1], Kevin P. Battaile[3], Scott Lovell[2],

Mark L. Richter[1], and Peter A. Petillo[*4]*

[1]Department of Molecular Biosciences, University of Kansas, Lawrence, KS 66045

[2]Protein Structure Laboratory, University of Kansas, Lawrence, KS 66044,

[3]NYX, New York Structural Biology Center, Upton, NY 11973, USA

[4*]Design-Zyme LLC, Lawrence KS 66045

Keywords: nicotine oxidase, nicotine binding, 3D structure, nicotine, 6-hydroxynicotine, protein engineering, flavin, flavoprotein

4.2 Abstract

Demand exists for a nicotine oxidase enzyme with high catalytic efficiency for a variety of applications including the *in vivo* detection of nicotine, therapeutic enzymatic blockade of nicotine from the CNS, and inactivation of toxic industrial wastes generated in the manufacture of tobacco products. Nicotine oxidase enzymes identified to date suffer from low efficiency, exhibiting either a high k_{cat} or low K_m, but not both. Here we present the crystal structure of the (S)-6-hydroxy-nicotine-oxidase from *Shinella sp* HZN7 (NctB), an enzyme that oxidizes (S)-nicotine with a high k_{cat} (>1 s^{-1}), that possesses remarkable structural homology to an enzyme with a nanomolar K_m for (S)-nicotine, the (S)-nicotine oxidase from *Pseudomonas putidia* strain S16 (NicA2). Based on a comparison of our NctB structure and the previously published crystal structure of NicA2, we successfully employed a rational design approach to increase the rate of oxidative turnover of the NicA2 enzyme by ~25% (0.011 s^{-1} to 0.014 s^{-1}), and reduce the K_m of the NctB protein by approximately 34% (940 μM to 622 μM). These results are a significant step forward towards engineering a nicotine oxidase with kinetic parameters that fulfill the functional requirements of biosensing, waste remediation, and therapeutic applications.

4.3 Introduction

Significant demand exists for enzymes capable of degrading nicotine *in vivo*.[1-6] Among the uses for such enzymes are the enzymatic breakdown of nicotine prior to entry into the CNS,[2, 3, 7] remediation of toxic industrial waste streams generated during the manufacture of tobacco products,[8] and the potential for the *in vivo* detection of nicotine levels via an amperometric biosensor.

Among the most promising nicotine degrading enzymes is the nicotine oxidoreductase identified in the genome of *Pseudomonas putida* strain S16 (UniProtKB: F8G0P2, NicA2).[9] The potential medical use of NicA2 for the treatment of nicotine dependence via enzymatic blockade of the CNS has been explored with some success.[2, 3, 7] Despite the remarkable ability of NicA2 to reduce blood (S)-nicotine levels and nicotine dependence in mice, the extremely slow k_{cat} of 6.1×10^{-2} s^{-1},[6] requires impractical doses of enzyme, as high as 10-75 mg kg^{-1},[3] to provide sufficient activity to achieve *in vivo* efficacy. Fast kinetic analysis of the mechanism of NicA2 has identified oxidation of the reduced FAD cofactor as the rate limiting step in the catalytic cycle of the enzyme, an observation that prompted speculation that the gene product was in fact a dehydrogenase with an unidentified electron acceptor.[1]

Recently, the low k_{cat} of NicA2 was explained by the discovery of a cytochrome C like protein encoded proximally to the NicA2 gene in the *P. putida* S16 genome. This protein rapidly reoxidizes the NicA2 flavin with a $k_{cat} = 27 \pm 1$ s^{-1},[10] demonstrating the need of both proteins for nicotine catabolism in *P. putida*. Indeed, when this cytochrome C like protein is knocked-out, the modified *P. putida* fails to grow on nicotine in minimal medium as compared to the wild-type organism. This discovery suggests that efforts to increase the oxidative turnover of NicA2 to enhance its suitability for practical applications is likely complicated by the absence of

evolved structural elements that promote oxygen reactivity. Said alternatively, NicA2 is not an oxidase enzyme but rather a dehydrogenase.[10]

The comparison of the NicA2 structure with related flavin amine oxidases that rapidly reduce molecular oxygen has been proposed to provide insight into how the NicA2 enzyme might be engineered to act efficiently as an oxidase.[10] Some success has been achieved in this regard by comparing the structure of NicA2 to the closest existing homolog in the Protein Databank (PDB), the (S)-6-hydroxy-nicotine oxidase from *A. nicotinovirans* (6HLNO).[1] While turning over nicotine at a significant rate (~0.3 s^{-1}), 6HLNO suffers from a millimolar K_m for (S)-nicotine, as this is not the enzyme's native substrate.[11] We previously attempted to improve the kinetic parameters (k_{cat} and K_m) of the 6HLNO by enhancing the chemical complementarity of the active site for (S)-nicotine in the hope of reducing the K_m into pharmacologically relevant concentration range. This effort was met with limited success.[11]

We now present the crystal structure of the (S)-6-hydroxy-nicotine oxidase from *Shinella sp.* Strain HZN7 (UniProtKB: A0A075BSX9, NctB) at 1.55Å resolution. We anticipated that this enzyme would provide a better scaffold for the rational design of a nicotine oxidase because NctB possesses significantly higher sequence homology to the NicA2 (43% identity) compared to 6HLNO (26% identity) or any other protein structure deposited in the PDB. Furthermore, the NctB enzyme was reported to turn over (S)-nicotine at a greater rate than the 6HLNO,[12] and like most other flavin dependent amine oxidases, NctB has high oxygen reactivity and thus it does not require an external acceptor.

Upon solving the crystal structure of NctB, we noted that the structural homology of NctB and NicA2 (TM-Align RMSD =1.1Å) was greater than that of the NicA2 and the 6HLNO (TM-Align RMSD = 2.6Å). This alignment, in addition to a computationally derived model for the structure

of substrate bound NctB, has allowed us to speculate on the structural basis of NicA2's high affinity for (S)-nicotine and the high oxygen reactivity of NctB. These insights informed a successful attempt at structure based rational design to improve both the oxidative turnover of NicA2 and the affinity of NctB for (S)-nicotine. While the results of the rational design efforts reported herein are modest, they point to the viability of comparing the structure of related nicotine degrading enzymes, some of which possess fast oxidative half reactions and some of which have very low K_m values, to inform the engineering of a highly efficient nicotine oxidase.

Ultimately, if an engineered enzyme were to possess both the oxygen reactivity of NctB and the low K_m of NicA2, then the dosage of such an enzyme as an anti-addiction therapy could be reduced by the ratio of the k_{cat} values, or ~120-fold. This dosage is far more practical and would allow for a therapeutic excess to be delivered, ensuring that treatment would have an extended duration of action. Additionally, a nicotine oxidase with a rate of turnover above 1 s^{-1} under pharmacologically relevant nicotine concentrations would enable the fabrication of a fully functioning *in vivo* biosensor. Such a device would allow researchers to measure CNS nicotine dynamics in real time with high temporal and spatial resolution, potentially enabling critical research on the nicotine reward pathways in the brain and the development of nicotine addiction.

4.4 Materials and Methods

4.4.1 Cloning Duplex DNA encoding the NctB gene from *Shinella* sp. HZN7(UniprotKB: A0A075BSX9) and the NicA2 gene from *Pseudomonas Putida*(S16) (UniprotKB:F8G0P2), were obtained from Integrated DNA Technologies. The genes were cloned into the T7 promoter driven expression plasmid pTBSG, which encodes a N-terminal 6xHis tag and TEV protease site upstream of the insertion site, by ligation independent cloning.

4.4.2 Site Directed Mutagenesis : Mutations informed by the alignment of NctB and NicA2 crystal structures were generated in the native NctB expression plasmid ORF via the Quickchange site-directed mutagenesis kit (Agilent). Plasmid DNA was purified from mutant transformant colonies and the mutation validated by Sanger sequencing.

4.4.3 Protein expression Sequenced expression plasmid DNA from either LIC or site directed mutagenesis was used to transform BL21 (*DE3*) pRARE expression cells. Isolated transformant colonies were used to inoculate 25 mL LB shake flask starter cultures supplemented with 100 ug/mL carbenicillin which were grown overnight at 30 ºC with 350 rpm shaking. Subsequently, the starter culture was added to 1L of terrific broth media supplemented with 200 μg/mL carbenicillin and 10 mM $MgCl_2$. The expression culture was incubated at 37 ºC with shaking at 350 rpm until an OD600 of 0.6 was reached, at which point the incubator temperature was reduced to 15 ºC and the density monitored until an OD600 of 1.0 - 1.5. Protein expression was induced by addition of IPTG to 100 μM. Supplemental glycerol (0.5% v/v) was also added. After 24 h of additional expression, cells were chilled to 4 ºC and harvested by centrifugation at 2744 RCF for 10 minutes. Cell pellets were resuspended in 100 mL lysis buffer (50 mM Tris-HCL, pH 8.0, 300 mM NaCl, 10 mM imidazole) and frozen at -80 ºC until purification.

4.4.4 Protein purification Cells suspensions were thawed and sonicated in an ice water bath using a Branson model 400 sonifier (2s on, 10 s off at 30% amplitude for 10 min). The lysate was clarified by centrifugation 20,000 RCF for 1 hr at 4 ºC. The soluble fraction was gently mixed with 5 mL of Qiagen Superflow™ Ni-NTA resin equilibrated with lysis buffer. The resin slurry was loaded onto a 1.6 cm x 30 cm gravity fed column (Biorad) and washed with 20 column volumes of lysis buffer followed by 20 column volumes of lysis buffer supplemented with 3M imidazole stock to yield a final imidazole concentration of 20mM. The protein was then eluted with 1.5 column volumes of lysis buffer supplemented with 3M imidazole stock to yield a final imidazole concentration of 250 mM. Yields were typically greater than 50 mg/L as determined by a Bradford assay.[13] Prior to crystallization, the N-terminal His tag was removed from the *wt*-NctB by digestion of the Ni-NTA eluate with tobacco etch virus protease (TEV) as previously reported.[14] To the Ni-NTA eluate, DTT was added to 5mM and EDTA-Na added to 1mM, prior to the addition of TEV protease, prepared by a previously reported method.[14] TEV was added to a mass ratio of 1:20 and the sample incubated at 4 ^{O}C for 48 h. The protease digestion reaction was then buffer exchanged into lysis buffer to remove free DTT and EDTA, followed by the removal of TEV protease and cleaved N-terminal 6xHis fragments by application of the sample to a Qiagen Ni-NTA superflow column. The NctB protein was recovered in the flowthrough and concentrated to 75 mg/mL before being submicron filtered and applied to a Superdex G-200 increase column equilibrated with gel filtration buffer (10 mM HEPES-OH pH 7.4, 140 mM NaCl, 0.02% NaN_3). The fractions containing the predominant, yellow, low Mw peak were collected and pooled. The purified NctB sample concentration was adjusted to 10 mg/ml prior to crystallization either by dilution with gel filtration buffer or by ultrafiltration in an Amicon™ ultrafiltration device.

4.4.5 Crystallization and Data Collection A sample of purified *wt*-NctB was concentrated to 10 mg/mL in 10 mM HEPES-OH pH 7.5 for crystallization. Crystallization screening was conducted in Compact 300 (Rigaku Reagents) sitting drop vapor diffusion plates at 20 ^{o}C using equal volumes of protein and crystallization solution and then equilibrated against 75 μL of the latter solution. Crystals displaying a cuboctahedron morphology were observed after 1 day from the Proplex HT (Molecular Dimensions) screen condition H8 (25% MPD, 50 mM Calcium Acetate, 0.1 M Cacodylate pH 6.0). Native samples were transferred briefly to a fresh drop containing 35% MPD, 50 mM Calcium Acetate, .1 M Cacodylate pH 6.0, 1 mM FAD and heavy atom derivative crystals were prepared by soaking in 35% MPD, 50 mM Calcium Acetate, .1 M Cacodylate pH 6.0, 1 mM FAD, 100 μM K_2PtCl_4 overnight. Samples were harvested and stored in liquid nitrogen prior to data collection. X-ray diffraction data were collected at the Advanced Photon Source beamline 17-ID using a Dectris Pilatus 6M pixel array detector.

4.4.6 Structure Solution and Refinement Intensities for all data sets were integrated using XDS[15] via Autoproc[16] and the Laue class analysis and data scaling were performed with Aimless.[17, 18] The highest probability Laue class was -3*m* and space group $P3_121$. Based on the Matthew's coefficient,[19] the asymmetric unit contained 1 molecule (V_m= 2.16 Å^3/Da, 43.05% solvent). Structure solution was conducted by SAD phasing with Crank2[20] using the data obtained from K_2PtCl_4 soaked crystals. The resulting model was used for molecular replacement searches, against the native data, with Phaser[21] and the top solution was found in the space group $P3_121$. The model was refined and manually built using Phenix[22] and Coot[23] respectively. Disordered side chain atoms were truncated to the point where electron density could be observed. Structure validation was conducted with Molprobity[24] and figures were prepared with CCP4mg.[25] Relevant crystallographic data are provided in Table 1.

4.4.7 Docking of (S)-6-hydroxy-nicotine into NctB with AutoDock Vina The crystal structure of NctB was prepared for docking using AutoDockTools.[26] Crystallographic waters and MPD ligands were removed from the crystal structure, polar hydrogens were added, and partial charges were automatically assigned to the (S)-6-hydroxy-nicotine ligand and protein. A grid box of 20 $Å^3$ was centered at the active site, and the docking of (S)-6-hydroxy-nicotine performed using AutoDock Vina[27] (without flexible side chains, exhaustiveness parameter = 200). Only the lowest energy structure was docked in a catalytically competent conformation based on the distance between, and alignment of, the C4 bound hydrogen of (S)-6-hydroxy-nicotine and N5 of the FAD cofactor. All other docked structures were discarded. A similar set of calculations were performed using the Molecular Operating Environment (MOE) from the Chemical Computing Group.[28] Unlike the AutoDock Vina calculations, the MOE calculations failed to reproduce the salient features of the (S)-nicotine bound NicA2 structure (data not shown) and did not produce catalytically competent docked structures. For the purposes of this report, only the AutoDock Vina results will be discussed.

4.4.8 Alignment of protein structures of NicA2, NctB, and HLNO: : The program TM-Align[29] was used to generate alignments between NctB and its closest homolog NicA2 which were visualized in PyMOL™.[30] Because the alignment proved sufficient for our rational design effort, no further attempt was made to perform domain localized docking.

4.4.9 Assay of NicA2 and NctB variants All variants were assayed using a variation of the Amplex Red™ peroxidase assay.[31] Proteins were prepared for assay by buffer exchange into 50 mM $NaPO_4$ pH 7.4 buffer by gel filtration on Sephadex G50-Fine media followed by triplicate Bradford assays.[13] Each assay was performed by combining (*i*) 500 μL of a solution comprised of 50 mM $NaPO_4$ pH 7.4, 50 μM Amplex Red™, 0.1 U / mL of Horse Radish Peroxidase, and the enzyme variant being assayed at twice the target final enzyme concentration with (*ii*) 500 μL of a solution containing 50 mM $NaPO_4$ pH 7.4 and (S)-nicotine at twice the final assay concentration. The NctB variants were assayed at an enzyme concentration of 10 μg/mL. (S)-nicotine was purchased from TCI America and purified by vacuum distillation under argon and stored under argon at -80 ºC. The change in absorbance of the assay reactions was measured continuously on a Cary 50 UV/Vis spectrophotometer. The rate of change in product concentration was determined by fitting the kinetics data via least squares linear regression to determine the optical velocity and dividing this value by the slope of an experimentally determined peroxide standard curve (30,800 A cm^{-1} M^{-1}). Chemical velocity data were transformed to unimolecular turnover by dividing by the total enzyme concentration and fit via nonlinear regression to a Michaelis-Menten kinetic model using GraphPad Prism software version 5.0 for Windows.

4.4.10 Active site tunnel analysis by CAVER 2.0 Active site tunnel analysis was performed with CAVER 2.0 software.[32] The MPD molecule occupying the analogous position in the NicA2 structure was used to define the binding site of the substrate.

4.5 Results and Discussion

4.5.1 NctB overall structure analysis The structure of NctB was found to have the same topology and overall fold as the previously described NicA2.[5] Alignment of NctB via the TM-align program revealed an RMSD of 1.10 Å relative to the 6-hydroxy-nicotine oxidase bound NicA2 structure with a TM-align score of 0.98 (PDB ID: 6C71) and 1.15 Å to the unbound NicA2 structure with a TM-align score of 0.97 (PDB ID:5TTJ). Significant structural homology exists between the NctB and NicA2 structure given the disparate functional properties of these enzymes. By contrast, the enzyme in the RCSB which has the greatest functional homology to the NctB, the 6HLNO, was found to have only a 2.60 Å RMSD and TM-align score of only 0.89.

4.5.2 Attempted substrate soaking of NctB crystals Efforts to acquire the substrate bound structure of NctB via anerobic soaking of (S)-6-hydroxy-nicotine under argon were unsuccessful. Remarkably, the crystals retained their yellow color suggesting the flavin was not reduced. It should be noted that three sites containing electron density consistent with 2-methyl-2,4-pentanediol (MPD) molecules from the crystallization solution were observed in the density maps of the NctB structure. MPD may have sufficient affinity for the NctB active site at a concentration of 25% (v/v) to outcompete the native substrate. Soaking the crystals in a solution analogous to the crystallant wherein the MPD was substituted for PEG 8000 @ 25% v/v resulted in crystals that bleached upon addition of (S)-6-hydroxy-nicotine, but which did not diffract.

Table 4-1 Summary of relevant crystallographic data

	Pt-Bound NctB	**NctB (RCSB:6CR0)**
Data Collection		
Unit-cell parameters (Å, º)	$a = b = 96.211$, $c = 78.68$ $\alpha = \beta = 90^o$, $\gamma = 120^o$	$a = b = 96.28$, $c = 78.62$, $\alpha = \beta = 90^o$, $\gamma = 120$
Space group	$P3_121$	$P3_121$
Resolution (Å)[1]	48.1-2.10 (2.16-2.10)	48.14-1.55 (1.64-1.55)
Wavelength (Å)	1.072040	1.000000
Temperature (K)	100	100
Observed reflections	250388	607045
Unique reflections	24990	61448
$\langle I/\sigma(I)\rangle$[1]	25.8 (3.7)	17.0 (1.8)
Completeness (%)[1]	99.9 (98.9)	99.8 (97.2)
Multiplicity[1]	10.0(9.9)	9.9(9.0)
R_{merge} (%)[1, 2]	0.070 (0.628)	0.069 (1.349)
R_{meas} (%)[1, 4]	0.074 (0.662)	0.073 (1.439)
R_{pim} (%)[1, 4]	0.023 (0.209)	0.023 (0.471)
$CC_{1/2}$ [1, 5]	0.999 (0.906)	0.999 (0.663)
Phasing		
Anom. Completeness	99.8 (98.0)	NA
Anom. Multiplicity	5.1 (5.0)	NA
FOM	0.90	NA
Refinement		
Resolution (Å)		31.52-1.55
Reflections (working/test)		58,322/3,082
R_{factor} / R_{free} (%)[3]		14.9/18.5
No. of atoms (protein/FAD/water)		3,323/53/276
Model Quality		
Rms deviations		
Bond lengths (Å)		0.009
Bond angles (º)		1.056
Average *B* factor (Å^2)		
All Atoms		30.3
Protein		29.9
FAD		22.5
Water		35.8
Coordinate error, maximum likelihood (Å)		0.14
Ramachandran Plot		
Most favored/Additionally Allowed (%)		97.9/1.90

1. Values in parenthesis are for the highest resolution shell.
2. ΣR_{merge} = $\Sigma hkli$ |Ii(hkl) - <I(hkl)>| / $\Sigma hkl \Sigma i$ Ii(hkl), where Ii(hkl) is the intensity measured for the ith reflection and <I(hkl)> is the average intensity of all reflections with indices hkl.
3. R_{factor} = Σhkl ||F_{obs} (hkl)| - |F_{calc} (hkl)|| / Σhkl |F_{obs} (hkl)|; R_{free} is calculated in an identical manner using 5% of randomly selected reflections that were not included in the refinement.
4. R_{meas} = redundancy-independent (multiplicity-weighted) R_{merge}-[17, 33]. R_{pim} = precision-indicating (multiplicity-weighted) R_{merge}[34, 35]
5. CC1/2 is the correlation coefficient of the mean intensities between two random half-sets of data.[36, 37]

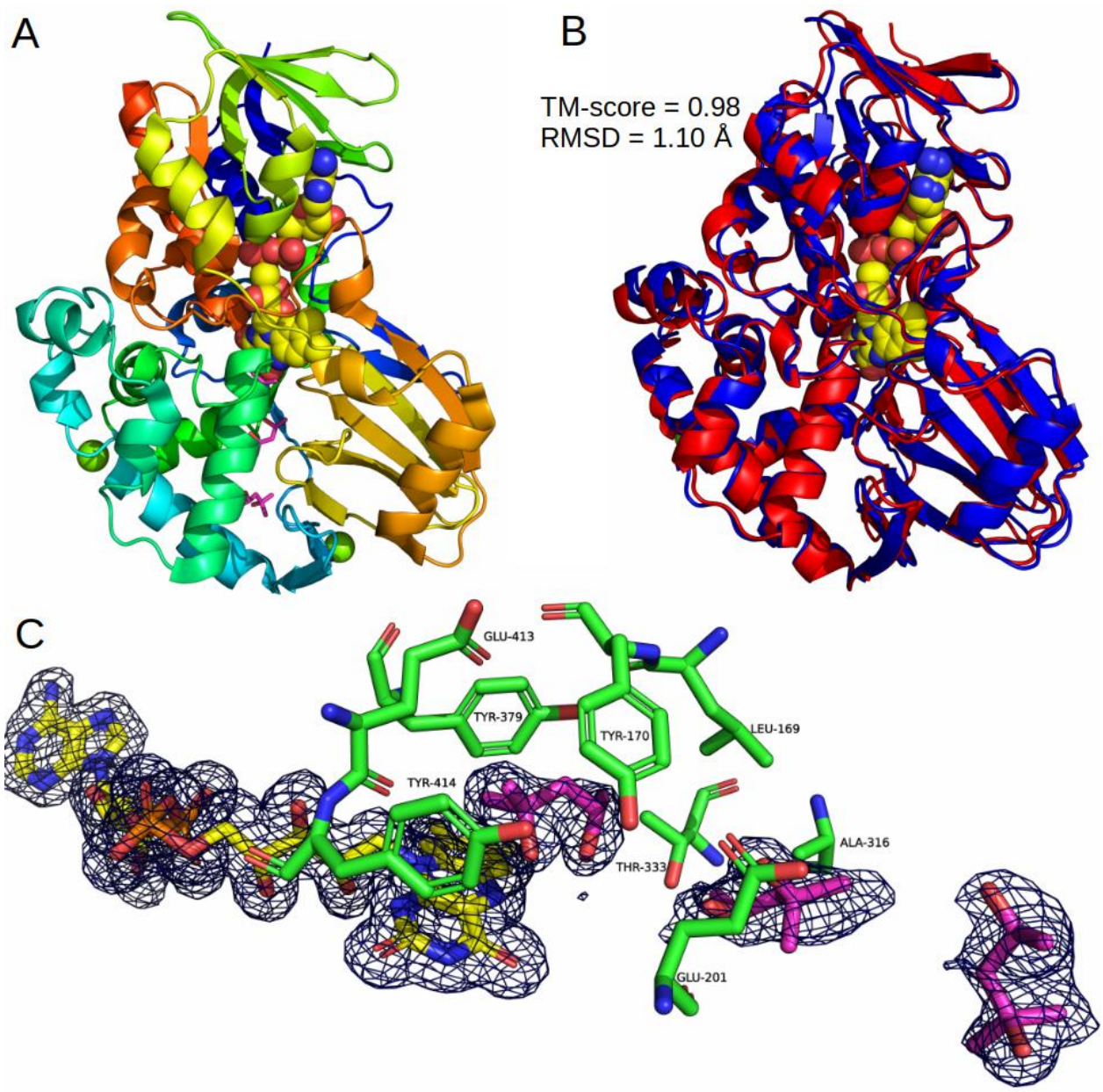

Figure 4-1 Depiction of NctB crystal structure (RCSB: 6CR0) and its alignment to the closest structural homolog in the PDB, NicA2 (RCSB: 6C71).A) NctB crystal structure (RCSB: 6CR0) bound to 2-methyl-1,3-propanediol (MPD). Calcium ions are shown as green spheres, the backbone ribbons cartoon colored as a red to blue / N to C terminus gradient, and the FAD cofactor molecule is shown as yellow sticks. **B)** Backbone atom TM-align alignment of NctB and NicA2 substrate bound structure (RCSB: 6C71). NctB backbone shown in blue, the NicA2 shown in red, and the flavin ligands are shown as yellow sticks. **C)** Active site structure of NctB. Three MPD ligands are bound to the active site and the entrance / exit channel and are shown in magenta with the F_o-F_c density map contoured to 3σ in blue mesh. Active site side chains making contact to the active site MPD ligand are displayed as green sticks and the FAD co-factor is displayed as yellow spheres.

4.5.3 NctB flavin geometry comparison to NicA2 apo and substrate bound structures Unlike the unbound forms of NicA2 and HLNO crystal structures, our density map shows that the flavin ring system is bent in the absence of substrate (Figure 2). A bent flavin ring system is often observed in substrate and inhibitor bound flavin oxidase crystal structures and has been previously linked to the tuning of the flavin redox potential in the Michaelis complex.[38, 39] The observation of a bent flavin in NctB in the presence of bound MPD suggests that the active site may have already undergone other induced fit structural changes. These structural changes may be analogous to those observed in the crystal structure of glycerol complexed with cholesterol oxidase.[39] This hypothesis is also consistent with the differences observed in flavin ring system geometries between the NicA2 *apo*(flat) and *holo*(bent) structures. The transition from a planar to a bent flavin ring system geometry upon substrate binding in NicA2 suggests a similar mechanism may exist in NctB. These structural changes may be similar to those that occur upon binding of the substrate. Since docking results are often more accurate when performed on structures that have already undergone induced fit changes with their ligands, the presence of MPD in the structure may potentially facilitate a more accurate prediction of the true Michaelis complex by our docking studies.

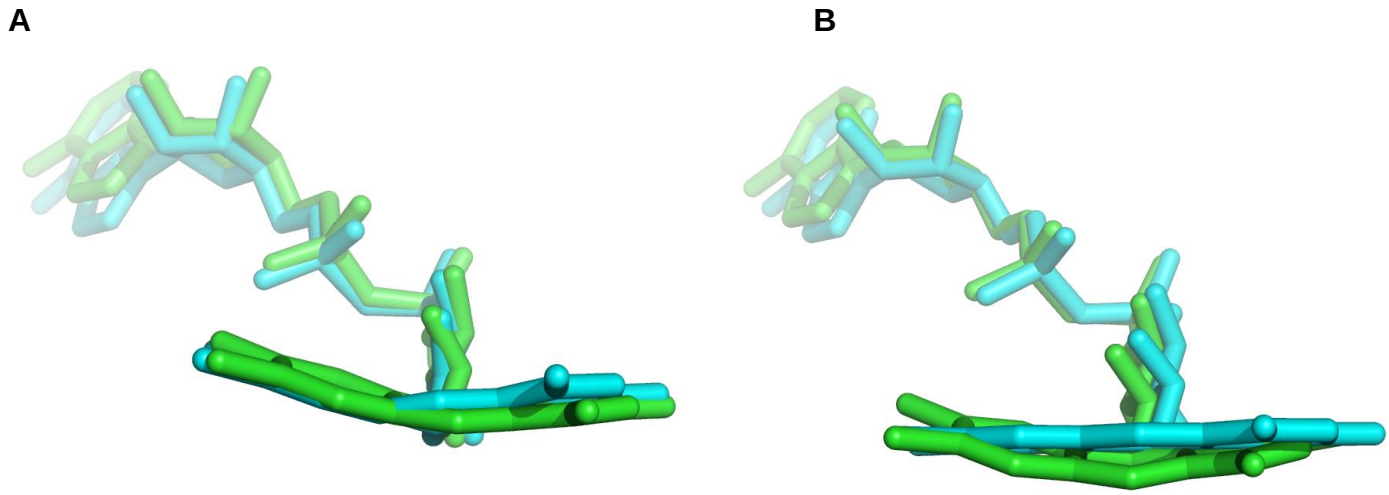

Figure 4-2 Comparison of flavin ring system geometry

A) Alignment of the NctB unbound structure (green) to the NicA2 unbound structure (blue). **B)** Alignment of the NctB unbound structure (green) to the NicA2 nicotine bound structure (blue).

4.5.4 Comparison of enzyme substrate interactions in the NctB and NicA2 enzymes. To facilitate analysis of the binding interaction of NctB to (S)-6-hydroxy-nicotine, AutoDock Vina™[26, 27, 40] was used to dock the substrate into the active site of the MPD bound NctB structure. The lowest energy docked structure is shown in Figure 3A. This predicted complex is highly similar to the experimentally determined complex of (S)-nicotine bound to NicA2. Both structures possess a conserved active site tyrosine (TYR170 in NctB and TYR218 in NicA2) positioned to form a hydrogen bond with the pyrrolidine nitrogen of the substrate, and a conserved threonine (THR333 in NctB and THR381 in NicA2) that is poised to form a second hydrogen bond to the substrate. In the NctB docked structure, THR333 is sufficiently close that it could potentially form a hydrogen bond with either the 6' hydroxyl group or the pyrimidine nitrogen of the substrate. In addition to facilitating the binding and orientation of substrate, TYR170 of NctB may serve a similar role as does TYR407 in 6HLNO, which has been proposed to facilitate the deprotonation of (S)-nicotine prior to hydride transfer.[41] In both complexes, the hydrogen bound to the substrate's tertiary carbon is positioned just above N5 of the flavin cofactor in an orientation suitable for hydride transfer. The canonical 'hydrophobic cage' in the NctB active site is comprised of just three aromatic residues - TYR414, TYR379, and TYR170. By contrast the hydrophobic cage in NicA2 is comprised of five aromatic residues- TRP427, TRP108 TYR218, TYR214 and TRP364. The presence of A316 in NctB at the homologous position of W364 in NicA2 results in a binding site that is both less sterically occluded from the primary substrate entrance / product exit channel of the enzyme, and forms fewer hydrophobic interactions with its substrate. The additional hydrophobic / aromatic contacts that form between NicA2 and its substrate may partially account for the dramatically lower K_m of this enzyme compared to NctB. Interestingly, in both active sites, a conserved glutamate residue (GLU249 in

NicA2 and GLU209 in NctB) is oriented distal to a corresponding aromatic cage tyrosine (TYR214 in NicA2 and TYR414 in NctB). The homologous glutamate side chains occupy distinct rotamers that position the carboxylic acid moieties away from the corresponding tyrosines (Figure 3C), a structural difference whose functional role is unclear.

A high level of similarity exists between the (S)-6-hydroxy-nicotine / NctB complex and the (S)-nicotine / NicA2 complex. The AutoDock Vina™ derived model reproduces the hydrogen bonding interactions, the relative orientation of the substrate in the active site, and the critical proximity of the C5 bound hydrogen of the substrate to the N5 of the flavin, strongly suggesting that the docked NctB structure is a good model for the Michaelis complex.

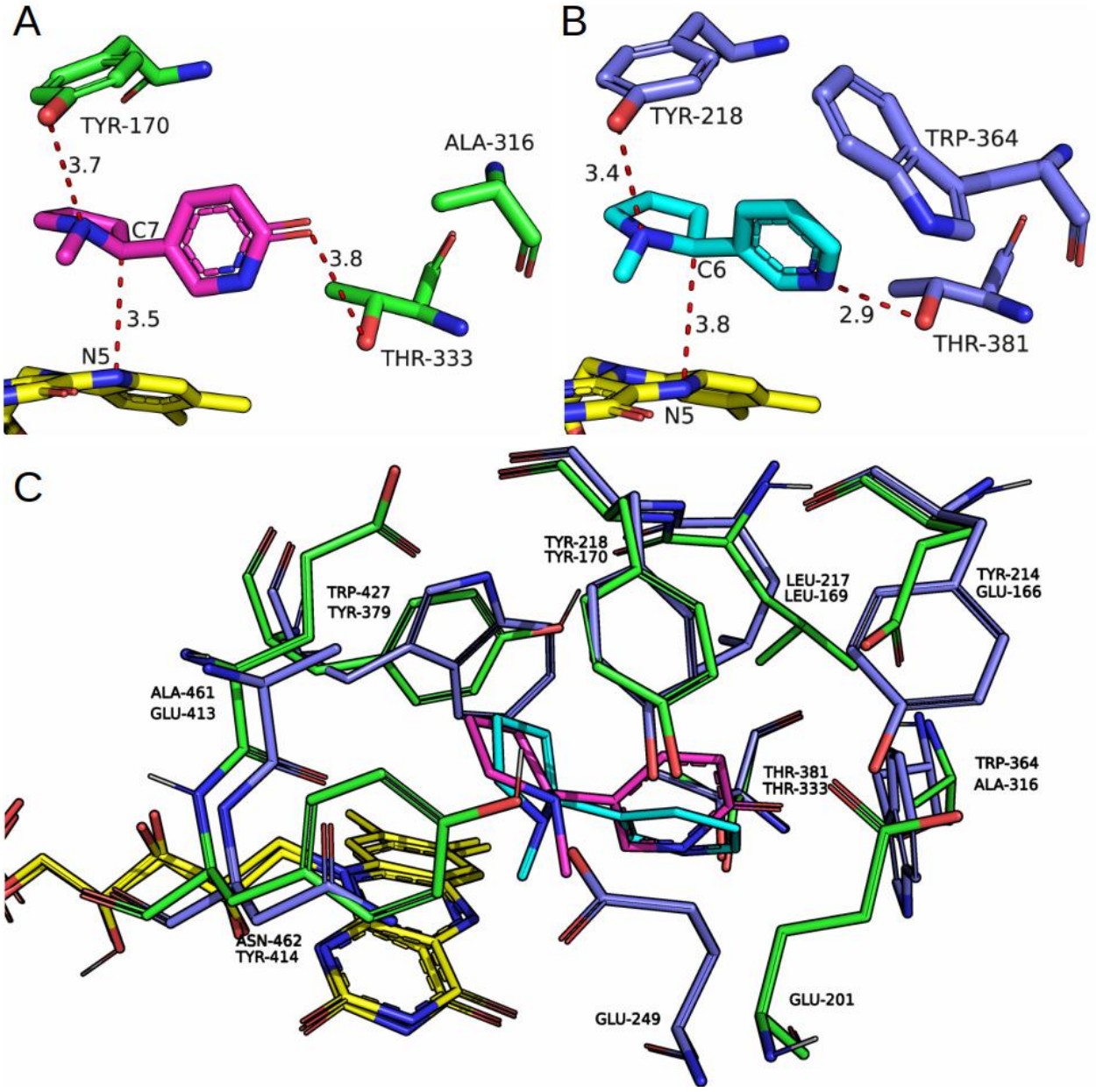

Figure 4-3 Comparison of modeled NctB and experimental NicA2 substrate bound structures A) Structure of NctB bound to (S)-6-hydroxy-nicotine (6HLN) predicted by AutoDock Vina. The 6HLN is shown in magenta sticks, the FAD molecule is shown as yellow sticks, and the side chains are shown as green sticks. Distance rulers (Å) are shown in red. **B)** Structure of NicA2 bound to (S)-nicotine (RCSB: 6C71).[5] The (S)-nicotine is shown in cyan sticks, the FAD molecule is shown as yellow sticks, and side chains are shown as blue sticks. Distance rulers (Å) are shown in red. **C)** Structural alignment of the 6HLN bound NctB docking model and NicA2 (S)-nicotine bound crystal structure. The active site side chains within 7 Å of the docked substrate are displayed as green sticks (NctB) blue sticks (NicA2), 6HLN shown as magenta sticks, the (S)-nicotine is shown as cyan sticks, and FAD cofactors are displayed as yellow sticks. Homologous sidechains are labeled with NicA2 residue identifiers above NctB residue identifiers.

4.5.5 Rational improvement of (S)-nicotine binding by NctB In the NicA2 substrate bound structure, W364 forms an edge-to-face hydrophobic interaction with the pyridine ring of (S)-nicotine. By contrast, in the NctB active site substitution of an alanine amino acid, the homologous position (A316) results in a water filled cavity that is able to accommodate the 6'-hydroxyl group of (S)-6-hydroxy-nicotine. Residue W364 of NicA2 has been previously hypothesized as important for both the binding of (S)-nicotine to the NicA2 active site and for mediating the rate of product release after catalysis.[4] The substitution of an alanine residue at this position is among the most dramatic structural differences observed by inspecting the alignment of these active sites. The aligned structures share a high degree of local structural similarity with respect to the location of the Cα atoms of the A316 and W364 residues and with respect to the position and conformation of the substrates. We hypothesized that by replacing A316 in NctB with the homologous tryptophan residue present in the NicA2, or with another bulky hydrophobic residue, we could increase the chemical complementarity of the NctB active site for (S)-nicotine, and thereby reduce the K_m of the enzyme while hopefully retaining a high oxidative turnover. Kinetic analysis of the A316W, A316V, and A316I NctB mutants revealed that while the homologous tryptophan mutation did not reduce the K_m of the enzyme for (S)-nicotine, the isoleucine substitution resulted in a modest 34% reduction in K_m (Table 2). Substitution with valine did not improve either kinetic parameter. The observed reduction in K_m with reduction in k_{cat} observed for the A316I mutants suggests that while this mutation enhanced the binding affinity of (S)-nicotine in the NctB active site, other steps of the catalytic cycle were inhibited. Suboptimal orientation of the bound substrate for hydride transfer is one possible explanation for the drop in k_{cat}, although the possibility that the substitutions are inhibiting

product release in a manner analogous to the previously proposed role of W364 in NicA2[4] cannot be ruled out by our steady state kinetic analysis.

Table 4-2 Comparison of kinetic parameters of native enzymes and single point mutation variants. Standard errors from non-linear regression fitting to the Michaelis -Menton equation are shown.

	k_{cat} , s^{-1}	K_m, μM
NicA2	0.011	Not determined
NctB	0.918 ± 0.04	940.9 ± 121.2
NctB A316W	0.5020± 0.020	1145±116.6
NctB A316V	0.823 ± 0.01	1314 ± 45.8
NctB A316I	0.622 ± 0.01	622.1 ± 32.9

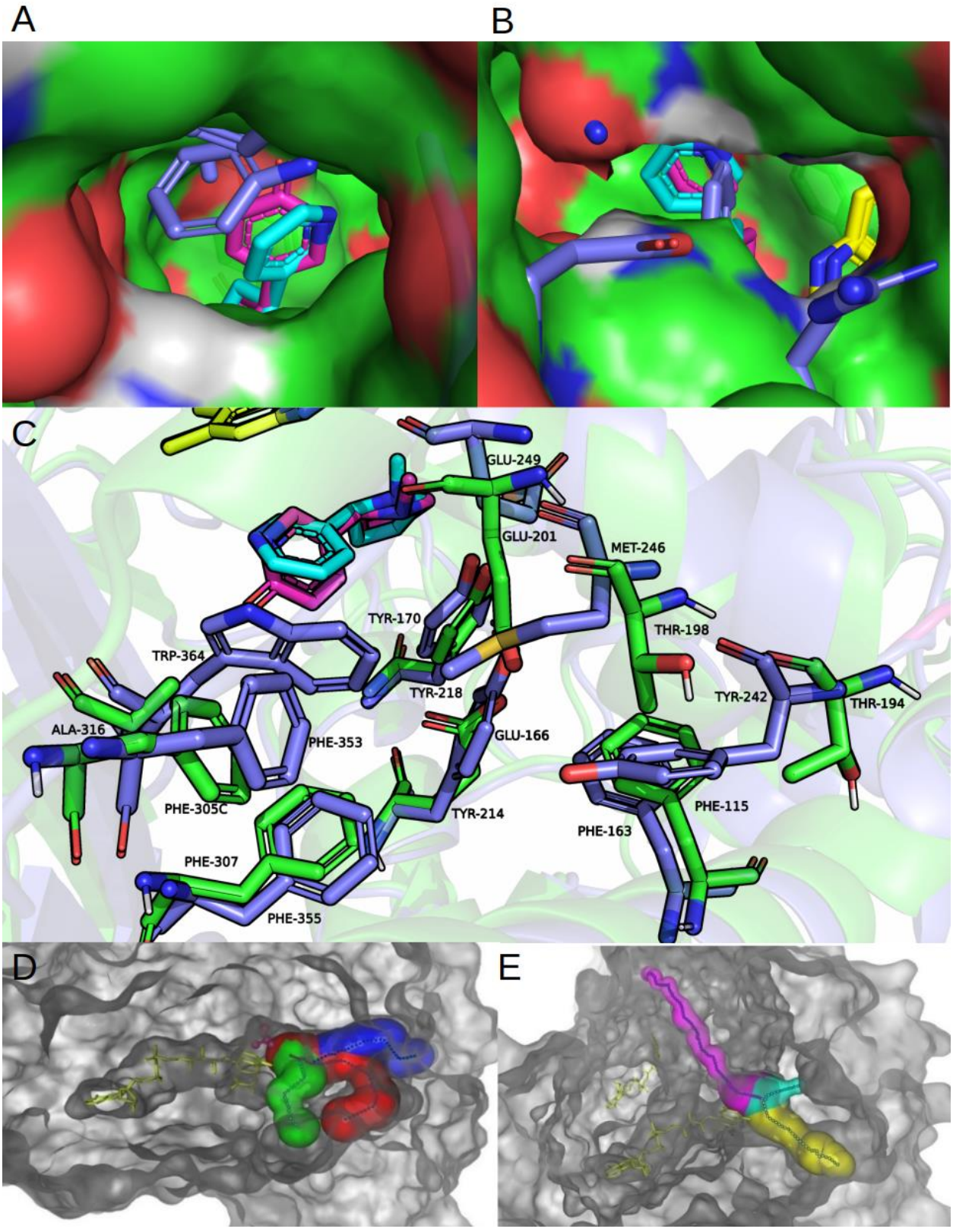

Figure 4-4. Comparison of active site accessibility of NctB and NicA2 A) NctB / NicA2 alignment showing primary active site access channel of NctB and the occlusion by W364 in NicA2. The NctB surface is shown in

green, (S)-nicotine is shown in cyan, (S)-6-hydroxy-nicotine is shown in magenta, and W364 of NicA2 is shown is blue sticks. **B)** NctB /NicA2 alignment showing the secondary active site access channel of NctB and the occlusion of this region by R253 and W108 of NicA2. The NctB surface is shown in green, (S)-nicotine is shown in cyan, (S)-6-hydroxy-nicotine is shown in magenta, and residues W253, D130, and W108 of NicA2 are shown is blue sticks. **C)** Comparative alignment showing residues lining the primary channel of NctB to residues implicated in the deceleration of product release in NicA2. NctB residues are shown as green sticks, the NicA2 residues are shown as blue sticks, (S)-nicotine is shown in cyan, (S)-6-hydroxy-nicotine is shown in magenta, the NctB backbone is shown as partially transparent green cartoon, and the NicA2 backbone is shown as partially transparent blue cartoon. **D)** Channels in NctB as determined by CAVER 2.0 analysis (Minimum Probe radius: 0.4 Å, shell radius: 3 Å, shell depth: 4 Å). The MPD molecule proximal to the FAD was used to define the binding site for the CAVER analysis. The top three tunnels with minimum bottlenecks of 2.14 Å, 2.00 Å, and 1.64 Å are shown here in blue, green, and red, respectively. FAD co-factor is shown as yellow sticks and the MPD molecule occupying the putative nicotine binding site is shown in purple. **E)** Channels in NicA2 as determined by Caver 2.0 analysis (minimum Probe radius: 0.4 Å, shell radius: 3 Å, shell depth: 4 Å). The top three channels with minimum bottlenecks of 2.11 Å, 1.05 Å, and 0.91 Å are shown here in yellow, cyan, and purple, respectively. The FAD co-factor is shown as yellow sticks.

4.5.6 NctB active site accessibility comparison to NicA2 Significant differences exist in the active site accessibility of NctB and NicA2. A comparison of the accessibility of the active sites in these enzymes is shown in Figure 4. When inspecting the active site of the NctB structure, it is apparent that an MPD molecule occupies the location where (S)-nicotine or (S)-6-hydroxynicotine would be expected to bind. Two additional MPD molecules occupy discrete densities in what we hypothesize to be the substrate entrance / product egress channel of the enzyme. These MPD ligands are shown as magenta sticks in Figure 1C, and the channel identified by CAVER 2.0 is shown in blue in Figure 4D. Caver 2.0 analysis also reveals two additional large channels in NctB that converge at the surface of the protein which are shown in green and red in Figure 3D. Comparison of the channels identified by CAVER reveals that the NctB active site is significantly more accessible than that of NicA2. The analysis also reveals that the 'backside' channel of NicA2 (shown in magenta in Figure 4E), which has been proposed to be the substrate entrance channel of NicA2,[4] is absent in NctB. These differences suggest that while NicA2 may possess distinct substrate entrance and product egress channels, NctB product egress may occur through any of the channels observed in this enzyme (shown in green, blue, and red in Figure 4D). These additional channels may also permit better oxygen diffusion to the active site assisting in the reoxidation of the NctB flavin, and thereby contributing to its high k_{cat}.

Nine bulky residues (F163, Y214, Y218, Y242, M246, E249, F353, F355, and W364) occupying the putative substrate egress channel of NicA2 have been proposed to reduce the rate of product release from the enzyme.[4] While three residues (F305, F307, F115) which occupy spatially homologous positions in NctB are identical and overlapping, several significant substitutions are observed that change the accessibility of the channel. In particular, the substitution of alanine at position 316 of NctB for a tryptophan at position 364 in NicA2 results

in the substrate binding site being directly accessible from the protein surface. By contrast, in the NicA2 structure, the active site is fully occluded from solvent due to the presence of W364. Substitution of threonine in place of a methionine at position 198 and substitution of a threonine for a tyrosine at position 194 in NctB also cause the putative substrate entrance / exit channel to be significantly more open and accessible to bulk solvent than in the NicA2 structure, as shown in Figure 4C. Apart from the significant disparity in sidechain bulk at these three positions, the other five homologous residues purported to slow down product release in NicA2 are identical in the NctB structure. Despite these bulky residues lining the primary substrate/product channel of the enzyme, the NctB is still able to turn over many times a second.

The increased accessibility of the active site of NctB vs NicA2 may play a role in the increased rate of the oxidative half reaction of NctB by allowing for greater access of oxygen to the flavin and/or by facilitating faster product release from the enzyme as compared to NicA2. Kachalova has proposed, based on kinetic data and crystallographic analysis of intermediates, that the rate of oxygen reduction by $6HLNO_{red}$ is lower when substrate is bound in the active site of the enzyme,[41] an effect that might also occur when product remains bound. Future work should evaluate the rate of product release in NctB, since rapid product release would support the hypothesis that the higher k_{cat} of NctB is partially due to the kinetics of product release.

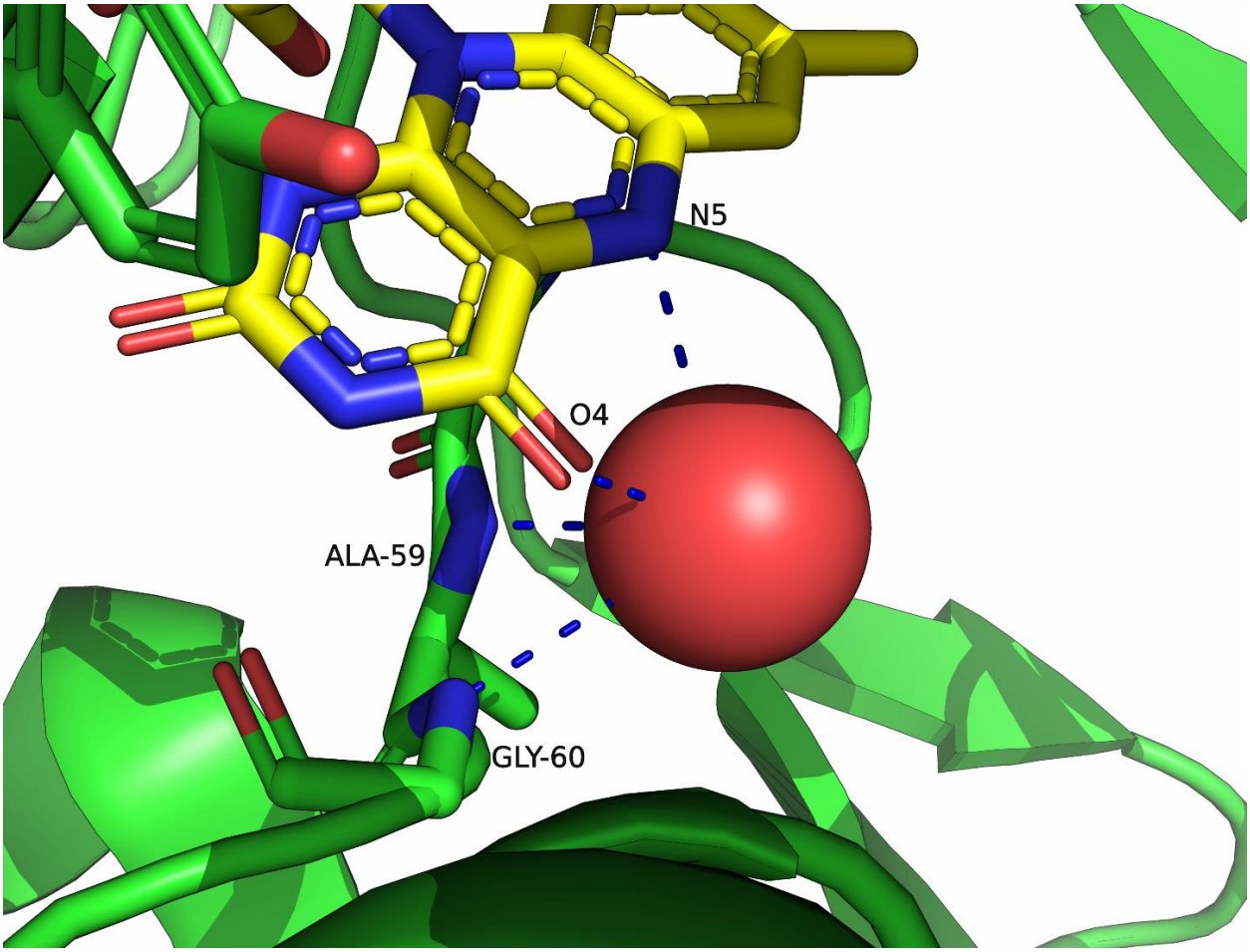

Figure 4-5 Proposed oxygen binding site in NctB occupied by structured water in NctB The NctB backbone is shown as a green cartoon, H2O775 is shown as a red space filling sphere, FAD is shown as yellow sticks, and residues within hydrogen bonding distance of H2O775 are shown as green sticks. Blue rulers show hydrogen bonding interactions between the H2O775 and the protein..

4.5.7 Oxygen site comparison and NicA2 oxygen channel / site engineering In addition to the differences in the nicotine binding site and active site access channels, significant differences between NctB and NicA2 exist near C4a of the flavin ring. This carbon center is where molecular oxygen is thought to react with $FADH_2$ in the oxidative half reaction of flavin amine oxidases.[42, 43] In NctB, a structured water (H_2O775) is bound proximal to C4a, is oriented just below the plane of the flavin ring system on the *si*-side, and occupies a volume suitable in size for molecular oxygen (Figure 5). By comparison, this volume in NicA2 is occluded by a combination of W108 and the conformation of the peptide backbone that runs along the *si*-side of the flavin. Additionally, H_2O775 is hydrogen bonded to LYS331. This residue may play a role in oxygen activation in a manner analogous to the proposed role of LYS287 in the 6HLNO oxygen site, which interestingly is also occupied by a water hydrogen bonded to an adjacent lysine.[41] NicA2 retains a lysine at the homologous position, LYS340, but there may not be sufficient volume in the cavity formed by the isoalloxazine ring, TRP108, ALA107 and LYS340 to accommodate either water or molecular oxygen. Additionally, the proximity of HIS205 to H_2O775 suggests the former could also serve a role in NctB oxygen activation, as a protonated histidine is a frequently observed feature of oxygen sites in flavin oxidases.[44] In NicA2, HIS205 is substituted by an arginine (ARG253), the guanidinium group of which is positioned to occlude access to the active site. The reduced side chain size and different packing of HIS205 in NctB produces a channel that allows access to the *si*-side of the flavin from the bulk solvent. Based on these observations, we hypothesized that NicA2's oxidase activity would be enhanced by mutations aimed at recreating the proposed oxygen binding cavity and channel in NctB. Specifically, the W108G mutant was expected to create a cavity in which oxygen might bind, while the R253H mutant was anticipated to both restore the presence of a basic histidine in the

proximity of the site, partially fill the volume otherwise occupied by W108 in the wild-type structure, and to potentially make the *si*-side of the flavin more solvent accessible. Since R253 in the NicA2 substrate bound structure is engaged in a salt bridge with D130, a triple mutant in which this residue is mutated to alanine was also prepared. This additional mutation avoids changing the electrical environment at the mouth of the channel and mitigates the uncoordinated ASP side chain from potentially interfering with folding. Relative activity at V_{max} for NicA2 W103G/R253H and NicA2 W103G/R253H/D130A is shown in Figure 6.

The moderate improvement in oxidative turnover observed for the W108G/R253H/D130A triple mutant suggests that the difference in oxygen reactivity between NctB and NicA2 is at least partially accounted for by the steric occlusion of C4a of FAD by W103 and that further efforts to optimize the cavity produced by the W103G mutation may be fruitful.

\

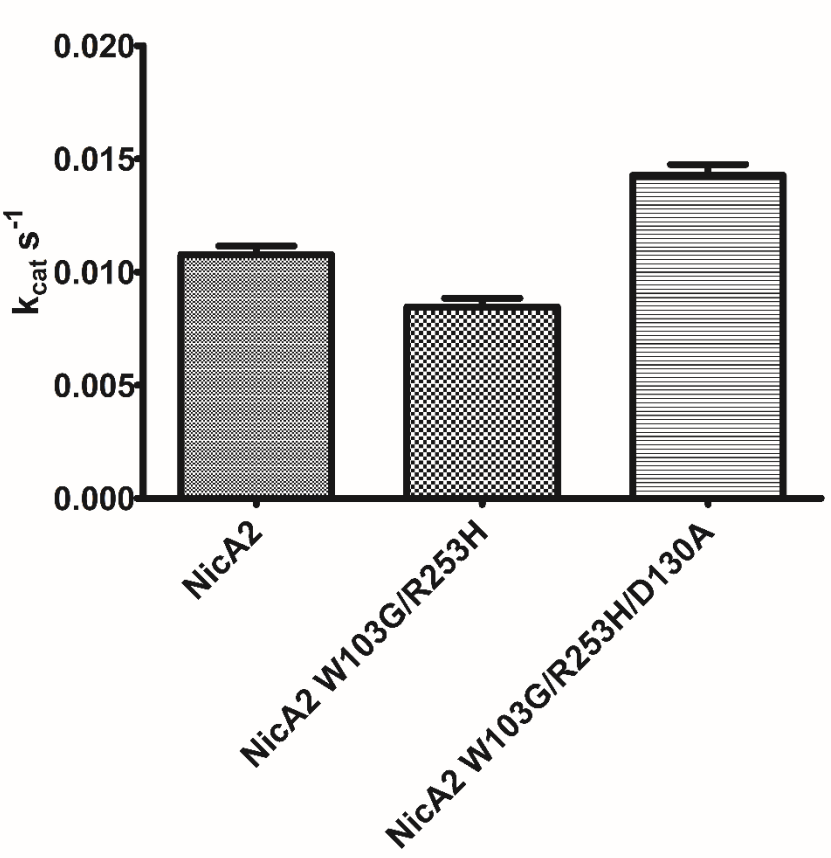

Figure 4-6 Observed rate of unimolecular turnover at Vmax. All data corrected for FAD occupancy.

It is unclear which nicotine degrading enzyme (NicA2, NctB, or an as yet undiscovered homolog) will ultimately prove the best starting point for the engineering of a highly efficient nicotine oxidase suitable for the discussed applications. Our rational design efforts only begin to survey the homologous mutations that could be evaluated, and further work along these lines has promise as a practical means to increase the efficiency of both enzymes. Beyond simply providing an accessible cavity for oxygen to bind, previous studies on the structural basis of oxygen reduction in flavin dependent amine oxidases suggest that future efforts should focus on providing the appropriate electrical environment for stabilization of the super oxyanion intermediate that forms during oxygen reduction.[1, 45]

Future work might also include exploring the kinetics of product release in the NctB A316 variants, crystallographic inspection of the oxygen site / channel structure of the NicA2 W103G/R253H/D130A variant, application of site saturated mutagenesis to residues of both NicA2 and NctB identified in this paper as being important to function, and the combination of beneficial mutations identified in this paper with those identified by other authors' rational design[1] and site saturated mutagenesis efforts[46]. Additionally, QM-MM analysis of oxygen binding and flavin reduction in NctB would give insights into what other structural features are important for endowing this enzyme with robust oxygen reactivity. Since the cost of nicotine dependence to society is measured in millions of deaths and trillions of dollars, demand for an efficient nicotine oxidizing enzyme for therapeutic and analytical applications is likely to persist until a solution is found

4.6 Acknowledgement

This publication is in memory of Professor Mark L. Richter, who unexpectedly passed away due to COVID-19 complications during the course of this manuscript's preparation. The authors of the paper would like to thank Professor Kim Colvert for her timely discussions on the kinetics of mutants related to those in this paper. Use of the IMCA-CAT beamline 17-ID at the Advanced Photon Source was supported by the companies of the Industrial Macromolecular Crystallography Association through a contract with Hauptman-Woodward Medical Research Institute. Use of the Advanced Photon Source was supported by the U.S. Department of Energy, Office of Science, Office of Basic Energy Sciences under contract no. DE-AC02-06CH11357.

4.7 Funding sources

This work was supported in part by a J.R. & Inez Jay grant from the University of Kansas.

4.8 Supplemental material

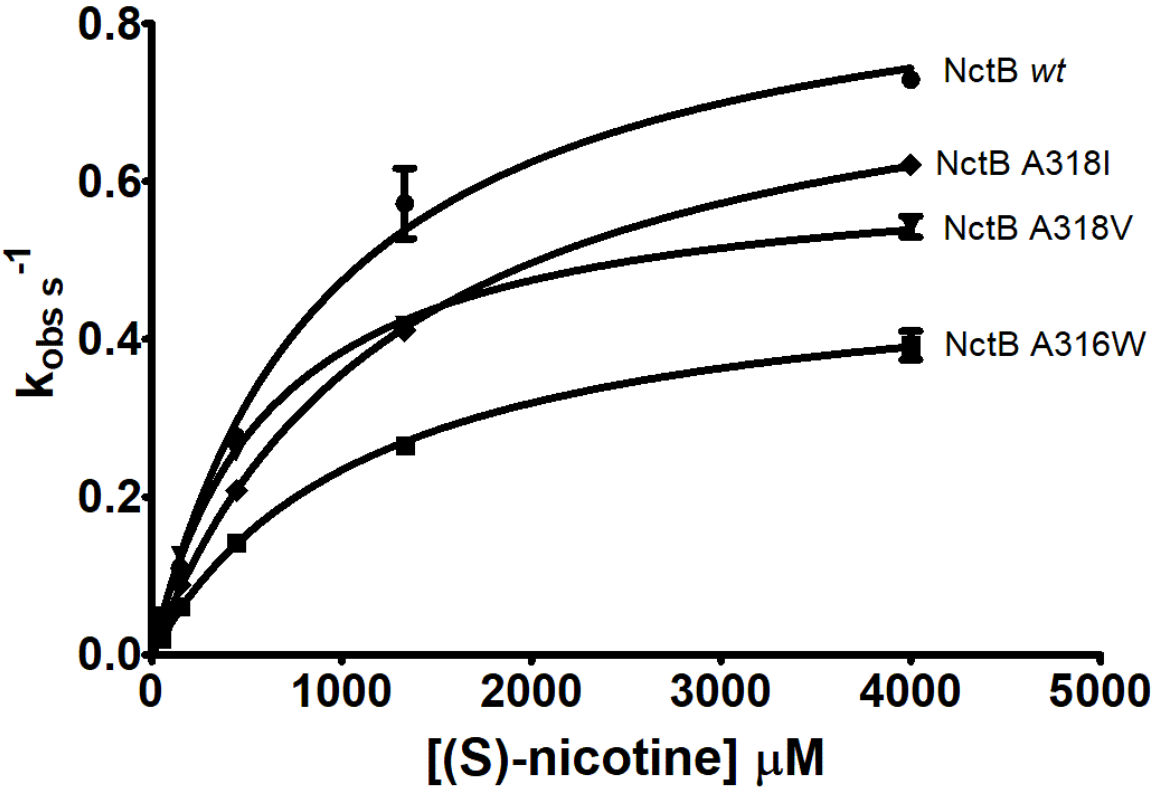

Figure 4-7 Kinetics of NctB variants Apparent unimolecular rate of turnover of NctB variants plotted vs. [(S)-nicotine].

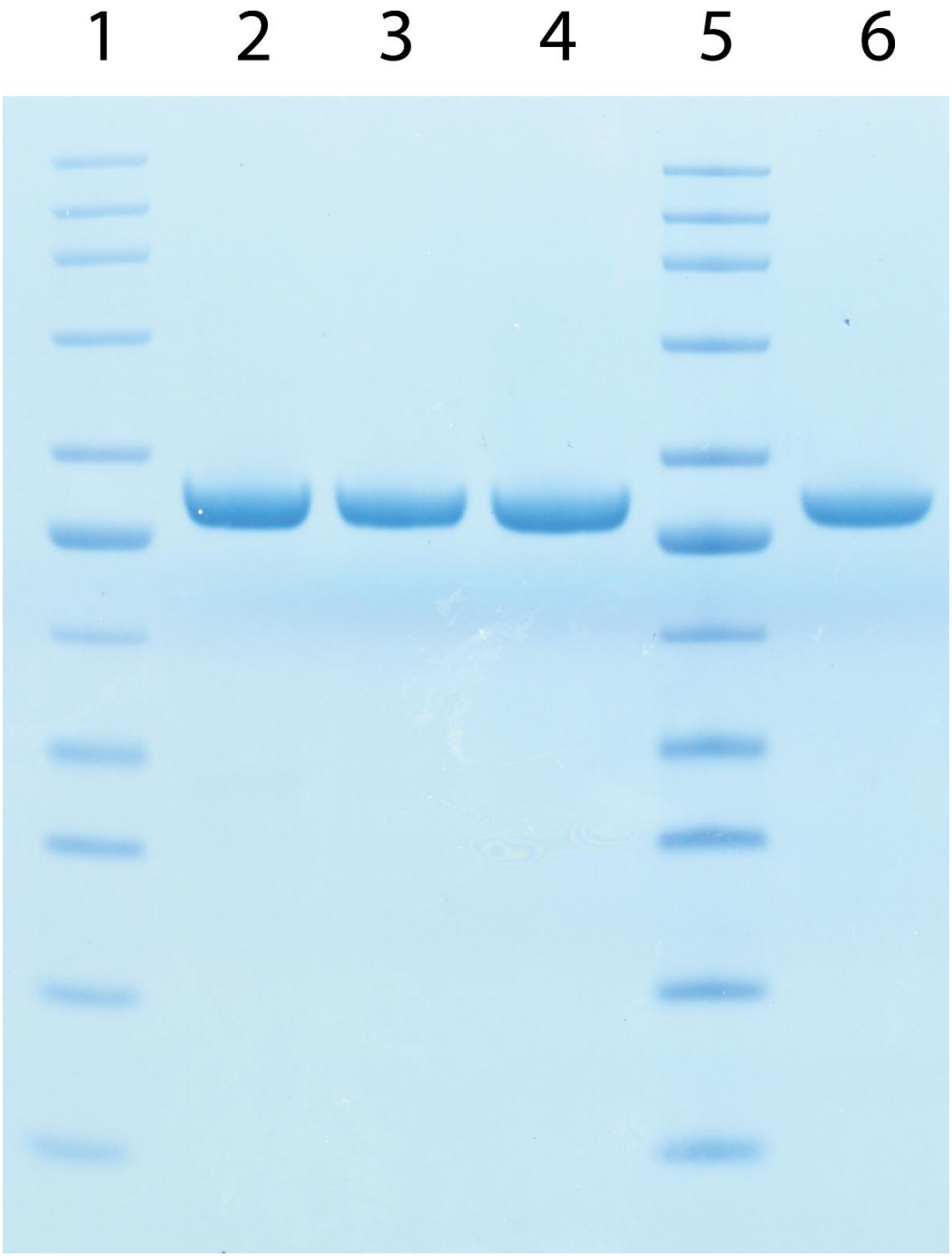

Figure 4-8 SDS-PAGE gel of NctB variants. 4-12% gradient Bis-Tris gel w/ NEB blue marker protein mW marker. Gel Key: Lane 1: Marker, Lane 2 NctB A316W, Lane 3: NctB A316L, Lane 4: NctB A316V, Lane 5: Marker, Lane 6: NctB-*wt*

4.9 Bibliography

1. Tararina, M. A.; Dam, K. K.; Dhingra, M.; Janda, K. D.; Palfey, B. A.; Allen, K. N., Fast Kinetics Reveals Rate-Limiting Oxidation and the Role of the Aromatic Cage in the Mechanism of the Nicotine-Degrading Enzyme NicA2. *Biochemistry* **2021,** *60* (4), 259-273.

2. Kallupi, M.; Xue, S.; Zhou, B.; Janda, K. D.; George, O., An enzymatic approach reverses nicotine dependence, decreases compulsive-like intake, and prevents relapse. *Science Advances* **2018,** *4* (10), eaat4751.

3. Pentel, P. R.; Raleigh, M. D.; Lesage, M. G.; Thisted, T.; Horrigan, S.; Biesova, Z.; Kalnik, M. W., The nicotine-degrading enzyme NicA2 reduces nicotine levels in blood, nicotine distribution to brain, and nicotine discrimination and reinforcement in rats. *BMC Biotechnology* **2018,** *18* (1).

4. Tang, H.; Zhang, K.; Hu, H.; Wu, G.; Wang, W.; Zhu, X.; Liu, G.; Xu, P., Molecular Deceleration Regulates Toxicant Release to Prevent Cell Damage in Pseudomonas putida S16 (DSM 28022). *mBio* **2020,** *11* (5).

5. Tararina, M. A.; Janda, K. D.; Allen, K. N., Structural Analysis Provides Mechanistic Insight into Nicotine Oxidoreductase fromPseudomonas putida. *Biochemistry* **2016,** *55* (48), 6595-6598.

6. Tararina, M. A.; Xue, S.; Smith, L. C.; Muellers, S. N.; Miranda, P. O.; Janda, K. D.; Allen, K. N., Crystallography Coupled with Kinetic Analysis Provides Mechanistic Underpinnings of a Nicotine-Degrading Enzyme. *Biochemistry* **2018,** *57* (26), 3741-3751.

7. Xue, S.; Schlosburg, J. E.; Janda, K. D., A New Strategy for Smoking Cessation: Characterization of a Bacterial Enzyme for the Degradation of Nicotine. *Journal of the American Chemical Society* **2015,** *137* (32), 10136-10139.

8. Briški, F.; Kopčić, N.; Ćosić, I.; Kučić, D.; Vuković, M., Biodegradation of tobacco waste by composting: Genetic identification of nicotine-degrading bacteria and kinetic analysis of transformations in leachate. *Chemical Papers* **2012,** *66* (12).

9. Tang, H.; Wang, L.; Meng, X.; Ma, L.; Wang, S.; He, X.; Wu, G.; Xu, P., Novel Nicotine Oxidoreductase-Encoding Gene Involved in Nicotine Degradation by Pseudomonas putida Strain S16. *Applied and Environmental Microbiology* **2009,** *75* (3), 772-778.

10. Dulchavsky, M.; Clark, C. T.; Bardwell, J. C. A.; Stull, F., A cytochrome c is the natural electron acceptor for nicotine oxidoreductase. *Nature Chemical Biology* **2021**.

11. Deay, D. O.; Colvert, K. K.; Gao, F.; Seibold, S.; Goyal, P.; Aillon, D.; Petillo, P. A.; Richter, M. L., An active site mutation in 6-hydroxy-l-Nicotine oxidase from Arthrobacter nicotinovorans changes the substrate specificity in favor of (S)-nicotine. *Archives of Biochemistry and Biophysics* **2020,** *692*, 108520.

12. Qiu, J.; Wei, Y.; Ma, Y.; Wen, R.; Wen, Y.; Liu, W., A Novel (S)-6-Hydroxynicotine Oxidase Gene from Shinella sp. Strain HZN7. *Applied and Environmental Microbiology* **2014,** *80* (18), 5552-5560.

13. Bradford, M. M., A rapid and sensitive method for the quantitation of microgram quantities of protein utilizing the principle of protein-dye binding. *Anal Biochem* **1976,** *72*, 248-54.

14. Tropea, J. E.; Cherry, S.; Waugh, D. S., Expression and purification of soluble His(6)-tagged TEV protease. *Methods Mol Biol* **2009,** *498*, 297-307.

15. Kabsch, W., Integration, scaling, space-group assignment and post-refinement. *Acta Crystallogr D Biol Crystallogr* **2010,** *66* (Pt 2), 133-44.

16. Vonrhein, C.; Flensburg, C.; Keller, P.; Sharff, A.; Smart, O.; Paciorek, W.; Womack, T.; Bricogne, G., Data processing and analysis with the autoPROC toolbox. *Acta Crystallogr D Biol Crystallogr* **2011,** *67* (Pt 4), 293-302.

17. Evans, P. R., An introduction to data reduction: space-group determination, scaling and intensity statistics. *Acta Crystallogr D Biol Crystallogr* **2011,** *67* (Pt 4), 282-92.

18. Evans, P. R.; Murshudov, G. N., How good are my data and what is the resolution? *Acta Crystallogr D Biol Crystallogr* **2013,** *69* (Pt 7), 1204-14.

19. Matthews, B. W., Solvent content of protein crystals. *J Mol Biol* **1968,** *33* (2), 491-7.

20. Skubak, P.; Arac, D.; Bowler, M. W.; Correia, A. R.; Hoelz, A.; Larsen, S.; Leonard, G. A.; McCarthy, A. A.; McSweeney, S.; Mueller-Dieckmann, C.; Otten, H.; Salzman, G.; Pannu, N. S., A new MR-SAD algorithm for the automatic building of protein models from low-resolution X-ray data and a poor starting model. *IUCrJ* **2018,** *5* (Pt 2), 166-171.

21. McCoy, A. J.; Grosse-Kunstleve, R. W.; Adams, P. D.; Winn, M. D.; Storoni, L. C.; Read, R. J., Phaser crystallographic software. *J Appl Crystallogr* **2007,** *40* (Pt 4), 658-674.

22. Liebschner, D.; Afonine, P. V.; Baker, M. L.; Bunkoczi, G.; Chen, V. B.; Croll, T. I.; Hintze, B.; Hung, L. W.; Jain, S.; McCoy, A. J.; Moriarty, N. W.; Oeffner, R. D.; Poon, B. K.; Prisant, M. G.; Read, R. J.; Richardson, J. S.; Richardson, D. C.; Sammito, M. D.; Sobolev, O. V.; Stockwell, D. H.; Terwilliger, T. C.; Urzhumtsev, A. G.; Videau, L. L.; Williams, C. J.; Adams, P. D., Macromolecular structure determination using X-rays, neutrons and electrons: recent developments in Phenix. *Acta Crystallogr D Struct Biol* **2019,** *75* (Pt 10), 861-877.

23. Emsley, P.; Lohkamp, B.; Scott, W. G.; Cowtan, K., Features and development of Coot. *Acta Crystallogr D Biol Crystallogr* **2010,** *66* (Pt 4), 486-501.

24. Chen, V. B.; Arendall, W. B., 3rd; Headd, J. J.; Keedy, D. A.; Immormino, R. M.; Kapral, G. J.; Murray, L. W.; Richardson, J. S.; Richardson, D. C., MolProbity: all-atom structure validation for macromolecular crystallography. *Acta Crystallogr D Biol Crystallogr* **2010,** *66* (Pt 1), 12-21.

25. McNicholas, S.; Potterton, E.; Wilson, K. S.; Noble, M. E., Presenting your structures: the CCP4mg molecular-graphics software. *Acta Crystallogr D Biol Crystallogr* **2011,** *67* (Pt 4), 386-94.

26. Morris, G. M.; Huey, R.; Lindstrom, W.; Sanner, M. F.; Belew, R. K.; Goodsell, D. S.; Olson, A. J., AutoDock4 and AutoDockTools4: Automated docking with selective receptor flexibility. *Journal of Computational Chemistry* **2009,** *30* (16), 2785-2791.

27. Trott, O.; Olson, A. J., AutoDock Vina: Improving the speed and accuracy of docking with a new scoring function, efficient optimization, and multithreading. *Journal of Computational Chemistry* **2009**, NA-NA.

28. ULC, C. C. G., Molecular Operating Environment (MOE), . **2019**.

29. Zhang, Y.; Skolnick, J., TM-align: a protein structure alignment algorithm based on the TM-score. *Nucleic Acids Res* **2005,** *33* (7), 2302-9.

30. Schrodinger, LLC, The PyMOL Molecular Graphics System, Version 1.8. 2015.

31. Zhou, M.; Diwu, Z.; Panchuk-Voloshina, N.; Haugland, R. P., A Stable Nonfluorescent Derivative of Resorufin for the Fluorometric Determination of Trace Hydrogen Peroxide: Applications in Detecting the Activity of Phagocyte NADPH Oxidase and Other Oxidases. *Analytical Biochemistry* **1997,** *253* (2), 162-168.

32. Jurcik, A.; Bednar, D.; Byska, J.; Marques, S. M.; Furmanova, K.; Daniel, L.; Kokkonen, P.; Brezovsky, J.; Strnad, O.; Stourac, J.; Pavelka, A.; Manak, M.; Damborsky, J.;

Kozlikova, B., CAVER Analyst 2.0: analysis and visualization of channels and tunnels in protein structures and molecular dynamics trajectories. *Bioinformatics* **2018,** *34* (20), 3586-3588.

33. Evans, P., Scaling and assessment of data quality. *Acta Crystallogr D Biol Crystallogr* **2006,** *62* (Pt 1), 72-82.

34. Diederichs, K.; Karplus, P. A., Improved R-factors for diffraction data analysis in macromolecular crystallography. *Nat Struct Biol* **1997,** *4* (4), 269-75.

35. Weiss, M., Global indicators of X-ray data quality. *Journal of Applied Crystallography* **2001,** *34* (2), 130-135.

36. Evans, P., Biochemistry. Resolving some old problems in protein crystallography. *Science* **2012,** *336* (6084), 986-7.

37. Karplus, P. A.; Diederichs, K., Linking crystallographic model and data quality. *Science* **2012,** *336* (6084), 1030-3.

38. Yu, L.-J.; Golden, E.; Chen, N.; Zhao, Y.; Vrielink, A.; Karton, A., Computational insights for the hydride transfer and distinctive roles of key residues in cholesterol oxidase. *Scientific Reports* **2017,** *7* (1).

39. Lyubimov, A. Y.; Heard, K.; Tang, H.; Sampson, N. S.; Vrielink, A., Distortion of flavin geometry is linked to ligand binding in cholesterol oxidase. *Protein Science* **2007,** *16* (12), 2647-2656.

40. Morris, G. M.; Huey, R.; Olson, A. J., Using AutoDock for ligand-receptor docking. *Curr Protoc Bioinformatics* **2008,** *Chapter 8*, Unit 8 14.

41. Kachalova, G.; Decker, K.; Holt, A.; Bartunik, H. D., Crystallographic snapshots of the complete reaction cycle of nicotine degradation by an amine oxidase of the monoamine oxidase (MAO) family. *Proceedings of the National Academy of Sciences* **2011,** *108* (12), 4800-4805.

42. Roth, J. P.; Wincek, R.; Nodet, G.; Edmondson, D. E.; McIntire, W. S.; Klinman, J. P., Oxygen Isotope Effects on Electron Transfer to O2Probed Using Chemically Modified Flavins Bound to Glucose Oxidase. *Journal of the American Chemical Society* **2004,** *126* (46), 15120-15131.

43. Baron, R.; Riley, C.; Chenprakhon, P.; Thotsaporn, K.; Winter, R. T.; Alfieri, A.; Forneris, F.; Van Berkel, W. J. H.; Chaiyen, P.; Fraaije, M. W.; Mattevi, A.; McCammon, J. A., Multiple pathways guide oxygen diffusion into flavoenzyme active sites. *Proceedings of the National Academy of Sciences* **2009,** *106* (26), 10603-10608.

44. Mattevi, A., To be or not to be an oxidase: challenging the oxygen reactivity of flavoenzymes. *Trends in Biochemical Sciences* **2006,** *31* (5), 276-283.

45. Su, Q.; Klinman, J. P., Nature of Oxygen Activation in Glucose Oxidase fromAspergillus niger: The Importance of Electrostatic Stabilization in Superoxide Formation†. *Biochemistry* **1999,** *38* (26), 8572-8581.

46. Thisted, T.; Biesova, Z.; Walmacq, C.; Stone, E.; Rodnick-Smith, M.; Ahmed, S. S.; Horrigan, S. K.; Van Engelen, B.; Reed, C.; Kalnik, M. W., Optimization of a nicotine degrading enzyme for potential use in treatment of nicotine addiction. *BMC Biotechnology* **2019,** *19* (1).

5 Summary

5.1 Introduction

The optimization of FPDGO enzymes is a critical field of research if the repertoire of analytes that can be monitored *in vivo* by amperometric biosensors is to be expanded. While the toolbox of FDPGO enzymes provided by evolution has allowed for the establishment of amperometric biosensing as a useful modality, without further enzyme design and optimization the number of available analytes is likely to remain limited. Commercialized glucose biosensors have revolutionized the treatment of diabetes, giving the field a preview of the benefits that continuous real time monitoring of analytes in tissue can provide for the treatment and understanding of disease. Rational design and directed evolution of existing enzymes is the obvious path forward for the biosensor field and represents one of the most promising practical applications of the emerging science of protein engineering.

My goal has been to improve the toolbox available to the developers of biosensors and enable better enzyme performance for *in vivo* and *in vitro* applications. By improving the suitability of various oxidase enzymes for biosensing applications, my research has contributed to expanding the range of analytes that can be monitored *in vivo* by biosensors. Specifically, this dissertation describes the structure informed rational improvement of (S)-nicotine oxidation by three different nicotine oxidizing enzymes and the successful use of a gold binding peptide fusion sequence for the orientation-controlled immobilization of a putrescine oxidase on gold surfaces.

5.2 Rational improvement of (S)-nicotine oxidation by (S)-6-hydroxy-nicotine oxidase from *A. nicotinovorans*

In Chapter 2 of this dissertation the rational improvement of nicotine oxidation by the (S)-6-hydroxy-nicotine oxidase from *A. nicotinovorans* was described, in addition to the stabilization of the enzyme by incorporation of an MBP fusion tag.

Substitution of the active site residue tyrosine at position 311 for tryptophan resulted in a ~265% increase in the k_{cat} for nicotine while reducing the specificity constant for (S)-6-hydroxy-nicotine by more than 60-fold. The enhanced k_{cat} with (S)-nicotine in the Y311W mutant may be due to the introduction of a stabilizing hydrophobic contact with the edge of the pyrimidine ring of nicotine, which was indeed observed in the docking study. This stabilizing interaction may limit conformational flexibility of nicotine within the active site promoting catalytically competent conformations.

The fusion of the HLNO enzyme to the maltose binding protein from *E. coli* resulted in a 4-fold increase in the co-factor occupancy of the purified recombinant protein. Higher co-factor occupancy resulted in enzyme material with proportionally higher mass specific activity, a property critical for the performance of the biorecognition element of enzymatic biosensors.

Finally, the addition of the MBP tag resulted in a 11 ºC increase in the melting temperature of the enzyme and an approximately 10-fold increase in the half-life of the enzyme upon prolonged incubation at 37 °C. Intramolecular interactions between the fusion tag and the flavin binding domain of the HLNO enzyme may stabilize parts of the structure important to co-factor retention that may experience denaturation over time at 37 ºC, consistent with the known chaperone properties of MBP.

Since flavin co-factor binding domains are a ubiquitous structural feature of FDPGOs, adding the MBP tag may well work to enhance retention of the bound flavin and thermal stability of other enzymes in the family. This would be of special significance for applications where loss of the flavin co-factor reduces the utility of the enzyme, such as is observed in various alcohol oxidases.[1] By demonstrating the viability of rational design as a means to improve the substrate specificity and activity profile of nicotine oxidizing FDPGOs, and by demonstrating the thermal stabilization of co-factor binding and catalytic activity of an FDPGO by an N-terminal MBP tag, this work significantly advances the effort to engineer a nicotine oxidizing enzyme suitable for biosensor applications.

5.3 Engineering of a gold binding putrescine oxidase

In Chapter 3 of this dissertation, the engineering of a putrescine oxidase that binds selectively to gold surfaces with nanomolar affinity was described. Metal binding FDPGO enzymes provide a single step bio-assembly process with orientation control, a critical parameter for functional immobilization of the enzyme layer in biosensors. In this study, for the first time, we showed the self immobilization of a putrescine oxidase enzyme using a gold binding peptide tag. This effort resulted in an enzyme with nanomolar affinity for gold surfaces. The functional activity and expression were investigated, along with the selectivity of the binding of the peptide-tagged enzyme. Activity assays of protein bound to nanoparticles provide evidence that the enzyme retained catalytic activity when immobilized. Additionally, AFM images show significant differences in the height of the molecules immobilized through the peptide tag compared to non specific adsorption of the native enzyme, indicating differences in orientation of the bound enzyme when attached via the affinity tag. This result is highly significant since the controlled orientation of surface-immobilized enzymes is recognized to have the potential to further

improve biosensor function,[2, 3] as well as having a potential impact on other diverse applications including oxidative biocatalysts, biochips, and biofuel production. These results demonstrate that self assembly of molecular layers of enzymes on electrode surfaces via metal affinity peptide tags has the potential to supplant glutaraldehyde crosslinking as the principle method employed for immobilization of FDPGO enzymes in biosensors. By utilizing an immobilization strategy that does not inactivate a vast majority of enzyme molecules or build up a thick matrix of crosslinked enzyme molecules, the use of metal affinity peptides as demonstrated in this work may lead to biosensors that are smaller, last longer, more responsive, and are less expensive to manufacture.

5.4 Rational improvement of nicotine oxidation by two different nicotine oxidizing enzymes

In Chapter 4 of this dissertation, the improvement of (S)-nicotine oxidation by two different nicotine oxidizing enzymes was described. Nicotine oxidase enzymes identified to date suffer from low efficiency, exhibiting either a high k_{cat} or low K_m but not both, as will be required to meet the demands of *in vivo* nicotine monitoring applications. In this work, the crystal structure of the (S)-6-hydroxy-nicotine-oxidase from *Shinella* sp HZN7 (NctB) was solved, an enzyme that oxidizes (S)-nicotine with a high k_{cat} (>1 s^{-1}). NctB possesses remarkable structural homology to an enzyme with a nanomolar K_m for (S)-nicotine, the (S)-nicotine oxidase from *Pseudomonas putidia* strain S16 (NicA2). Insights derived from comparison of the substrate binding sites of NicA2 and NctB informed a rational design effort that reduced the K_m of (S)-nicotine oxidation by the NctB protein by ~600 fold. Similarly, insights derived from comparison of the oxygen binding sites of NicA2 and NctB informed a rational design effort that increases the k_{cat} of oxidative turnover of (S)-nicotine by the NicA2 enzyme by 25%. This

structural and rational design work marks an important step towards the engineering of a nicotine oxidase with kinetic parameters that fulfill the functional requirements of *in vivo* applications. While motivated initially by the ambition to develop a nicotine biosensor, the work has taken on new significance with the emergent application of nicotine oxidizing enzymes to the blockade of (S)-nicotine blockade from the CNS.

5.5 Conclusion

In conclusion, the work presented in this dissertation furthers the field of FDPGO engineering for *in vivo* biosensing applications. The rational improvement of nicotine oxidation by three distinct nicotine oxidizing enzymes represents a significant contribution to the nicotine biosensor development field, while the stabilization of the HLNO enzyme by an MBP tag may have significance to the entire field of amperometric biosensors. Finally, the engineering of a gold binding putrescine oxidase that self immobilizes itself in an orientation-controlled manner on a metal surface has the potential to revolutionize how FDPGO enzymes are immobilized when manufacturing amperometric biosensors and in other applications where the self assembly of a catalytically active, orientation controlled FDPGO enzyme layer is desired.

5.6 Bibliography

1. Petillo, P. A., 2021.

2. McMillan, D. G. G.; Marritt, S. J.; Kemp, G. L.; Gordon-Brown, P.; Butt, J. N.; Jeuken, L. J. C., The impact of enzyme orientation and electrode topology on the catalytic activity of adsorbed redox enzymes. *Electrochimica Acta* **2013,** *110*, 79-85.

3. Park, M., Orientation Control of the Molecular Recognition Layer for Improved Sensitivity: a Review. *BioChip Journal* **2019,** *13* (1), 82-94.